TÉCNICO LISBOA

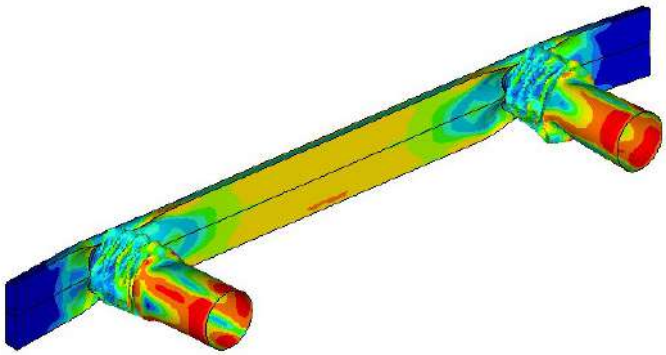

Multi-objective design optimization of a frontal crash energy absorption system for a road-safe vehicle

Tiago Miguel Encarnação Nunes

Thesis to obtain the Master of Science Degree in

Aerospace Engineering

Supervisors: Prof. André Calado Marta
Eng. Luís Miguel Ouro Colaço

Examination Committee

Chairperson: Prof. Filipe Szolnoky Ramos Pinto Cunha
Supervisor: Prof. André Calado Marta
Member of the Committee: Prof. João Manuel Pereira Dias

November 2017

Acknowledgments

First and foremost, I would like to thank my supervisors, engineer Luís Colaço, and Professor André Calado Marta. It was a privilege to be guided by two amazing professionals and learn from their experience.

Thanks to CEiiA for the opportunity to work in one of their most ambitious and challenging projects. To all the mobility team, thanks for all the help and for treating me as one of them since the first day. A special thanks to engineers José Silva, Inês Martins and Inês Crespo for their guidance and for always being available.

To my internship colleagues Pedro Reguenga, Carlos Lopes and Miguel Leal for all the motivation. I wish you the best. Keep working hard and follow your dreams.

To Técnico Lisboa and especially to my Técnico Lisboa friends, Rodolfo Dutra, Rui Pires, João Filipe Mendes, Vítor Mendonça and Duarte Santos, for being present during the best and the worst moments of this five years journey. All the deadlines and sleepless nights became easier because of you.

To my father, for always supporting and encouraging me to follow my dreams, respecting my choices and believing in me, even more than I do. For dedicating his life to me and my brothers, I will never forget that. To my brother and sister, thank you for always being there for me.

To my grandparents, for their endless kindness and love. I am sorry that I cannot have all of them at my graduation but I know they would be proud.

Finally, to my biggest friend and also my girlfriend Raquel Guarita, my main source of motivation. Her patience and unconditional love and support makes me feel like I can accomplish anything if I have her by my side.

Resumo

Desde 2013, mais de 1,25 milhões de pessoas morrem por ano em acidentes rodoviários, tornando a segurança rodoviária um problema à escala global. No que diz respeito à proteção em colisões frontais e traseiras, é comum usar uma estrutura projetada para deformar de forma controlada em caso de colisão, evitando a deformação do habitáculo e acelerações excessivas nos passageiros, que podem levar a lesões graves ou até fatalidades.

Este trabalho centra-se no desenvolvimento de uma estrutura de alumínio deste tipo, visando um design otimizado, dentro dos parâmetros disponíveis para o projeto do veículo em que está incluído. Utilizando doftware comercial de Anáise de Elementos Finitos (FEA), um modelo da estrutura de absorção de energia para impacto frontal é desenvolvido e validado com um procedimento experimental de compressão quasi-estática. É desenvolvido um processo de otimização multi-objetivo, que pode ser adaptável às necessidades futuras do projeto. Várias alterações na geometria são testadas, com foco em défices específicos no desempenho da estrutura.

Através deste processo, um modelo FEA robusto e adaptável é alcançado e uma compilação da influência de vários parâmetros no desempenho em impacto é obtida. A estrutura otimizada mostra uma melhoria significativa no desempenho em caso de colisão frontal e, de acordo com os limites estabelecidos, espera-se que satisfaça os valores legais de segurança nos testes realizados pelas entidades responsáveis.

Palavras-chave: vigas de paredes finas, colisão frontal, absorção de energia, desempenho ao impacto, optimização multi-objectivo

Abstract

Since 2013, more than 1.25 million people die each year in road accidents, making road safety a global concern. With regard to protection in frontal and rear collisions, a common solution is to use a structure designed to deform in a controlled manner in the event of collision, avoiding deformation of the cabin and excessive accelerations in the passengers, which can lead to serious injuries or even fatalities.

This work focus on the development of an aluminum structure of this type, aiming for an optimized design, within the design parameters available for the vehicle project in which it is included. A Finite Element Analysis (FEA) model of the frontal energy absorption structure for frontal impact is developed and validated with a quasi-static compression experimental procedure. A multi-objective optimization process, that can be adaptable to the future needs of the project, is developed. Several changes in the geometry are tested, focusing on specific deficits in the performance of the structure.

Through this process, a robust and adaptable FEA model is achieved and a compilation of the influence of several parameters on the impact performance is obtained. The optimized structure shows a significant performance improvement in the event of a frontal collision and, according to the established limits, it is expected to satisfy the legal values of safety in the tests carried out by the responsible entities.

Keywords: thin-walled beams, front collision, energy absorption, crash performance, multi-objective optimization

Contents

Acknowledgments . . . iii
Resumo . . . v
Abstract . . . vii
List of Tables . . . xiii
List of Figures . . . xv
Nomenclature . . . xix
Glossary . . . xx

1 Introduction **1**
1.1 Motivation . . . 1
1.2 CEIIA . . . 2
1.3 Context . . . 3
1.4 Objectives . . . 5
1.5 Thesis Outline . . . 6

2 Available Solutions **7**
2.1 Related Work . . . 7
2.1.1 Thin-Walled Beams . . . 7
2.1.2 Materials . . . 8
2.1.3 Cross Section . . . 10
2.1.4 Variable Thickness . . . 11
2.2 Regulations . . . 11
2.3 Front Bumper . . . 14

3 Design Approach **17**
3.1 Material Choice . . . 17
3.2 Material Model . . . 19
3.3 Relevant Tests . . . 21
3.3.1 Static vs Dynamic Problems . . . 22
3.3.2 Linear vs Non-Linear Behavior . . . 23
3.3.3 Implicit vs Explicit Analyses . . . 24
3.4 Crashworthiness Criteria . . . 28

4 Quasi-Static Approach **31**
4.1 FEA Model . . . 31
4.1.1 Geometry . . . 32
4.1.2 Meshing . . . 33
4.1.3 Setup . . . 36
4.1.4 Results . . . 41

5 Validation Procedures **43**
5.1 Material Model Validation . . . 43
5.1.1 Experimental Procedure . . . 43
5.1.2 Experimental Results . . . 45
5.1.3 Material Model Curve Fitting . . . 47
5.2 Quasi-Static Model Validation . . . 47
5.2.1 Quasi-Static Numerical Model Changes . . . 48
5.2.2 Experimental Compression Test . . . 49

6 Dynamic Approach **53**
6.1 Dynamic Setup . . . 54
6.1.1 Initial Velocity . . . 54
6.1.2 Added Mass . . . 55
6.2 Quasi-Static vs Dynamic Model . . . 56

7 Structure Optimization **59**
7.1 Performance Evaluation Using Pareto Analysis . . . 60
7.2 First Iteration . . . 61
7.2.1 Parameters . . . 62
7.2.2 Results . . . 62
7.3 Second Iteration . . . 65
7.3.1 Parameters . . . 65
7.3.2 Results . . . 66
7.4 Third Iteration . . . 69
7.4.1 Parameters . . . 69
7.4.2 Results . . . 70
7.5 Fourth Iteration . . . 72
7.5.1 Parameters . . . 72
7.5.2 Results . . . 73
7.6 Final Results . . . 75

8 Conclusions **79**
8.1 Achievements . . . 79
8.2 Future Work . . . 80

Bibliography **81**

A Optimization Process Force vs Displacement Curves **87**

A.1 First Iteration 87

A.2 Second Iteration 89

A.3 Third Iteration 91

A.4 Fourth Iteration 92

B Optimization Process Results **95**

B.1 First Iteration 95

B.2 Second Iteration 96

B.3 Third Iteration 97

B.4 Fourth Iteration 98

List of Tables

1.1 Examples of vehicle categories [19] 4

3.1 Aluminum alloys (adapted from [60]) 18
3.2 Aluminum tempers (adapted from [60]) 18
3.3 Explicit and implicit choice criteria (adapted from [72]) 24
3.4 Advantages and disadvantages of implicit and explicit analysis (adapted from [72]) 25

4.1 5 mm element size vs 2.5 mm element size energy absorption 35
4.2 Aluminum 6061 T6 properties 36
4.3 Quasi-static model data 41

5.1 Sample measurements 44
5.2 Results average 46
5.3 Aluminum 6063 T6 properties 46

6.1 Energy absorption of quasi-static and dynamic models 57
6.2 Maximum forces and accelerations of quasi-static and dynamic models 57

7.1 First iteration geometries 62
7.2 First iteration geometry choice 64
7.3 Second iteration geometries 66
7.4 Second iteration geometry choice 67
7.5 Third iteration geometries 69
7.6 Third iteration geometry choice 70
7.7 Fourth iteration geometries 72
7.8 Fourth iteration geometry choice 74
7.9 Initial vs final geometries measurements 75
7.10 Initial vs final geometries comparison 75

B.1 First iteration results 95
B.2 Second iteration results 96
B.3 Third iteration results 97
B.4 Fourth iteration results 98

List of Figures

1.1 CEIIA headquarters [15] . . . 2
1.2 Autonomous vehicle Be [18] . . . 3
1.3 Product engineering team flow chart (icons from [20]) . . . 4

2.1 Thin-walled beams [22] . . . 7
2.2 Aluminum extruded tubes [28] . . . 8
2.3 CFRP tubes [36] . . . 10
2.4 Short fiber reinforced thermoplastic [37] . . . 10
2.5 Deformation in different shaped beams [12] . . . 10
2.6 Variable thickness [43] . . . 11
2.7 40% overlap test [49] . . . 12
2.8 ECE impact device (adapted from [50]) . . . 12
2.9 NHTSA pendulum device (adapted from [50]) . . . 12
2.10 Stars score by NCAP [54] . . . 13
2.11 Fixed barrier NCAP front crash test [53] . . . 13
2.12 Deformable barrier NCAP 40% offset front crash test [53] . . . 13
2.13 RCAR fixed bumper structure [55] . . . 14
2.14 Front rail structure [56] . . . 15
2.15 Front bumper beam connected to crash boxes [59] . . . 15

3.1 Johnson-Cook formulation stress strain curve . . . 19
3.2 NHTSA front crash test [71] . . . 22
3.3 Examples of static, quasi static and dynamic problems (adapted from [72]) . . . 22
3.4 Comparison between quasi static and dynamic applied force [72] . . . 23
3.5 Range of application of implicit and explicit analysis [72] . . . 24
3.6 Cost vs complexity in implicit and explicit analysis [72] . . . 25
3.7 Explicit flow chart (adapted from [72]) . . . 26
3.8 Force vs displacement diagram (adapted from [75]) . . . 29

4.1 Flowchart of the process used to build the numerical model . . . 31
4.2 Bumper geometry measurements . . . 33
4.3 Crash box cross section (adapted from [76]) . . . 33

4.4 Transverse beam cross section (adapted from [76]) . . . 33
4.5 Complete bumper structure . . . 34
4.6 Structure midsurfaces . . . 34
4.7 Comparison between the model results with a 5 mm element size and a 2.5 mm element size . . . 35
4.8 Mesh with triangles . . . 36
4.9 Corrected mesh . . . 36
4.10 Rigid body . . . 38
4.11 Infinite wall . . . 38
4.12 Boundary conditions and velocity . . . 39
4.13 Spotweld connection . . . 39
4.14 *HyperCrash*^{TM} model tree . . . 40
4.15 Complete model . . . 40
4.16 Deformed structure with plastic strain colored elements . . . 41
4.17 Quasi-static test force-displacement curve . . . 41

5.1 Samples cut from the extrusion tubes . . . 44
5.2 Sample measurements . . . 44
5.3 Width (green) and thickness (red) measurement points . . . 44
5.4 Tensile test setup . . . 45
5.5 Tensile tests output curves . . . 46
5.6 Johnson Cook material model curve compared with tensile test results . . . 47
5.7 Compression procedure specimen measurements . . . 48
5.8 Adapted quasi-static model force vs displacement curve . . . 48
5.9 Half structure quasi-static model . . . 49
5.10 Half-structure force vs displacement curve . . . 49
5.11 Fixing strategy for the compression procedure . . . 50
5.12 Final setup for the compression procedure . . . 50
5.13 Compression procedure force-displacement curves . . . 50
5.14 Final shape of the 4 compressed crash boxes . . . 51
5.15 Comparison between the computational model, the expected result [81] and the obtained result . . . 51
5.16 Experimental results vs quasi-static model . . . 52

6.1 Initial velocity of 50 Km/h added to all nodes . . . 55
6.2 Mass added to the rigid bodies . . . 55
6.3 Comparison between quasi-static and dynamic tests . . . 56
6.4 Comparison between quasi-static and CFC 1000 filtered dynamic test . . . 56

7.1 Example size of an exhaustive test procedure . . . 59

7.2 Pareto set example (adapted from [85]) . . . 61
7.3 Parameters that will be changed in the first iteration . . . 62
7.4 Example of data gathering (Geometry 12) . . . 63
7.5 Pareto set of first iteration (each point corresponds to a different geometry) . . . 63
7.6 Comparison between the reference geometry and geometry 12 force-displacement curves 64
7.7 Comparison between reference geometry and geometry 12, before and after the impact . 65
7.8 Parameters that will be changed in the second iteration . . . 66
7.9 Pareto set of second iteration . . . 67
7.10 Comparison between the reference geometry and geometry 21 force-displacement curves 68
7.11 Comparison between the reference geometry and geometry 21 before and after the impact 68
7.12 Parameters that will be changed in the third iteration . . . 69
7.13 Pareto set of third iteration . . . 70
7.14 Comparison between the reference geometry and geometry 6 force-displacement curves 71
7.15 Comparison between the reference geometry and geometry 6 before and after the impact 71
7.16 Parameters that will be changed in the fourth iteration . . . 73
7.17 Pareto set of fourth iteration . . . 73
7.18 Comparison between the reference geometry and geometry 8 force-displacement curves 74
7.19 Comparison between the reference geometry and geometry 8 before and after the impact 74
7.20 Comparison between the initial geometry and the resultant of the optimization process . . 75
7.21 Final Pareto distribution . . . 76

A.1 Force-displacement curves of the first iteration (geometries with L = 300 mm) . . . 87
A.2 Force-displacement curves of the first iteration (geometries with L = 400 mm) . . . 88
A.3 Force-displacement curves of the first iteration (geometries with L = 500 mm) . . . 88
A.4 Force-displacement curves of the first iteration (geometries with L = 600 mm) . . . 88
A.5 Force-displacement curves of the second iteration (geometries with D = no and R = straight) 89
A.6 Force-displacement curves of the second iteration (geometries with D = no and R = 3200 mm) . . . 89
A.7 Force-displacement curves of the second iteration (geometries with D = no and R = 2000 mm) . . . 89
A.8 Force-displacement curves of the second iteration (geometries with D = yes and R = straight) . . . 90
A.9 Force-displacement curves of the second iteration (geometries with D = yes and R = 3200 mm) . . . 90
A.10 Force-displacement curves of the second iteration (geometries with D = yes and R = 2000 mm) . . . 90
A.11 Force-displacement curves of the third iteration (squared section) . . . 91
A.12 Force-displacement curves of the third iteration (circular section) . . . 91
A.13 Force-displacement curves of the third iteration (hexagonal section) . . . 91

A.14 Force-displacement curves of the third iteration (triangular section) 92
A.15 Force-displacement curves of the fourth iteration (geometries with Z = 20 mm) 92
A.16 Force-displacement curves of the fourth iteration (geometries with Z = 40 mm) 92
A.17 Force-displacement curves of the fourth iteration (geometries with Z = 60 mm) 93

Nomenclature

c	Speed of sound
C	Damping matrix
C_v	Constant volume specific heat
CFE	Crash force efficiency
CS	Crashworthiness score
E	Young's modulus
E_k	Kinetic energy
f_{int}	Internal forces
f_{ext}	External forces
$F_{contact}$	Contact forces
G	Shear Modulus
F_{max}	Peak crash force
K	Stiffness matrix
l	Length of the element
M	Mass matrix
t	Time
T	Temperature
T_{melt}	Melting temperature
T_{room}	Ambient temperature
SEA	Specific energy absorption

Greek symbols

δ	Displacement

ε	Strain
$\dot{\varepsilon}$	Strain rate
$\bar{\varepsilon}^p$	Effective plastic strain
ν	Poisson's ratio
ρ	Specific weight
σ	Stress
$\bar{\sigma}$	Effective stress
σ_{yield}	Plasticity yield stress
$d\varepsilon_{ij}$	Plastic strain tensor
ΔT	Temperature change
Δt	Time step

Subscripts

cr	Critical
max	Maximum
min	Minimum

Superscripts

*	Nondimensional
o	Reference

Glossary

CAD Computer Aided Design.

CEIIA Centro para a Excelência e Inovação na Indústria Automóvel.

CFC Channel Frequency Class.

CFRP Carbon Fiber Reinforced Plastic.

CMS Crash Management System.

EA Energy Absorption.

ECE Economic Commission for Europe.

FDM Finite Difference Method.

FEA Finite Element Analysis.

FMVSS Federal Motor Vehicle Safety Standards.

GFRP Glass Fiber Reinforced Plastics.

HIC Head Injury Criterion.

NCAP New Car Assessment Programme.

NHTSA National Highway Traffic Safety Administration.

RCAR Research Council for Automotive Repairs.

WHO World Health Organization.

Chapter 1

Introduction

1.1 Motivation

Since the introduction of automobile structures mass production by Henry Ford in 1913 [1], a continuous technological development in road vehicles took place. The majority of the consequences for the world society have been positive but, with the increasing in the number of vehicle and travel speeds, the fatalities caused by crashes have become a major concern [2]. According to the World Health Organization (WHO), by the year 2030, road accidents will reach fifth place among the leading death causes in the world [3], making the development of automotive safety systems a vital subject for research.

In order to improve the road safety worldwide, numerous works have been made aiming for a decrease in vehicle crashes and an improvement of the ability of the vehicle to protect the occupants against injury. With the development of safety systems in automotive industry, the number of deaths between 2005 and 2014 in the EU have decreased from 46,000 to 26,000 [4]. Citing Ashwin Sheshadri, the ability of the vehicle to absorb energy and to prevent occupant injuries in the event of an accident is referred to as ”Crashworthiness” [5]. This ability can be improved by developing more efficient Energy Absorption (EA) systems and has been studied by many authors [6, 7, 8, 9] due to its relevance.

In the case of frontal crash, the main automotive part which undergoes impact stress is the bumper [10]. This makes the study of bumper's design and manufacturing a relevant and crucial subject. Bumpers are solid structures that should be stiff enough to maintain the integrity of the cabin and have sufficient ductility to suffer plastic deformation, in the case of metals, to absorb kinetic energy transmitted during the collision process. In most cases, bumpers are simple structures, composed by one or more beams connected to the vehicle's chassis. The connection between these components is one of the focal points for some studies [11], as they represent weak spots in the structure.

As the industry strives for the reduction in automobile weight, associated to the urgent cutback in carbon emissions, a need for lightweight structures emerged. One of the most studied solutions is the use of thin-walled structures due to their advantages not only light weight but also low price, high strength and stiffness, high reliability and excellent energy absorption capacity [12]. These structures are used across almost all the fields of engineering and have a vital role in the present industry. The

crashworthiness is analyzed taking into account representative factors, making easier the comparison between different options and the improvement of old structures. Material, section shape and wall thickness represent the most studied factors. The behaviour of the structures when loads are applied is the object of several studies as well as the viability and validation of computational tools to analyze representative cases of loading and impact [13, 14].

Numerical softwares have been progressively developed to obtain a good approximation to structure behaviour in a wide variety of load or crash situations. This work is focused on the computational modeling and model validation of a front impact structure, and was performed in a product development team environment.

All the tools for the completion of the computational model as well as validation tests where provided by CEiiA. This work would not be possible without these tools and the integration in the team that is performing the development of the company's first electrical M1 class car, the Be2 project. Front impact energy absorption structures play a crucial role in the vehicle's homologation tests.

The present thesis was performed in order to obtain the Master of Science in Aerospace Engineering. For the automotive industry, crash situations are much more common than in aerospace world. However, the numerical model developed in this thesis can be implemented to an aircraft for a crash situation or for other types of static or dynamic load cases that are needed when evaluating an aircraft structure. The multi-objective performance evaluation process used in this work, can also be a great tool for any industry, including aeronautics.

1.2 CEIIA

CEiiA is a private non-profit organization, created in 1999 and located in Matosinhos, Portugal. The organization is a center of engineering and product development that designs and implements innovative products and systems and is associated with technical universities and some of the automotive and aeronautic market leaders. One of the main concerns of this organization, is the community where it is inserted, reflecting in a wide variety of technological and sustainable solutions. Figure 1.1 shows CEiiA's headquarters.

Figure 1.1: CEIIA headquarters [15]

In the mobility sector, CEiiA was responsible for the creation of mobi.me, a fully integrated and user-

centric management of mobility devices [16]. Also the company was responsible for the implementation of a scooter sharing platform in several European cities as well as a bike sharing service in Cascais.

One of the latest projects of the company is the Be project. The main goals of this project are [17]:

- To attract new investment associated to new logic's of motorization and mobility services;
- To develop a national industrial cluster with capacity to design, develop, industrialize and test electric vehicles and integrated services for the new environments of sustainable mobility;
- To position Portugal as a world reference in Electric Mobility and export an integrated solution [system, service and vehicle].

In 2016, CEiiA presented Be, an autonomous vehicle, designed to work as an on-demand vehicle. Figure 1.2 is a photo of the functional prototype.

Figure 1.2: Autonomous vehicle Be [18]

1.3 Context

CEiiA's next goal is to create Be2, a M1 class electric powered and road safe vehicle that can be implemented in the sharing platform mobi.me. M1 class vehicles, are vehicles used for carriage of passengers, with a maximum of 9 passengers including the driver. Some examples of this and other vehicle categories are listed in Table 1.1.

Table 1.1: Examples of vehicle categories [19]

Category	Description
M	Motor vehicles with at least four wheels designed and constructed for the carriage of passengers
M1	Vehicles designed and constructed for the carriage of passengers and comprising no more than eight seats in addition to the driver's seat
M2	Vehicles designed and constructed for the carriage of passengers, comprising more than eight seats in addition to the driver's seat and having a maximum mass not exceeding 5 tonnes
M3	Vehicles designed and constructed for the carriage of passengers, comprising more than eight seats in addition to the driver's seat and having a maximum mass exceeding 5 tonnes
N	Motor vehicles with at least four wheels designed and constructed for the carriage of goods
O	Trailers (including semi-trailers)

The product engineering team is responsible for the design and development of any mobility product developed by CEiiA. Designers and engineers create a solution from paper to final product, always maintaining the concept as a priority. The work flow of the company is represented in Figure 1.3.

Every project starts from the design. Taking into account the features that the product will have, a group of product designers develop an innovative, attractive and user-friendly concept and the engineering team is responsible for making sure that all the regulations are respected and the features are implemented in the vehicle.

The packaging, systems implementation and structural analysis is performed by Computer Aided Design (CAD), embedded systems and structure engineers, and the structure is iterated until the problems are solved. Also in this phase, it is possible to create prototypes to check the functionality of the product or validate the computational models.

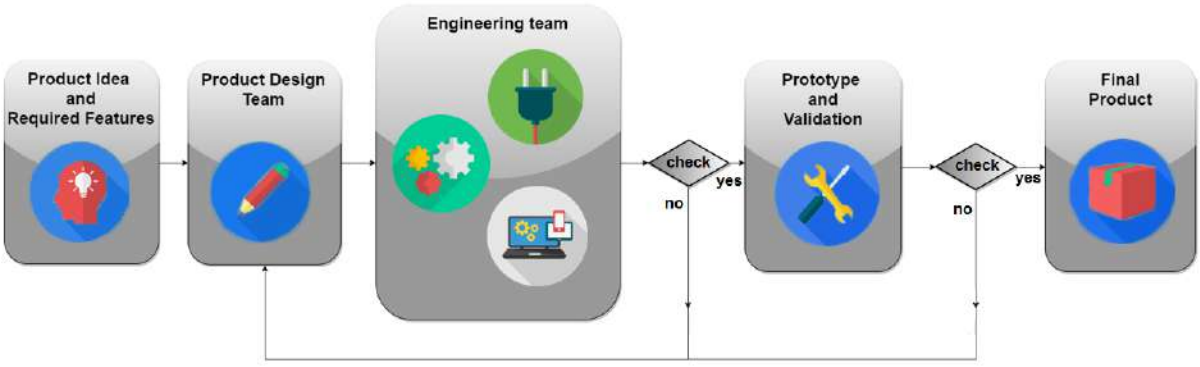

Figure 1.3: Product engineering team flow chart (icons from [20])

This work was performed with daily direct contact with all the members of the product engineering team, working on structure analysis and focusing on a crash Finite Element Analysis (FEA), in particular on a structure that will be responsible for the controlled absorption of kinetic energy when a frontal

impact occurs. This structure is commonly called Front Crash Management System (CMS) and should absorb most of the energy of a front collision stopping the vehicle and minimizing deformation in the chassis.

1.4 Objectives

In order to meet CEiiA's expectations, as well as creating scientific value, this work is focused on obtaining a final optimized solution for the Front CMS of an M1 class vehicle.

Due to the early stage of the Be2 project, some assumptions will be made. It is important to have a method that can be changed to meet the requirements of the project in the future. The quality of the structure should be evaluated taking into account the current regulations related to automotive crash safety and occupants biomechanical injury limits. A crash performance evaluation tool should also be developed to meet the goals of the project.

A numerical model that represents, as closely as possible, a real collision will be created and used to evaluate different solutions. Using suitable criteria, an evaluation process will be used to access the quality of the structures and understand the influence of a set of parameters in the crash performance of the structure. The model will then be validated using the available experimental procedures, provided by the organization.

By the end of this work, several goals should be achieved:

- A robust numerical model for a complete front bumper structure in a full overlap front crash situation that can be changed to meet the future requirements of the project;
- A multi-objective optimization procedure that allows the improvement of the structure, in terms of the project goals;
- An optimized solution that is expected to perform well in the tests specified by the responsible entities regarding front collision of vehicles.

The focus of this work is the study of a complete front bumper structure in terms of energy absorption and deformation. The computational model must represent a crash situation and provide data that allow to evaluate the performance of the structure and improve it. Taking this into account, the model must affect all the parts of the structure in a typical crash situation. The most common front crash test performed by the entities responsible for the assessment of vehicle safety systems is the full overlap test. In this work, a model of the bumper structure will be made and analyzed in a full overlap impact against a rigid wall. The deformation pattern and range, as well as the energy absorption ability of the structure must be the focus of its development.

1.5 Thesis Outline

In the first chapter the motivation behind the study of front impact protection systems was made and the context of the work in a company environment, as well as the main goals of this work, were explained.

Chapter 2 makes a summary of the studies made about this subject and the regulations and safety procedures that are usually made to front impact passive safety structures.

Chapter 3 covers the problem approach, including the material choice, material model explanation, tests and numerical software choice and quantitative criteria for the structure dimensioning study.

Chapter 4 looks at the quasi-static numerical model development, setup and results, explaining the inputs and outputs of the model.

In Chapter 5 the validation of the material and quasi-static models are validated. The experimental procedures are described and compared with the numerical models.

Chapter 6 comprehends the conversion from quasi-static to a dynamic model, comparing both in terms of force-displacement curve and deformation pattern.

In Chapter 7, the multiobjective optimization method and process is explained and four iterations to the structure are made using this process.

Finally, Chapter 8 compiles the achievements of this work and leaves recommendations for future works regarding front impact energy absorption structures.

Chapter 2

Available Solutions

2.1 Related Work

Before starting to work on a solution, it is important to gather information about the studies related to the present challenge and the solutions that have already been developed, to know the best way to approach the problem. It is also important to know the regulations regarding crash safety. In this phase, several articles regarding energy absorption structures and techniques will be taken into account.

2.1.1 Thin-Walled Beams

Due to all the advantages that this type of structures bring to several industries, thin-walled beams are one of the most studied components when talking about structural design. Having high stiffness as well as being lightweight structures, the versatility of thin-walled structures is almost endless. The evolution of material and fabrication technologies motivates studies of this type of beams using different materials, geometries and sections as will be described in the following sections. The energy absorption characteristics of metallic tubes under various load conditions have received extensive investigations including axial crushing, lateral crushing, transverse bending and others [21]. In Figure 2.1 several metallic thin-walled beams are represented with a variety of sections.

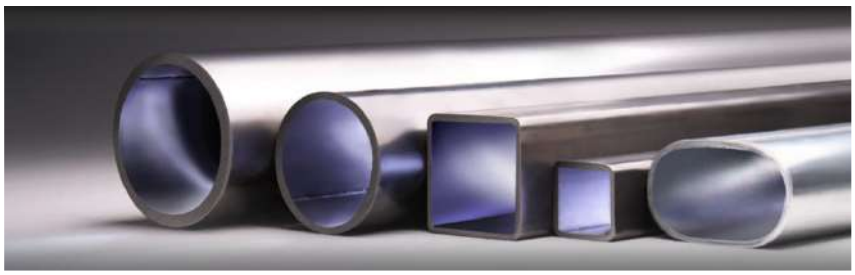

Figure 2.1: Thin-walled beams [22]

2.1.2 Materials

Metals

Metallic materials are responsible for about 80% of the total automobile weight, having plastics, rubbers, glass, paints, and textiles contributing with the rest [23].The group of metallic materials used by the automotive industry includes steel, cast iron, sintered metals, aluminum alloys, magnesium alloys, metal-based composite materials, and various ceramic and metallic coatings [23].

One of the motives for the massive expansion of industry was the start of the use of steel. In the beginning of automotive industry, steel was and still is, the main vehicle's component, mainly high strength steel, that helped to keep structural stiffness while reducing mass [24, 25]. In 2004, the average light vehicle produced in North America contained 1013 Kg of steel (55% of the vehicle weight) and 150 Kg (8%), of iron [26].

The share of aluminum alloys among all the materials used to make car components has been continuously increasing, reducing the overall mass of a car. There are foresights claiming that within the next few years, the share of aluminum alloy castings in automobiles will double, mainly at the expense of reduced share of components made of steel and cast iron [23]. As a major class of energy-absorbing component, the sectional trusses or frames made of aluminum and its alloys are gaining growing popularity in a range of engineering designs mainly due to its low cost and high stiffness-to-weight ratio. Besides, aluminum alloys can be produced to almost any shape by using an extrusion process. Some examples of extruded aluminum sections are shown in Figure 2.2. For these design and manufacturing benefits, more and more new aluminum structural members with increasing complexity of sectional configurations are being introduced to further enhancing the structural integrity and crashworthiness.[27]

Figure 2.2: Aluminum extruded tubes [28]

Composite materials

Composite materials were introduced in the automotive world to improve the performance of motor sports vehicles. With the recent advances in this type of materials, their use is growing and becoming a serious option for the manufacturers. Advanced composites have high strength and their rigidity also help to maintain same or higher level of safety than the conventionally used materials in aerospace and automotive industries [29]. The primary advantages of using composites is the weight reduction for the

same strength as the composites are up to 35% lighter than aluminum alloys and 60% lighter than steel and the use of composites in automotive can lead to an overall vehicle weight reduction of up to 10% [30]. The main problems in the use of this type of materials are the difficulty in the bonding process to other structures and the high price point in large series when compared to metallic extruded parts.

Fiber reinforced composites are made of two materials, a matrix that holds the reinforcements in place while transferring the forces from fiber to fiber, and the fibers that enhance the properties of the material. This enhancement can be focused in different parameters depending on the desired use for the component. Glass Fiber Reinforced Plastics (GFRP) consist in a plastic matrix reinforced with continuous or discontinuous glass fibers. The type of matrix, glass and the size and layout of the fibers influence the properties of the final material. Unidirectional composites have higher strength and modulus in the direction of the fiber axis and generally are very weak in the transverse direction. This is very advantageous when these composites are used in applications where the state of stress can be determined accurately so that laminates can be fabricated from the unidirectional laminae having strengths matched to the design needs. However, in applications where the state of stress may not be predictable or where it is known that the stresses are approximately equal in all directions, unidirectional composites or laminae may not be required or cost-effective [31]. One solution is to fabricate fiber reinforced composites with fibers aligned in more than one direction giving the composite approximately equal strengths in all directions. This can be done with layers of unidirectional fibers stacked in different angles, what makes the material isotropic in a plane or with short random oriented fibers that can provide a close to 3D isotropic behaviour to the material. This techniques can also be used to make thin-walled beams as shown in Figure 2.3. The tubes in the figure are made of a Carbon Fiber Reinforced Plastic (CFRP), a composite with carbon fibers used as reinforcement for a plastic matrix. In Figure 2.4, an example of a 3D printed part made out of a composite with short random oriented fibers is shown.

The primary use of carbon fibers is in aircraft and aerospace, where weight savings are a major objective. While its cost limits carbon use in commercial applications, it is used extensively where material content is low, such as sporting equipment [32]. In automotive sports, CFRP are widely used due to their excellence as crash energy absorbing components featured by excellent stiffness to weight ratio [33]. The main disadvantage is the price point. CFRP are expensive to manufacture due to the high price of carbon fibers. A good alternative is the use of GFRP. Glass fiber is substantially cheaper than carbon fiber and have a similar weight-volume ratio, making the components lighter than the metallic ones while maintaining the stiffness.

Several companies such as Audi, Ford, Mercedes-Benz, Toyota, Volkswagen, Volvo and others are including composite parts in their new models [29]. Some of the more recent studies about structural parts made of composite materials investigate the viability of Carbon Fiber Reinforced Plastic (CFRP) [33], Glass Fiber Reinforced Plastics (GFRP) [34] and foams [35].

Figure 2.3: CFRP tubes [36]

Figure 2.4: Short fiber reinforced thermoplastic [37]

2.1.3 Cross Section

The influence of tube cross section shape has been yet another subject of study. Metal extrusion processes made possible to fabricate a wide range of shapes mainly made of aluminum. Some of the studies approach the behaviour of different sections to several types of loads in order to understand the influence of the cross section in the behavior of the structures. W. Abramowicz and N. Jones studied circular [38] and square [39] tubes in crushing conditions as well as in progressive buckling [40]. More recently, the section influence have been studied in bending tests, analyzing and comparing the bending behavior of circular, ellipsoid, rectangle, trapezoid and even open sections, as well as the influence of ribbed [12] and multicell sections [27, 41]. The conclusions show that section choice can have a big influence in the crashworthiness of a beam even if the aspect ratio is maintained.

According to Tang et al. [12], the parameters related to geometry size along impact direction, such as: radius of circular section, radius ratio of elliptical section, side length ratio of rectangular section and height for hat section, have significant influence on crashworthiness of beams under lateral impact. Usually, the section with a larger size along impact direction will result in a better crashworthiness performance. Some of the tested sections are represented in Figure 2.5. Qiu et al. [41] concluded that multi-cell tubes perform better than other tubal configurations during axial compression.

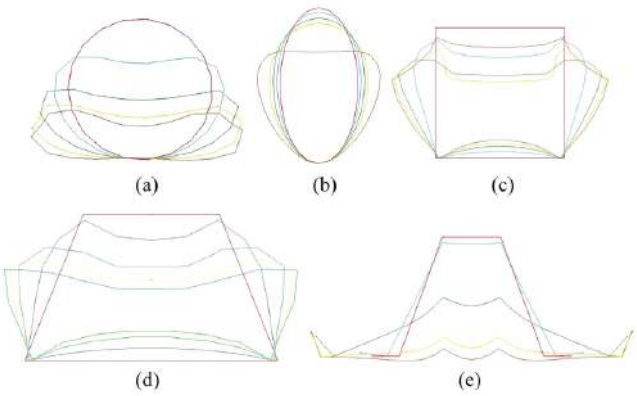

Figure 2.5: Deformation in different shaped beams [12]

2.1.4 Variable Thickness

In some cases, the deformation pattern of the protective Energy Absorption (EA) systems is more important than the ability to keep the shape. Several studies have been done to the influence of thickness distribution in structural beams aiming to control and manipulate the deformation of this components in case of high velocity or high load impact [42, 43, 44, 45, 46, 47]. The deformation pattern was found to be highly correlated with the wall thickness of the plates in the square section [21]. An example of a variable thickness square tube section is shown in Figure 2.6.

In terms of energy absorption, Zhang et al. [43] concluded that increasing the material in the corner regions can increase the energy absorption efficiency of a square tube. The energy absorption over mass ratio of the optimal design in this study was found to be about 40% higher than that of a uniform thickness design.

However, these studies represent a problem in the study of complex structures because they require the use of solid elements instead of shell elements, to take into account a variation in the walls thickness, which leads to higher computational time in the Finite Element Analysis (FEA).

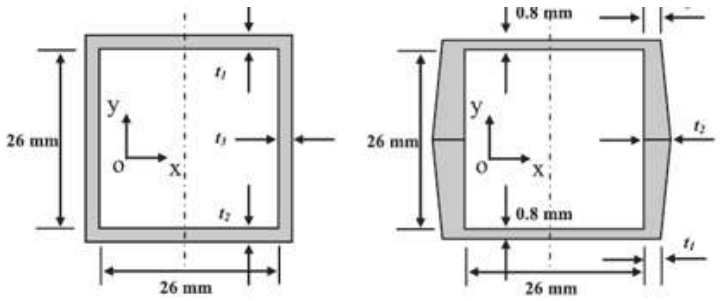

Figure 2.6: Variable thickness [43]

2.2 Regulations

When talking about automotive crash, there are several entities responsible to access the crash performance of road vehicles. The standard tests regulated by United Nations Economic Commission for Europe (ECE) and National Highway Traffic Safety Administration (NHTSA) in the U.S.A.. In these tests, the setup is defined by standard regulations and the results are compared to maximum values of accelerations and forces suffered by the dummies during the crash.

Currently in the U.S.A., the frontal impact testing with a rigid barrier (full overlap) at speeds up to 35 mph ($\simeq$ 56 km/h) is the primary mode for evaluating the front structure performance [48]. In Europe, however, the corresponding test has an offset (40% overlap) with a deformable barrier at 37.5 mph ($\simeq$ 60 km/h) [48], as shown in Figure 2.7.

Figure 2.7: 40% overlap test [49]

Another tests made by ECE are the longitudinal impact low speed test and the corner impact test. Both are done with the impact structure shown in Figure 2.8. The first test consists in two impacts at 4 km/h, one with empty weight and the other with gross weight, on the front end of the vehicle. In the second test, the vehicle is impacted in laded and unladed weight, but this time on the front corners at 2.5 km/h [50].

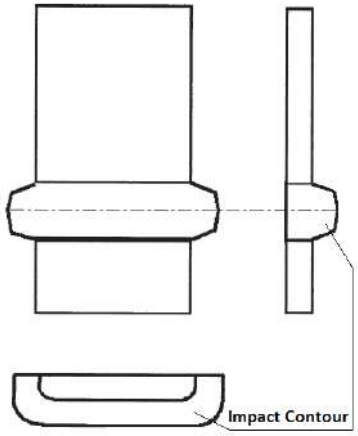

Figure 2.8: ECE impact device (adapted from [50])

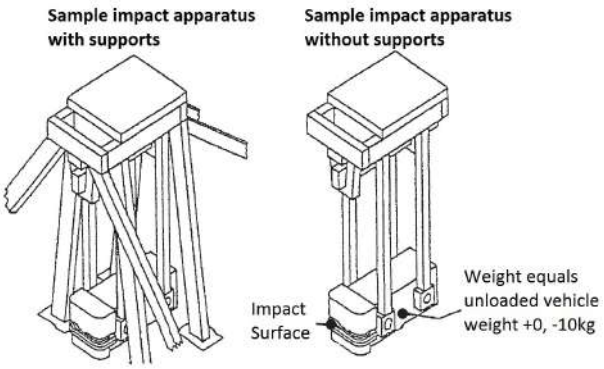

Figure 2.9: NHTSA pendulum device (adapted from [50])

NHTSA makes similar tests but with a pendulum structure, shown in Figure 2.9. The corner tests are made at 2.4 km/h and the front impact at 4 km/h. Also, a 4 km/h front impact is performed against a fixed collision barrier [50]. NHTSA issues Federal Motor Vehicle Safety Standards (FMVSS) to implement laws from Congress [51]. The main requirements to be within the safety limits are defined to the vital body parts, in particular chest and head, by three criteria: the Head Injury Criterion (HIC), defined by

$$HIC = \left[\frac{1}{t_2 - t_1}\int_{t_1}^{t_2} a dt\right]^{2.5}(t_2 - t_1), \tag{2.1}$$

is limited by a maximum allowable value of 1000, being a the resultant acceleration expressed as a multiple of g, and $t1$ and $t2$ are any two points in time during the crash of the vehicle which are within a 15 ms time interval; the chest must not suffer a compression superior to 76.2 mm and an acceleration higher than 60 G's. These standards are defined by FMVSS [52] for an impact in a fixed barrier either perpendicular or at a 30 degree angle at a speed of 30 mph ($\simeq$ 48 km/h) for the front-seated Hybrid III

dummy occupants [48].

In order to give the consumers a better qualitative idea of the crashworthiness and safety of a vehicle, some independent associations started to test a great number of vehicles available in the market and developed scoring systems. Two of the most relevant entities performing these tests are Research Council for Automotive Repairs (RCAR) and New Car Assessment Programme (NCAP). Today it is possible to have an idea of the safety of a vehicle in many fields just by checking NCAP's website [53]. The performance is represented in a score by stars (1 to 5) taking into account HIC and chest G's as represented in Figure 2.10.

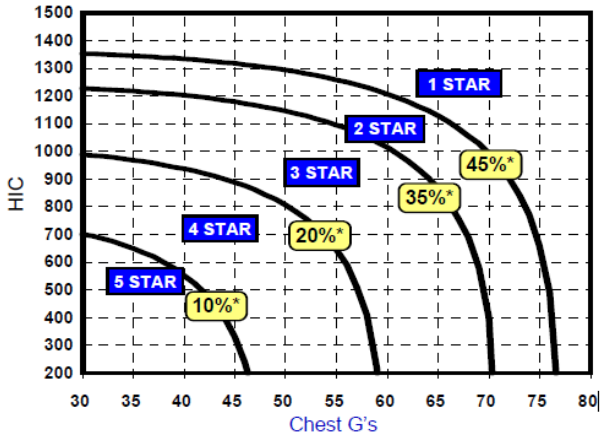

Figure 2.10: Stars score by NCAP [54]

This score gives a probability for serious injury with each level, meaning that vehicles with 1 star have up to 45% probability of serious injury in a crash similar to the one performed by NCAP, 2 stars have up to 35% and so on, up to a score of 5 stars with a probability of serious injury of only 10%.

NCAP's frontal impact tests consist in a frontal impact test into a fixed barrier at 50 km/h and a 40% overlap impact onto a deformable barrier at 64 km/h as shown in Figures 2.11 and 2.12.

Figure 2.11: Fixed barrier NCAP front crash test [53]

Figure 2.12: Deformable barrier NCAP 40% offset front crash test [53]

RCAR focus in low impact tests to access the resistance of the structures to low speed impacts and prevent the occurrence of deformations and the need for repairs. They perform two types of tests. The first is a low speed offset crash test. This test is similar to NCAP offset crash test with 40% offset but is performed at 15 km/h and the barrier is not deformable. The other test consists in a better simulation

of a real front crash between two vehicles being performed at 10 km/h and impacting the vehicle onto a fixed bumper structure, as shown in Figure 2.13.

Figure 2.13: RCAR fixed bumper structure [55]

Knowing the different tests and requirements, it is possible to design the structure with a good performance level in sight.

2.3 Front Bumper

On impact, the structure of a vehicle has two main functions: absorb kinetic energy of the vehicle while keeping an allowable deceleration for the survival of occupants and preserve the integrity of the passenger compartment and so avoid the intrusion of rigid components into it [56]. In the situation of frontal impact, the first part of the vehicle to make contact is the front structure. The components responsible for most of the absorption in this situation are the front bumper and the longitudinal rails that the bumper is connected to. This brings a major relevance to the structural design of these structures to improve their Energy Absorption (EA) performance.

Along the years in automotive evolution, the vehicles started to have progressive deformation zones to absorb some of the kinetic energy from the impact through controlled plastic deformation [57].

Usually, the bumper subsystem consists of a bumper transverse beam made of impact-absorbing materials connected to the structural components and a cover that has both aesthetic and protection purposes. The bumper subsystem is then connected to the longitudinal front rail. In most conventional vehicles the front rail is made up of two parts: a replaceable piece called the crash box (A) which folds in a controlled pattern under impact, a second part, the frame rail, with an initial section which also folds in a controlled pattern (B) and a second section which transmits the force to the vehicle structure (C) [56]. An example is shown in Figure 2.14.

Among those elements, the bumper beam and the crash boxes are the main structural components. They are expected to be deformable enough to absorb the impact energy, to reduce the risk of injury for pedestrians and other vulnerable road users but, at the same time, should also have sufficient strength and stiffness to give place to small intrusion of the engine compartment and, therefore, to protect the nearby vehicle components [58]. An example of a bumper beam connected to the crash boxes is repre-

sented in Figure 2.15.

In a well designed structure with these main components, it is possible to have a controlled deformation, resulting in a suitable energy absorption process in the case of a crash that prevents the occurrence of high deceleration that can hurt the passengers.

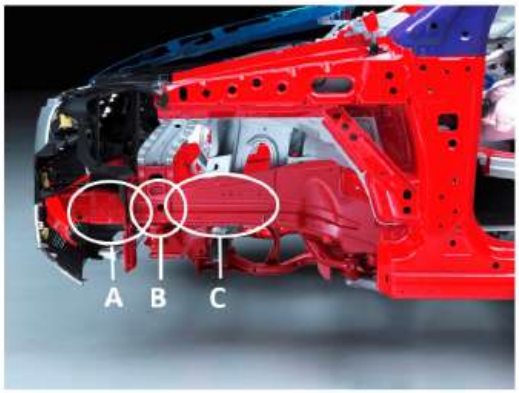

Figure 2.14: Front rail structure [56]

Figure 2.15: Front bumper beam connected to crash boxes [59]

Chapter 3

Design Approach

Considering a typical structure similar to the one described in the end of the previous chapter, the type of analysis and material model as well as the criteria for the performance evaluation of the structure will be discussed in this chapter.

3.1 Material Choice

In the beginning of the design phase it is important to study the benefits of the available materials and choose a suitable one for the structure. The most common solution is steel but, as referred in the previous chapter, in the automotive industry there are better options in terms of cost and weight savings.

Composites have been studied and are a good option. This type of material can be even better than metal alternatives but the properties are more difficult to reproduce in the numerical model and failure models and are less accurate. Being the focus of this work an impact focused structure, complex deformations are expected so the model should have the best possible correlation with reality.

Aluminum have been used in many automotive applications. The versatility of this metal is the existing variety of alloys and mechanical and thermal treatments that can be done to this metal to make it serve a wide range of purposes. Following European standards, the different alloys can be designated by chemical composition or by a 4 digit designation. The first digit defines the alloy group, as listed in Table 3.1. The second indicates modifications of the original alloy or impurity limits and the last two digits define the alloy [60].

The 6061 magnesium and silicon alloy is the best choice whenever welding or brazing is required. It has structural strength and robustness, good resistance to corrosion and good machining characteristics. This alloy is used extensively as building material, the most common being in the production of components for aircraft, shipping and automobiles [61].

Table 3.1: Aluminum alloys (adapted from [60])

Definition of Alloy Group	Group	*
Aluminum 99.00 percent and greater	1XXX	(H)
Aluminum alloys grouped by major alloying elements		
Copper (Cu)	2XXX	(T)
Manganese (Mn)	3XXX	(H)
Silicon (Si)	4XXX	(H/T)
Magnesium (Mg)	5XXX	(H)
Magnesium and Silicon (Ma + Si)	6XXX	(T)
Zinc (Zn)	7XXX	(T)
Other elements (e.g. Fe, Li,...)	8XXX	(H/T)
Unused series	9XXX	(-)

* H = work hardening (non-heat-treatable), T = heat-treatable

For automotive structural purposes, the most used alloys are the ones of the series 6 and 7 because they have high stiffness and are heat treatable [62]. The heat treatment makes possible a change in the mechanical properties of the metal to fulfill to the demands of the design. Some types of heat treatment are listed on Table 3.2.

Table 3.2: Aluminum tempers (adapted from [60])

Temper	Process
T4	Solution heat treated and naturally aged to a stable condition
T6	Solution heat treated and artificially aged to maximum strength
T7	Solution heat treated and naturally overaged
T8	Solution heat treated,cold worked and artificially aged
T9	Solution heat treated, artificially aged and cold worked

In the present work, a T6 heat treatment will be used, because it is more suitable for energy absorption structures due to its maximizing strength [62].

3.2 Material Model

To get the best correlation between the FEA model and a real crash test, it is important to chose the appropriate theoretical model to simulate the properties of the material being tested. The most common way for taking account plasticity is to set a tabulated function that gives the link between stresses and plastic strains [63]. The problem with this approximation is that it does not consider the changing in properties of the materials with different conditions. A solution is to use a model that has been used in similar studies and proven to work for similar cases with the best proximity to the real impact test. In this case, a suitable model needs to have some validation tests already done for low speed impact tests.

In impact analysis, the material constitutive law should include strain rate dependency for both material deformation and failure [64]. G. R. Johnson and W. Cook made several studies [65, 66] and developed a model that respect this requirement. This model was used and validated by some authors for low and high velocity impact situations [63, 64, 67, 68]. Some papers focus in the study of strain-rate forms implemented in modified Johnson-Cook constitutive model and conclude that the standard model strain-rate form provides the best overall comparison with the data [68]. Considering these results, it is expected that this model will fit the crash tests intended by the present study and have good correlation with the experimental results.

Using Johnson-Cook formulation, the material stress strain curve is built in two parts as shown in Figure 3.1 and introduced in the numerical model.

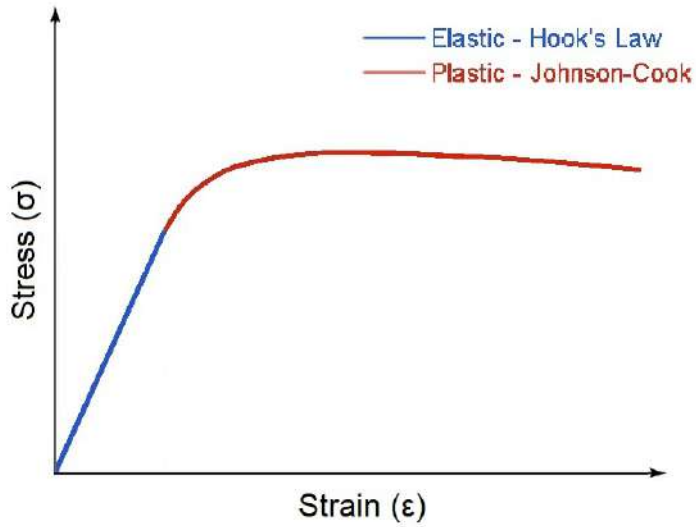

Figure 3.1: Johnson-Cook formulation stress strain curve

Before the start of the plastic deformation, the stress-strain curve is linear, respecting Hook's Law,

$$\sigma = E\varepsilon \tag{3.1}$$

where σ is the stress, E Is the Young's modulus and ϵ is the strain.

Introducing Poisson's ratio (ν), the shear modulus (G) can be calculated as [69]

$$G = \frac{E}{2(1+\nu)} \tag{3.2}$$

and the 3D generalized Hook's Law for homogeneous isotropic material can be used [69]

$$\varepsilon_x = \frac{\sigma_x}{E} - \frac{\nu\sigma_y}{E} - \frac{\nu\sigma_z}{E}, \quad \varepsilon_y = \frac{\sigma_y}{E} - \frac{\nu\sigma_x}{E} - \frac{\nu\sigma_z}{E}, \quad \varepsilon_z = \frac{\sigma_z}{E} - \frac{\nu\sigma_x}{E} - \frac{\nu\sigma_y}{E} \tag{3.3}$$

The shear stress is calculated as

$$\tau_{xy} = G\gamma_{xy}, \quad \tau_{yz} = G\gamma_{yz}, \quad \tau_{xz} = G\gamma_{xz}, \tag{3.4}$$

, where τ is the shear stress and γ the shear strain [69].

When the stress reaches the yield strength value of the material, the plastic strain starts. After this point, the curve is defined by Johnson-Cook Flow Surface.

The Johnson-Cook Flow Surface is [67]

$$\sigma = [A + B(\bar{\varepsilon}^p)^n]\,[1 + Cln(\dot{\varepsilon}^*)][1 + (T^*)^m], \tag{3.5}$$

where A, B, C, n and m are constants, σ is the stress value in the plastic regime, T^* is the non-dimensional temperature defined as

$$T^* = \frac{T - T_{room}}{T_{melt} - T_{room}}, \tag{3.6}$$

being T the current temperature of the material, T_{room} the ambient temperature and T_{melt} is the melting temperature. Adiabatic conditions are assumed such that all plastic work is converted into temperature change, i.e.

$$\Delta T = \frac{\bar{\sigma}\bar{\varepsilon}^p}{\rho C_v}, \tag{3.7}$$

where $\bar{\sigma}$ is the effective stress, $\bar{\varepsilon}^p$ is the effective plastic strain, ρ is the mass density, and C_v is the constant volume specific heat. The effective plastic strain $\bar{\varepsilon}^p$ is defined by

$$\bar{\varepsilon}^p = \int_0^t d\bar{\varepsilon}^p, \tag{3.8}$$

where the incremental plastic strain $d\bar{\varepsilon}^p$ is determined from the incremental plastic strain tensor $d\varepsilon_{ij}$, such that

$$d\bar{\varepsilon}^p = \sqrt{\frac{2}{3} d\varepsilon_{ij} d\varepsilon_{ij}}. \tag{3.9}$$

The effective stress $\bar{\sigma}$ is defined by

$$\bar{\sigma} = \sqrt{\frac{3}{2} \sigma_{ij} \sigma_{ij}}. \tag{3.10}$$

The non-dimensional strain rate $\dot{\varepsilon}^*$ is the ratio of the effective plastic strain rate $\dot{\bar{\varepsilon}}^p$ to the reference strain rate $\dot{\varepsilon}^0$ (usually equal to 1.0), i.e.

$$\dot{\varepsilon}^* = \frac{\dot{\bar{\varepsilon}}^p}{\dot{\varepsilon}^0}. \tag{3.11}$$

In several studies, the influence of strain rate was studied and, as described by A. Manes et al [70], for strain rates lower than $1000\ s^{-1}$, this influence is not significant. Higher values of strain rates are observed mostly on ballistic tests and is not expected that, in a crash situation, the material suffers a strain rate higher than that value.

Also the temperature dependence is negligible in this case because the value of T^* will be small while the temperature of the specimen is close to room temperature and the room temperature is considerably lower than the melting temperature.

If the change in temperature and the strain rate are not considered, the model gets simplified by

$$\sigma = \left[A + B(\bar{\varepsilon}^p)^n\right]. \tag{3.12}$$

3.3 Relevant Tests

The structural study of a component or a full vehicle can be approached in a wide variety of methodologies and models. To have a good understanding of the structure behaviour in the studied situation, the choice of the simulation is critical to obtain meaningful results and conclusions about the expected behaviour of the structure in a specific test and save computation time traducing in cost savings. Essentially, the expected behaviour of the structure has to be studied before the computational model is developed.

The focus of this work is the study of a complete front bumper structure in terms of energy absorption and deformation. The computational model must represent a crash situation and provide data that allow to evaluate the performance of the structure and improve it. Taking this into account, the model must affect all the parts of the structure in a typical crash situation. The most common front crash test performed by the entities responsible for the assessment of vehicle safety systems is the full overlap test. In this work, a model of the bumper structure will be made and analysed in a full overlap impact against a rigid wall. The deformation pattern and range, as well as the energy absorption ability of the structure must be the focus of its development.

Trying to obtain a good proximity with NHTSA full overlap frontal crash test, shown in Figure 3.2, the model will be created and the structure will be developed to withstand an impact at 50 km/h and respect the requirements imposed by FMVSS.

Figure 3.2: NHTSA front crash test [71]

3.3.1 Static vs Dynamic Problems

There are two representative types of structural problems: static and dynamic problems. Static problems consist in an equilibrium structure where the sum of the forces and moments applied to the structure is zero. This is the type of approach used to study the behaviour of buildings or other structures that are not supposed to have large deformations.

When motion is added to a problem, the problem is no longer static and becomes dynamic, but in some cases quasi-static approach is used. Quasi-static means that there is motion in the problem but the displacement is done slowly and the inertia of the objects is less important than in high speed situations. When studying the compression or tension of a structure at slow speeds, the problem can be translated as a quasi-static problem. Some examples of static, quasi-static and dynamic problems are shown in Figure 3.3.

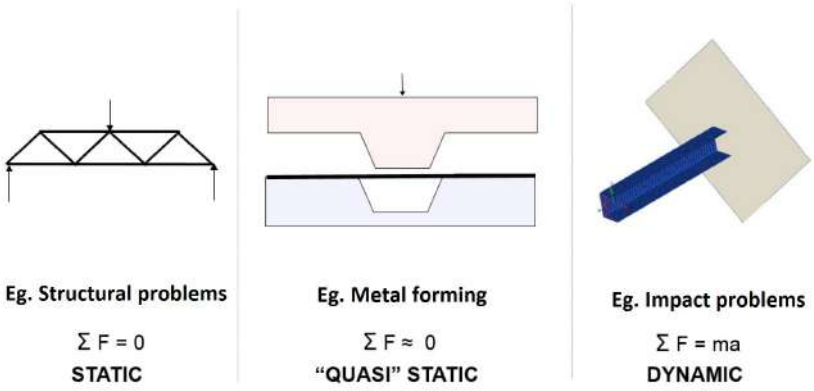

Figure 3.3: Examples of static, quasi static and dynamic problems (adapted from [72])

In terms of software, the term quasi-static simulation is used when a dynamic model program is used to produce a static result [72]. To have a result close to static, is important that the forces have a sufficiently large ramp up time so the force-time slope is not too steep. A dynamic code always produces oscillations in the result and the solution to reduce this is using a shallower ramping [72], as shown in

Figure 3.4.

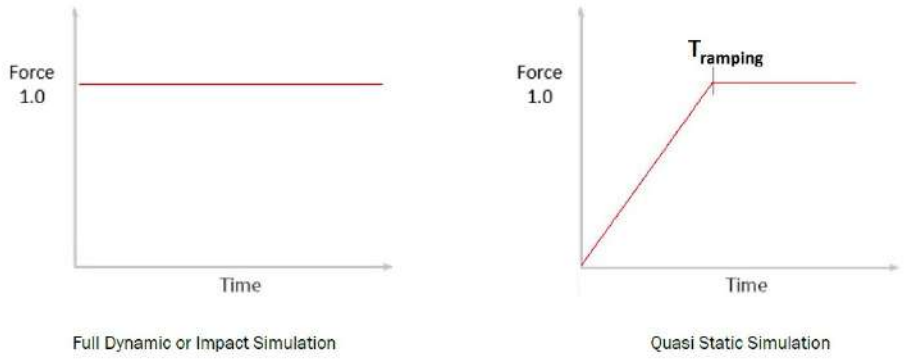

Figure 3.4: Comparison between quasi static and dynamic applied force [72]

In crash tests, static approach does not make sense because the velocity and inertia of the vehicle takes a big role in the behaviour of the whole structure, so the problem should be treated as fully dynamic.

Using a FEA, the basic equilibrium equations of transient dynamics can be written as

$$[M]\left\{\frac{d^2u}{dt^2}\right\} + C\left\{\frac{du}{dt}\right\} + K\{U\} = \{F_{ext}(t)\}, \tag{3.13}$$

where M is the mass matrix, C is the damping matrix and K is the stiffness matrix [72].

Solving a dynamic problem consists in solving this system for a discretized domain for given initial conditions, to obtain quantities such as displacements, velocities and accelerations with respect to time.

All other quantities can be derived from these and the most important are the element stresses, plastic strains, contact forces and the energies such as kinetic, potential energy and overall energy absorption characteristics popularly called as energy management [72].

3.3.2 Linear vs Non-Linear Behavior

After knowing that the problem should be treated as a dynamic problem, it is important to evaluate if the behaviour of the structure is expected to be linear or have non-linearities. Both static and dynamic problems can be treated as linear or non-linear.

Linear behaviour in structural problems means that the structure stress never surpasses the yield limit and it should only be used in small deflection problems, usually the criteria is that the deflection should not be larger than half of the structure thickness. Thus assuming a linear relation between stress and strain contacts usually have a non-linear behaviour, so using contacts in linear static analysis is also a bad approach [72].

Non-linear analysis allows the introduction of non-linearities in the problem that can be associated to materials, geometries or contacts. In studies with high plastic deformation or even when rupture is expected, for example crash tests, the material model is highly non-linear. Taking that into account, a model that allows the use of non-linearities will be used.

3.3.3 Implicit vs Explicit Analyses

In terms of computation, non-linear problems are solved with implicit or explicit solvers. A choice must be made taking into account that none of this type of solver is better for every problem. Both solvers can introduce and compute non-linearities but both have limitations. In Table 3.3 there are some criteria that can help choosing between implicit and explicit numerical models.

Table 3.3: Explicit and implicit choice criteria (adapted from [72])

Implicit Non-Linear Analysis	**Explicit Non-Linear Analysis**
Long Event (Few Seconds)	Short Events (milliseconds)
Small deformation	Large deformation
Less number of contacts	Complex and large number of contacts
Simple material models	Wide variety of material options

In a car crash, the total time of the impact can have less than 100 milliseconds, the deformation of the frontal impact absorption system should be large enough to absorb the kinetic energy and protect the cabin and the components suffer high deformations, sometimes even fractures. Taking the previous criteria into account, the obvious choice is to use an explicit software so that the computational model can have better resemblance to a real crash. Explicit analyses are the best option for dynamic high non-linear problems.

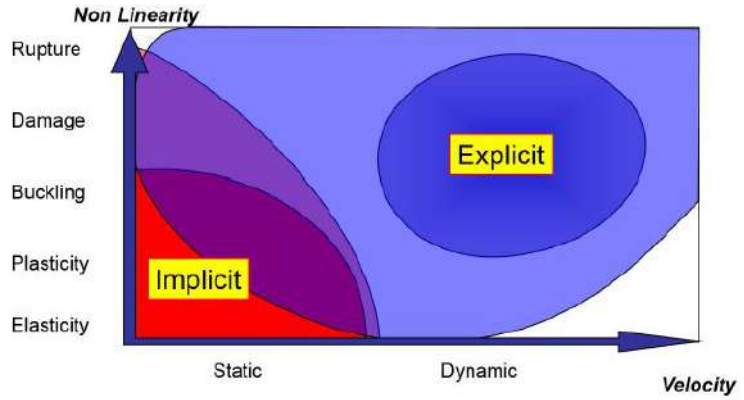

Figure 3.5: Range of application of implicit and explicit analysis [72]

In nonlinear implicit analysis, the solution at each step requires a series of iterations to establish equilibrium within a certain tolerance. In explicit analysis, no iteration is required as the nodal accelerations are solved directly.

Explicit analysis also allows local treatment. This is a major advantage when the user knows where the problem is. The problem can be analysed locally instead of changing the entire model.

In contrast to an explicit analysis, an implicit analysis also requires a numerical solver to invert the stiffness matrix once or even several times over the course of a load/time step. This matrix inversion is a

computationally expensive operation, especially for large models [73]. For this reason, a large memory space in the machine is a requirement for implicit analysis and not for explicit.

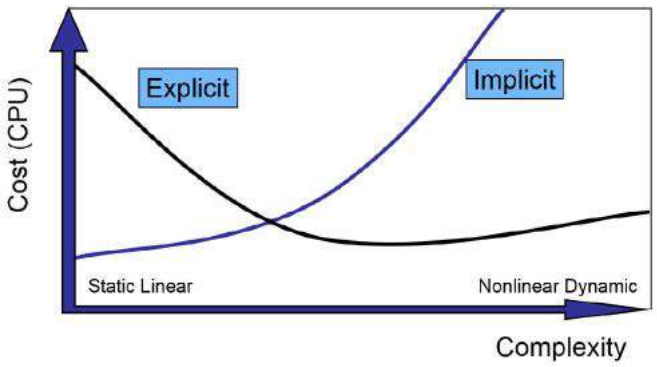

Figure 3.6: Cost vs complexity in implicit and explicit analysis [72]

The high robustness of explicit analysis is another advantage. Implicit analysis need the problem to be fully accurate to run, while explicit analysis can run even if the solution will not correspond to the aimed result. For this reason, the implicit result is usually accurate and always stable, while in explicit analysis a better understanding of the problem is needed to check if the results are correct.

Table 3.4: Advantages and disadvantages of implicit and explicit analysis (adapted from [72])

	Explicit	**Implicit**	
$(-)$	Conditional stability $\Delta t < \Delta t_c$	Always stable	$(+)$
$(-)$	Small $\Delta t[\mu s]$	Large $\Delta t[ms]$	$(+)$
$(+)$	Precision	Precision	$(+)$
$(+)$	$[M]^{-1}$	$([M] + a[K])^{-1}$	$(-)$
$(+)$	Low memory [10MW]	High memory [6000 MW]	$(-)$
$(+)$	Dynamic and Shock problems	Dynamic and Static problems	$(+)$
$(+)$	Element by Element $-$ Local treatment	Global $-$ Need of convergence at each step	$(-)$
$(+)$	High Robustness	Low Robustness	$(-)$
$(+)$	Relatively low cost $-$ Low CPU, Low Memory	Too expensive $-$ High CPU, High memory	$(-)$

As expected for a crash test, an explicit analysis was chosen to build the models in this work.

Explicit Method Time Integration

When solving dynamic problems with the FEA, it must be remembered that FEA is used only for the spatial discretization and the temporal (Time) discretization is always by using the Finite Difference Method (FDM). This approach is called as the Semi Discrete Galerkin as the space time finite element concept was a failure. The total response time is divided into much smaller time intervals Δt called time steps or increments. The equilibrium equations are solved and the value of unknowns are determined at (t + Δt) based on the knowledge of their values at time t [72].

In Figure 3.7, the flow chart of an explicit analysis is represented.

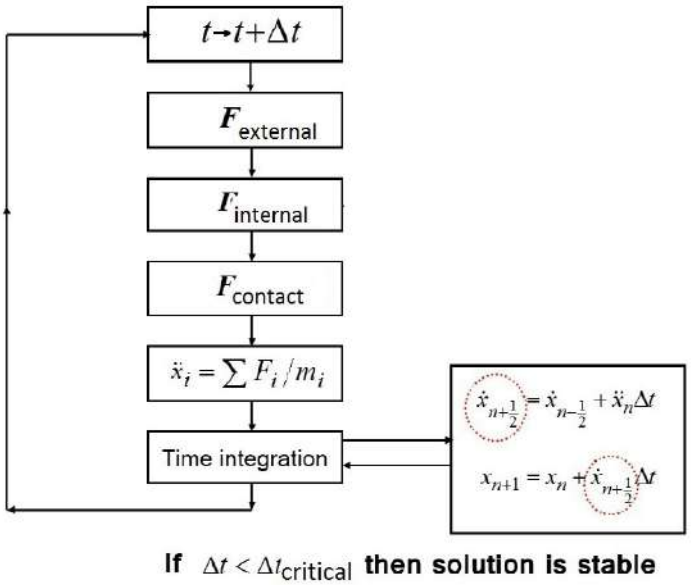

Figure 3.7: Explicit flow chart (adapted from [72])

A loop is made over all nodes with finite difference to obtain an acceleration for time n and with that, obtain the positions for $n+1$. The second Newton's law gives the acceleration,

$$\ddot{x}_n = \frac{f_{ext}(t_n) - f_{int}(t_n)}{m}, \tag{3.14}$$

then speed and position are integrated using a first-order finite-difference formula.

$$\dot{x}_{n+\frac{1}{2}} = \dot{x}_{n-\frac{1}{2}} + \ddot{x}_n \Delta t \tag{3.15}$$

$$x_{n+1} = x_n + \dot{x}_{n+\frac{1}{2}} \Delta t \tag{3.16}$$

After, a loop is made over elements to calculate strain,

$$\varepsilon_{n+1} = \frac{x_2^{n+1} - x_1^{n+1}}{l_0} - 1 \tag{3.17}$$

And using Hook's law, the stress can be obtained,

$$\sigma_{n+1} = E\varepsilon_{n+1} = E\left[\frac{x_2^{n+1} - x_1^{n+1}}{l_0} - 1\right] \tag{3.18}$$

Then the process starts again for $n+1$:

$$\ddot{x}_{n+1} = \frac{f_{ext}(t_{n+1}) - f_{int}(t_{n+1})}{m} \tag{3.19}$$

Time-step calculation and control

The explicit time discretization method requires a time step smaller than a critical value Δt_{cr}. If the time step is greater than the critical time step, the solution of the equations is artificially amplified during the step-by-step procedure, due to the accumulation of the discretization error [72].

If the system does not have damping, the critical time step can be simplified [72] as

$$\Delta t_{cr} = \frac{2}{\omega_{max}}, \tag{3.20}$$

where, w_{max} is the highest angular frequency in the system. For a discrete system, the time step must be small enough to excite all frequencies in the finite element mesh. This requires such a short time step that the shock wave does not miss any node when traveling the mesh [72],

$$\Delta t \leq \frac{l_{cr}}{c}, \tag{3.21}$$

where l_{cr} is the critical length of the element and c is the sound speed.

Elements, nodes and even other components like springs or contacts time step can be calculated and the global time step can be adjusted for a maximum value that makes the computation time as small as possible without compromising the results with error introduction. Elemental time-step is given by

$$\Delta t_e = \frac{l}{c} = \frac{l}{\sqrt{\frac{E}{\rho}}}, \tag{3.22}$$

where l is the length of the element, c is the speed of sound, E is the elasticity modulus and ρ is the specific weight. Nodal time-step is given by

$$\Delta t_n = \sqrt{\frac{2m}{k}}, \tag{3.23}$$

where m is the nodal mass and k is the equivalent nodal stiffness.

While discretizing the domain, the element size must be chosen carefully. If it is too large, the model will have low precision, but a low element size traduces in a low time step and a large computation time associated with the step and the number of elements to calculate.

As mentioned before, the most suitable computational method to represent the studied structure is a dynamic explicit analysis. However, to validate this model, the experimental data is more difficult to obtain. The perfect experimental test would be an impact of the bumper structure, implemented in the

vehicle, against a rigid wall, but that setup is not reachable in this early stage of the vehicle development.

The best option that can be considered is the validation of the material model, performing a tensile or compression test of a sample to obtain the characteristic stress-strain curve, and a quasi static test of an initial structure to validate the deformation pattern and the force vs displacement curve.

Adapting the quasi static FEA explicit model to a dynamic one, an approximation of what would happen in an impact test can be obtained and the structure can be sized to accomplish the project goals. This way it is possible to have an idea of the performance and crashworthiness of the studied structure when implemented in the full model subject to a full overlap frontal crash onto a rigid wall.

3.4 Crashworthiness Criteria

In order to assess the crashworthiness of the studied structure or compare the performance of different structures, it is necessary to establish proper criteria. These criteria must correlate the experimental or numerical results with the quality of the structures in several fields. The analyzed quantities must be relevant to the case study and previously proven useful in the comparison between crash structures.

In several structural studies, a group of parameters have been used numerous times [21, 12, 74] and proven to satisfy these requirements. Some of these quantities will be used in the present work, namely the Energy Absorption (EA), the Specific Energy Absorption (SEA), the peak crash force (F_{max}), the average crash force (F_{avg}) and the Crash Force Efficiency (CFE).

The energy absorption of the structure during a crash can be obtained as

$$EA = \int_0^{\delta} F(z)dz, \tag{3.24}$$

where $F(z)$ is the crash force and δ is the deformation. This structure, as well as the rest of the front structures of the vehicle, must be able to absorb the kinetic energy of the moving vehicle.

The ratio between the absorbed energy and the mass of the structure gives the SEA,

$$SEA = \frac{EA}{M}. \tag{3.25}$$

This parameter allows a better understanding of the absorption efficiency of the structure. The structure can be reinforced to improve the energy absorption but this represents a weight increase that can harm fuel efficiency.

During the crash, the maximum force point gives the peak crash force,

$$F_{max} = max(F_z). \tag{3.26}$$

A high force represents a high energy absorption but it is desirable that this occurs over long time periods to protect the passengers from high acceleration spikes.

When the EA is obtained, it is possible to divide it by the total displacement, yielding the average crash force,

$$F_{avg} = \frac{EA}{\delta}. \tag{3.27}$$

Maximizing this value is usually the best option. Maintaining a high force over the deformation time means that there is no high acceleration spikes.

Dividing the average crash force by the peak crash force, results in the CFE,

$$CFE = \frac{F_{avg}}{F_{max}}. \tag{3.28}$$

If the average crash force is maximized and the maximum crash force is minimized, CFE is close to 1. The best possible scenario is when a structure absorbs energy with a value close to 1 for CFE. In this case, the structure has a ramping in the beginning of the force-displacement curve, followed by a force value close to the maximum as shown in Figure 3.8. This leads to a uniform energy absorption over time and, consequently, high crash force efficiency. A structure with a better CFE minimizes the force spikes in the crash, leading to less accelerations in the cabin and a better safety.

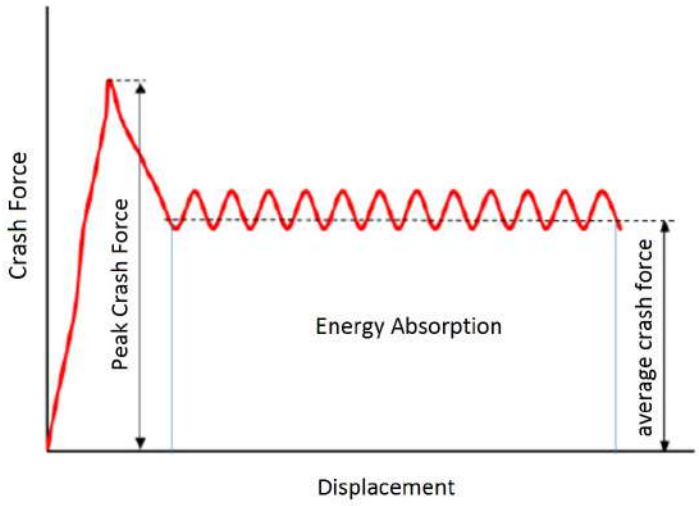

Figure 3.8: Force vs displacement diagram (adapted from [75])

Chapter 4

Quasi-Static Approach

As mentioned in Section 3.3, due to the unfeasibility of dynamic crash experimental tests, the best option with the available means to validate the model is to perform a quasi-static analysis and correspondent experimental procedure.

For the bumper structure, the quasi-static test that better matches the front crash situation with a full overlap is the compression of the structure between two rigid bodies in the direction correspondent to the velocity of the vehicle. If the behaviour of the structure is close to the numerical model in terms of deformation and energy absorption, the quasi-static model is validated and a similarity is expected between the dynamic crash model and a real crash.

4.1 FEA Model

For the computational simulations performed in this work, a generic process was used with the numerical tools available at CEiiA. Figure 4.1 sums the process in a flowchart.

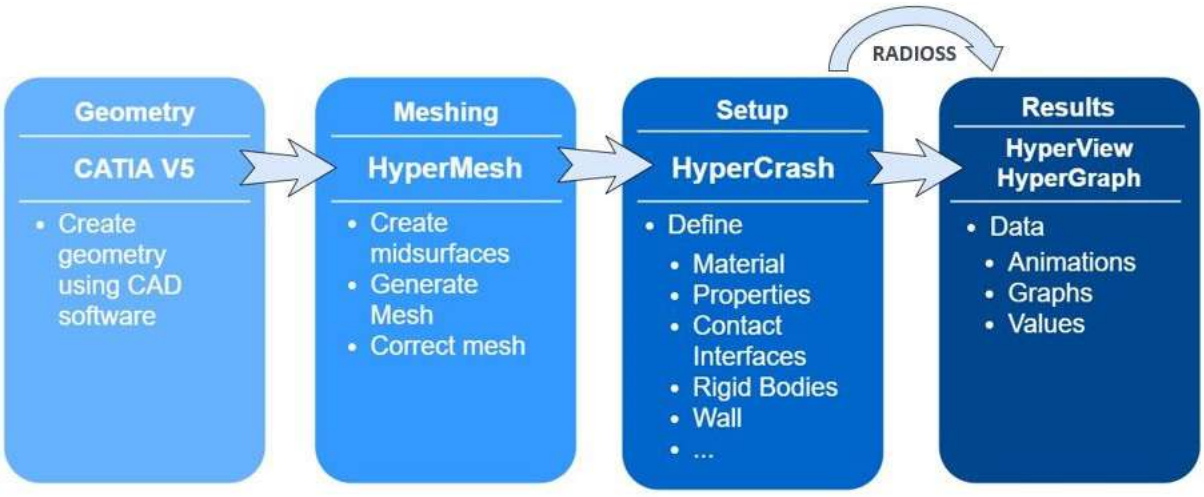

Figure 4.1: Flowchart of the process used to build the numerical model

The first step is to create a 3D CAD model. The commercial software used was *CATIA*^{TM} *V5*. In this

part of the work is important to establish all the dimensions of the parts.

After the CAD geometry is created, it is necessary to discretize the domain to allow the calculation software to use this nodes. For this job, *Altair® HyperMesh®* was used. The software can generate a mesh automatically but is possible for the user to check the quality of the generated mesh and edit it to satisfy the needed criteria.

When a good quality mesh is obtained, it is necessary to perform the test setup. This setup can be done in *HyperMesh®* but Altair has another pre-processing software that is more indicated for crash analysis. The software is called *HyperCrash™* and allow the user to setup different materials, properties, connections between materials, velocities, forces and other relevant parameters to obtain the best resemblance of the simulation to the real crash test.

The last steps are to run the calculations and post-process the results. For the calculations, *RADIOSS™* was used. *RADIOSS™* is a solver software capable of performing explicit as well as implicit non-linear analysis. The analysis setup file is the input and the outputs are a series of files that have all the information about the crash test simulation. The results are analyzed in *HyperView®* and *HyperGraph®*. *HyperView®* let the user see an animation of the test and observe any major problems with the structure. *HyperGraph®* compiles the relevant information in graphs and allows a treatment of the output data, defined in the crash setup phase.

It is important to point out that this problem could be treated as a symmetrical problem. Using only half of the structure and imposing symmetry boundary conditions could have a close result in this case and save a substantial amount of computation time. However, this model will be used to simulate the bumper structure of the vehicle in a future stage of the project. At that stage it is possible that the structure becomes non symmetrical so that simplification will not be a part of the current approach. The major steps of the process outlined in Figure 4.1 are described in the following subsections.

4.1.1 Geometry

In a latter stage of this work, a geometry improvement study will be performed in order to obtain a structure that is expected to have a good performance in a frontal crash test performed by responsible entities. Before that work can be done, an example geometry must be created to validate the model.

For the creation of the CAD model, *CATIA™ V5* was used. *CATIA™ V5* is a commercial software that allows the user to create geometries with high level of complexity and detail.

As explained in Section 2.3, the main components of a standard bumper are a transverse beam and the frame rail. In this work, the deformable structures will be properly sized. The general measurements used to build this structure where obtained from a preliminary model of the vehicle being developed by CEiiA. The distance between the crash boxes is 640mm and the length of the front beam is 1125mm. From a study made by G. Belingrady, et al. [58], it was concluded that a curvature in the transverse beam is beneficial for the crashworthiness of a bumper structure. At this point of the project, a radius of 3200mm, that was concluded more beneficial in that study, was used.

Due to the early stage of the vehicle project, the remaining dimensions have some design freedom

and will be studied in Chapter 6 for the optimization of the structure crashworthiness. For the quasi-static model, the dimensions shown in Figure 4.2 were used.

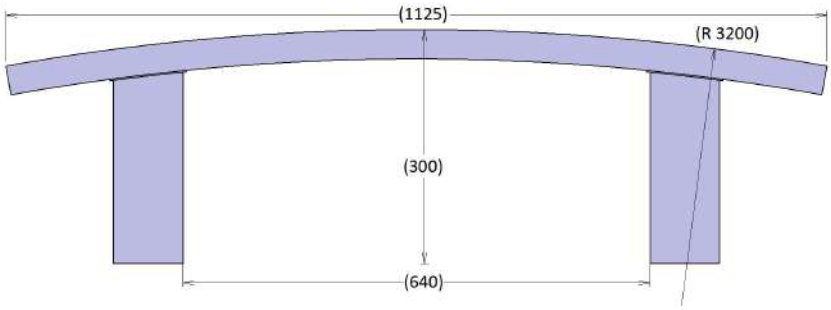

Figure 4.2: Bumper geometry measurements

In order to simplify the assembly of the structure for the experimental tests, as well as minimizing the manufacturing cost, the part sections were chosen from a catalogue of standard extrusion profiles [76].

The chosen section for the crash boxes was a square one, with the largest cross section area as it is expected that this part of the structure will absorb more energy in a front impact crash. For the transverse beam, a rectangular shape was used where the largest side should be at least the same size as the crash box to simplify the bonding process between the two parts. From the sections that have this side larger than the crash box sides, the one with higher thickness was chosen.

The cross section of the boxes and transverse beam are represented in Figures 4.3 and 4.4.

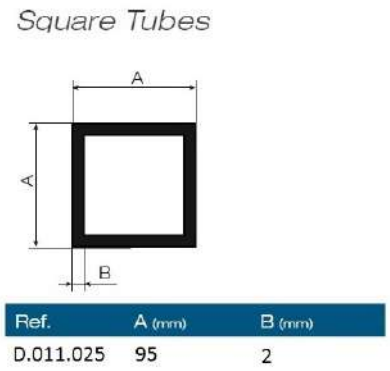

Figure 4.3: Crash box cross section (adapted from [76])

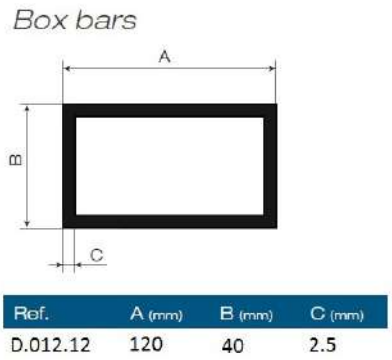

Figure 4.4: Transverse beam cross section (adapted from [76])

The complete structure composed by two crash boxes and the transverse beam is represented in Figure 4.5. The mass of the structure can be obtained in *CATIA*^{TM} *V5* as soon as the CAD part is finished by specifying the material density.

4.1.2 Meshing

To be able to use FEA, the domain should be discretized by applying a mesh to the geometry. For thin walled structures, each of the parts faces have a small thickness when compared to the general dimensions of the bumper. This makes a good approximation to simplify the formulation using the tubes

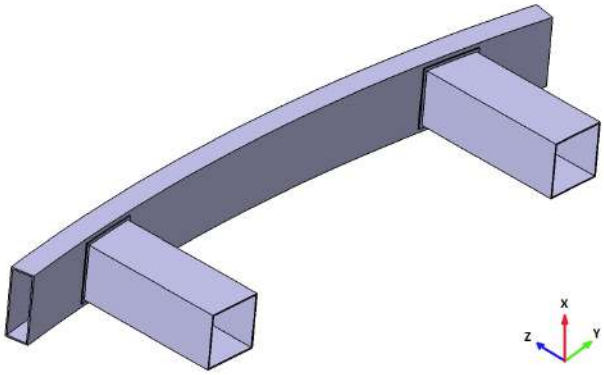

Figure 4.5: Complete bumper structure

as surfaces, adding thickness later on, in the setup phase. 2D shell elements represent a saving in computational time when compared to solid elements.

After all the parts are created, a $.igs$ file can be exported from *CATIA™ V5* to be used in *HyperMesh®* to create the mesh. The first step is to import the geometry for *HyperMesh®* and create a surface that represents the structure. The technique used is to create a midsurface and generate the mesh in that surface. A midsurface is a surface component that is generated in the center plane of each surface. This allows to treat the problem with 2D mesh elements and input the corresponding thickness later in the setup software. 2D shell elements make the analysis much more cost efficient, when compared to 3D elements, decreasing the computational time. This is only possible because none of the sections in the used geometry have variable thickness. When the midsurface is created, the next step is to generate a mesh. The different midsurfaces can be grouped with collectors as parts of the structure as shown in Figure 4.6.

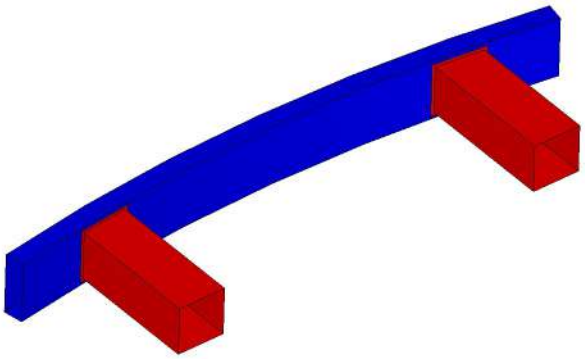

Figure 4.6: Structure midsurfaces

With the structure converted into surfaces, *HyperMesh®* can generate an automatic mesh to divide the domain in elements. Generating a mixed mesh, the software will try to divide the surface into quads and triangles that are as close as possible to the chosen element size. The element size should be small enough for the model to have a good detail but not too small because that will influence the number of elements to be calculated and the time-step of the explicit analysis. A small variation in the element size

represent a large change in in the computation time. In the present work, all generated meshes were generated for a target element size of 5 mm, following the minimum recommended value by the software manual for crash analysis [72]. The minimum value is used in order to keep the detail of the deformed structure. It is expected that several bends are formed during the axial crushing of the structure and the detail of this deformation pattern will be influenced by the size of the elements. A study was made to investigate if using a smaller element size would improve the quality of the results. The force vs displacement curve of both models, one with a target element size of 5 mm and other with a target element size of 2.5 mm, is shown in Figure 4.7.

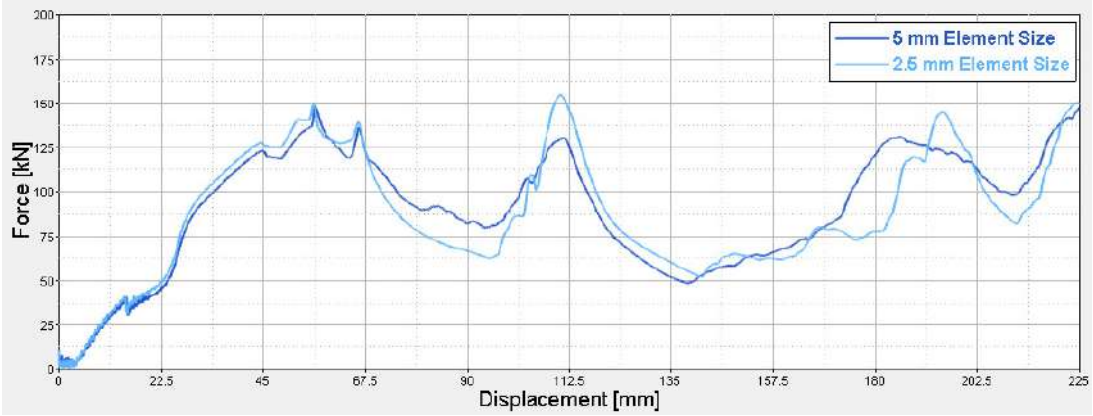

Figure 4.7: Comparison between the model results with a 5 mm element size and a 2.5 mm element size

The two meshes generate a result with similar force-displacement curves, the values of energy absorption are also similar with only 2.7% difference. This values are listed in Table 4.1.

Table 4.1: 5 mm element size vs 2.5 mm element size energy absorption

Target Element Size [mm]	**Energy Absorption [J]**	$\Delta EA\%$
5	19780	–
2.5	20306	+2.7

The computational time of the 5 mm element size mesh analysis was close to 16 hour, while the more refined mesh took close to 62 hours. Both element size and time step have influence in this time.

The 5 mm element size mesh has 22515 elements while the 2.5 mm element size mesh has 87282. This is close to four times the number of elements. Considering the similarity of the results and the difference in computational cost, the target element size for all the analysis of this work will be 5 mm.

For a good quality mesh, the number of triangles should be minimized. In a simple structure like this, all triangles can be removed to improve the mesh quality. In Figures 4.8 and 4.9 an example of this improvement is shown.

Then the mesh can be checked for quality parameters and corrections can be made to the elements that violate the quality standards. When a good quality mesh is obtained, the solver deck can be exported in a $.rad$ file that will serve as base for the model setup.

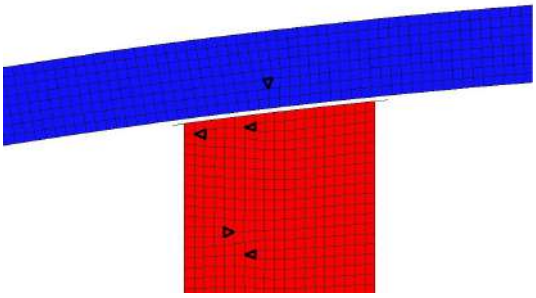

Figure 4.8: Mesh with triangles

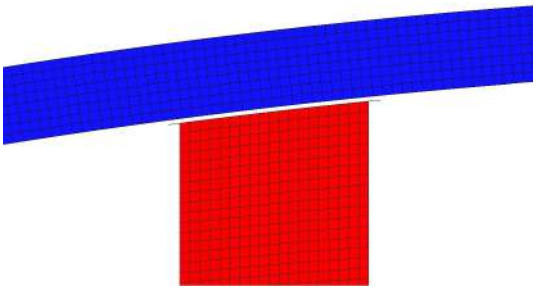

Figure 4.9: Corrected mesh

4.1.3 Setup

Being a quasi-static model, trying to represent a real compression test, the velocity of the compression should be in the order of 1 mm/s. For this order of speed and taking into account that the time step should be small enough to obtain convergence, the compression would take close to 5 minutes. This is not a workable time range for an explicit model.

An alternative would be the creation of an implicit model for the quasi-static test and an explicit model for the dynamic one. One of the problems with this approach is that the quasi-static model would still have a high plastic deformation that can be be a problem using an implicit integration. Also, the similarity of the tests and correspondence is larger if the same software is used, maintaining the same material model, assigned properties and mathematical formulation. For this reason, it was decided to use the same explicit solver for dynamic and quasi-static models, making quasi-static one with a higher compression velocity of 500 mm/s. This choice allows to have the same time-step in dynamic and quasi-static analyses, as well as a similar setup without compromising the results in a significant level or increasing the computation time for impracticable values.

Using the previously created mesh, the crash setup must then be created. This setup must represent the bumper crash behaviour when connected to a vehicle and impacting a rigid wall.

Material

As explained in Section 3.1, the material used in the present study is an Aluminum 6061 alloy with a T6 heat treatment. According to *Aerospace Specification Metals Inc.* [77], citing several books [78, 79], this material has the relevant properties presented in Table 4.2.

Table 4.2: Aluminum 6061 T6 properties

	Property	**Value**
ρ	Density $[kg/m^3]$	2700
E	Young's modulus $[GPa]$	68.9
ν	Poisson's ratio	0.33
σ_{yield}	Plasticity yield stress $[MPa]$	276

HyperCrash^{TM} has a wide range of material model formulations from perfectly elastic, to plastic and fluid materials. One of the formulations available in this software is the one explained in Section 3.2, the Johnson Cook material model. With this formulation, using the properties described in Table 4.2, the material model was created and assigned to both parts of the structure.

Properties

At this point, the parts are still surfaces instead of solids. *HyperCrash*^{TM} allow the introduction of properties for lines, surfaces or volumes. With these definitions, it is possible to use a line as a beam or a spring and to add layers or thickness to a surface for example. In this case, a thickness of 6mm was added to every surface using the $SHELL$ command.This command instructs the software to treat each element as a 2D finite element.

Contact Interfaces

The contact definition in *HyperCrash*^{TM} is usually computed with a master surface and slave nodes. $Type$ 7 contact interface allow the presence of slave nodes in the master surface. This allows the creation of a contact called $selfimpact$. Selecting all the parts as master surfaces and all the nodes in the surfaces as slave nodes, makes the contact possible between different sections of a surface with itself as well as with other parts. The contact happens when the nodes and surface are closer to each other than a specified gap value, so the thickness should be taken into account when defining this minimum gap. Having the same thickness in every surface in the current design, a single self impact $Type$ 7 contact is enough for the current model.

If the contact is not correctly defined, penetrations between different elements can occur. It is critical to avoid or correct these penetrations to have a stable model. For the contact stiffness, different formulations can be used. In this case, the stiffness was computed as an average between the stiffness of the master and slave elements $K = (Km + Ks)/2$. The $Type$ 7 contact interface also allows the friction definition. Coulomb friction formulation was used for this contact.

Rigid Bodies

In order to impose a velocity to the rear end of the bumper or, in the case of the dynamic test, add mass or inertia to the structure, rigid bodies can be created. Rigid bodies are created with a command called $RBODY$. With this command it is possible to create a master node in the center of mass of a group of slave nodes. This command locks the distance between the nodes in this group and the created master node. A used practice in the study of bumper structures is to create a single rigid body with the nodes at the back end of both of the crash boxes [58]. The problem with this method is that it creates a pinpoint at the center of this plane. If no boundary conditions are added to this node, in the case of any unstable behaviour in a crash, it will rotate in the Z axis. To minimize this problem, two rigid bodies were created. Each rigid body was created in the center of gravity of the nodes in the end plane of the crash boxes as shown in Figure4.10.

Wall

Another useful feature in *HyperCrash*^{TM} is the creation of rigid walls. Rigid walls are non deformable surfaces that can have the shape of cylinders, spheres, parallelograms or infinite planes. In this case, an infinite plane was created near the front end of the bumper structure. The contact between the structure and the wall can be created in the wall definition as well as the friction definition. This surface is considered as a master surface and slave nodes are chosen in the structure so the contact occurs between the bumper and the wall. In Figure 4.11 the wall is represented with a square shape in purple and the slave nodes in green. All the nodes from the front beam were picked as slave nodes.

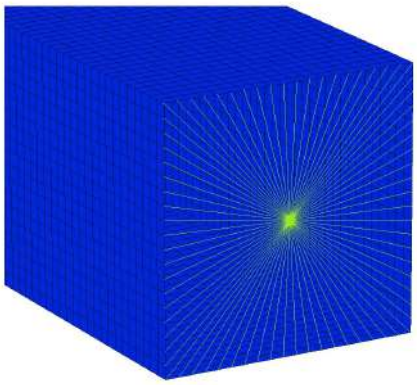

Figure 4.10: Rigid body

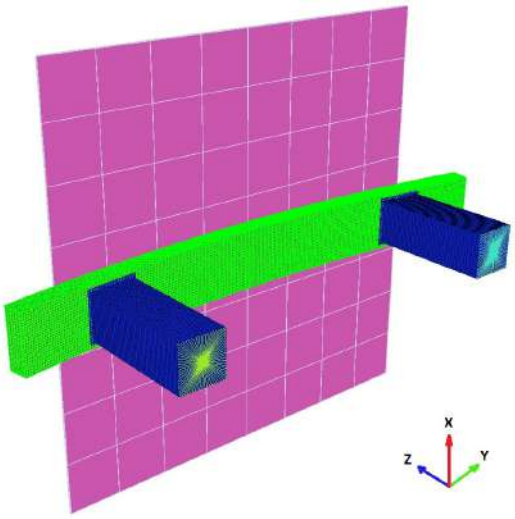

Figure 4.11: Infinite wall

Imposed Velocity

For the quasi-static model, in order to mimic the experimental compression test, the structure must be compressed between two rigid structures. In this case, one of these structures will be the rigid wall and the other will be defined with two rigid bodies, one on the end of each crash box. These bodies will have a constant imposed velocity of 500 mm/s, as explained in the beginning of this section. The rigid body velocity means that all the nodes that define the rigid body will have the same imposed velocity. The result is a movement of the nodes in the end plane of the crash boxes, similar to the movement of a wall compressing the structure against the rigid wall. This compression displacement will have a velocity aligned with the Z axis and it's represented with a green arrow in Figure 4.12.

Boundary Conditions

To maintain the horizontal positioning of the structure, one boundary condition was added to each rigid body. A boundary condition is a tool that allows to "lock" one or more movement degrees of freedom (red arrows in Figure 4.12). In this case for the rigid bodies, the movement in X, Y directions and all the rotation degrees of freedom where locked so the end of the bumper maintains the same position during

the whole compression test, having the rigid bodies to move only in the Z direction with the imposed velocity explained before (green arrow in Figure 4.12).

Connections

In terms of connections, the crash boxes were connected to the transverse beam by spotweld. Spotweld is a type of connection in *HyperCrash*^{TM} that allow the connection of two parts. In this case, the two parts were selected and three spotwelds were created on each side of each of the crash boxes as shown in Figure 4.13. An element is selected in the crash box and the software searches for a projection of the center point of the element in the other part. A spring element is created between the two points. By default, this spring is rigid. The connections are not the focus of this work so the spring formulation was not changed to not influence the result of the crash model.

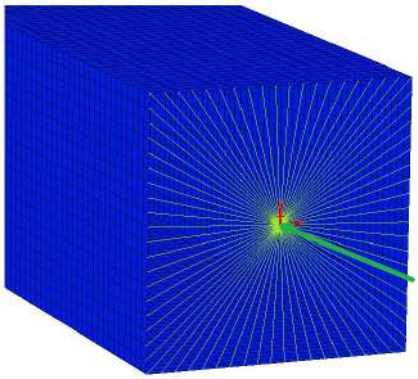

Figure 4.12: Boundary conditions and velocity

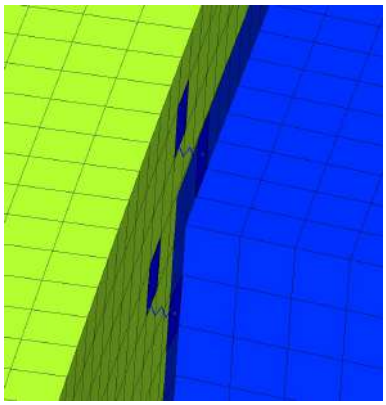

Figure 4.13: Spotweld connection

Control Cards

The final step on the model setup is to give the instructions to the solver about how it should perform the analysis. For *RADIOSS*^{TM} , this instructions are given with $Control\ Cards$. These cards have information about the solving process and writing of the results.

All the required or desired results should be asked in this phase. *HyperCrash*^{TM} allows the definition of animation data to preview the values correspondent to each element in the output format. General data such as stress, strain, energy, velocity or displacement can be seen in the pre-processing tool if specified in this phase. If any more detailed data is needed, the software has an option called $Time\ History$ that allows the user to ask for a more specific set of data about a specific element, node part or section. The writing frequency of this data can also be controlled.

For an explicit analysis, the time of the compression must be carefully chosen. In explicit solvers, the solving process is based on the time-step. This means that a big change in the compression time can make the solving time a lot longer. In the case of the quasi-static test, the approximate compression

distance is known and with the definition of the imposed velocity, the compression time can be obtained and provided to the solver with the command RUN.

There are several cards responsible for the definition and control of the time-step. Using the process described in Section 3.3.3, and defining a minimum allowable element size for the mesh, the minimum time-step was calculated. A criterin was defined for a minimum allowable element size of 3.5 mm and every mesh generated in this work will be checked in order to respect the critical time-step calculated here.

Using equation (3.21), for a critical size of $3.5\ mm$, a Young's modulus of $68.9\ GPa$ and a density of $2.7 \times 10^{-6}\ kg/mm^3$, the critical time-step is $\Delta t_c = 6.93 \times 10^{-4}$. A maximum time-step of 1×10^{-4} was defined to make sure that none of the other parameters of this model produce a divergence in the solution. Using a CST formulation, a scale factor of 0.9 was used for the time-step with a cap in 1×10^{-5}. Using this method, if at any moment of the solving process a higher frequency is necessary, mass is added to the node and the time-step is reduced.

With all the needed parameters and specifications completed, the model can be exported in a $.rad$ file format and imported in *RADIOSS™* to be solved. After the first solution, it was verified that the time-step did not change, which means that this factor was never applied and the initially defined time-step was maintained during all the solving process as expected.

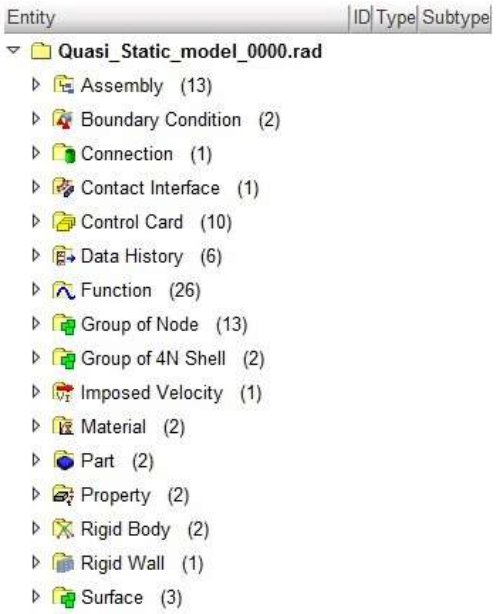

Figure 4.14: *HyperCrash™* model tree

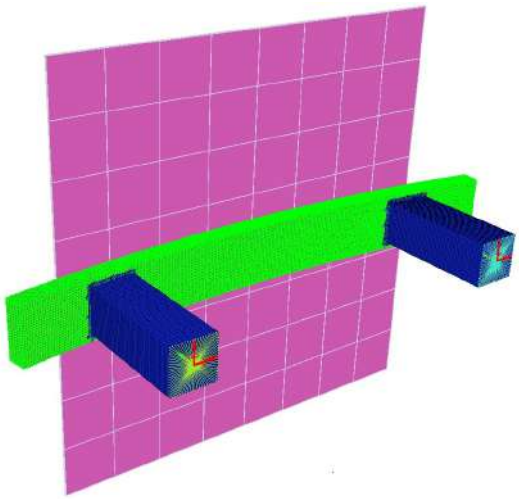

Figure 4.15: Complete model

4.1.4 Results

To analyze the results of the test, a representative animation of the compression test is opened in *HyperView®* (Figure 4.16). This animation allows an initial check of the deformation sequence as well as some variables with color schemes.

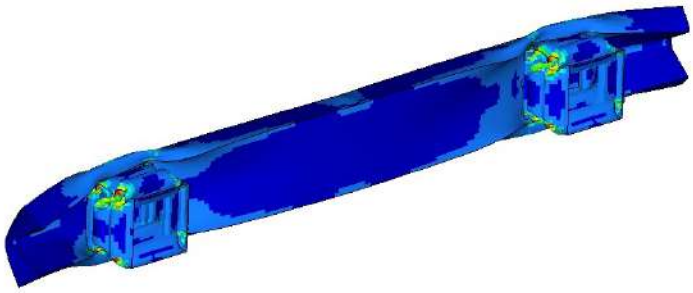

Figure 4.16: Deformed structure with plastic strain colored elements

After that, *HyperGraph®* is used to analyse the numerical data provided by the solver.

The peak crash force (F_{max}) is obtained from the force-displacement curve shown in Figure 4.17.

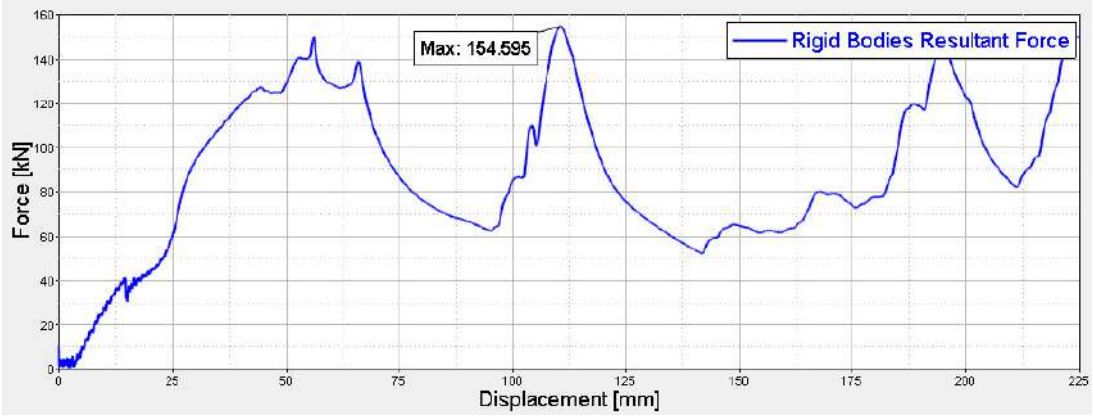

Figure 4.17: Quasi-static test force-displacement curve

Integrating this curve, is possible to obtain the Energy Absorption (EA) and divide that value by the displacement (δ) to obtain the average crash force (F_{avg}) as explained in Section 3.4.

With the mass of the structure and these two values, the crashworthiness criteria SEA and CFE can be calculated for the considered displacement.

This values are calculated for a displacement of 225 mm. This value corresponds to the value where a maximum deformation is observed in the structure. After this value, the structure is not able to deform and the force starts to increase at a high rate so it is considered that this value as the maximum reasonable deformation range.

The summary of the crash performance of the modeled baseline structure described in this section is summarized in Table 4.3.

Table 4.3: Quasi-static model data

	Data	**Value**
F_{max}	Peak Crash Force [kN]	154.6
F_{avg}	Average Crash Force [kN]	87.9
EA	Energy Absorption [J]	19780
M	Mass [kg]	3.421
δ	Displacement [mm]	225
SEA	Specific Energy Absorption [J/kg]	5782
CFE	Crash Force Efficiency	0.57

The value of CFE in this range of deformation is 0.57, this means that the maximum force is 1.75 times the average force what is a reasonable value. Remembering that CFE is the ratio between the maximum and the average force, the fact that all the three peaks in force have almost the same value and the force never goes below 50 kN helps to have a good value for this criterion.

In terms of energy absorption it is not possible to know if the obtained value is high enough before some parameters are chosen. In Chapter 6, the values for the impact test will be defined and will be possible to conclude if this structure is able to absorb all the necessary energy and with a reasonable force distribution.

The goal of this work is to improve this structure using these criteria as a comparison measure. That will be studied and discussed in Chapter 7.

Chapter 5

Validation Procedures

5.1 Material Model Validation

To make sure that the current used material model corresponds to the behaviour of the real material, it is necessary to validate this model. With a sample of the studied materials it is possible to perform a tension test to obtain the stress-strain curve. If the curve is similar to the curve used in the computational material model, the behaviour in the experimental tests should be close to the one in the computational simulations.

Several extruded aluminum companies and suppliers were contacted in order to obtain extruded aluminum profiles as close as possible to the ones chosen in the previous chapters. At the time of this work, the chosen alloy was not available from any of the suppliers. The closest option in terms of properties and the one used for this validation procedures was the aluminum 6063 alloy with T6 heat treatment. This was the only available option and it would be important to perform the tests with a material that correspond to the desired alloy properties to validate the models used in this work.

5.1.1 Experimental Procedure

The tensile test was performed according to the standard ASTM B557M-15 - Standard Test Method for Tension Testing (Metric) [80].

Test samples

In order to have the best possible proximity to the material used in bumper structure analyses, the samples were cut from the same aluminum 6063-T6 extrusion tubes that will be used to build the complete structure. 15 samples were cut having the same axial direction, corresponding to the direction of the extrusion process. This cut and measurements of the samples are represented in Figures 5.1 and 5.2.

Each of the samples was measured before testing. Three values of width W and thickness t were collected in the points represented in Figure 5.3 and the average of these three values was introduced in the software so the area can be taken into account and tension values can be calculated.

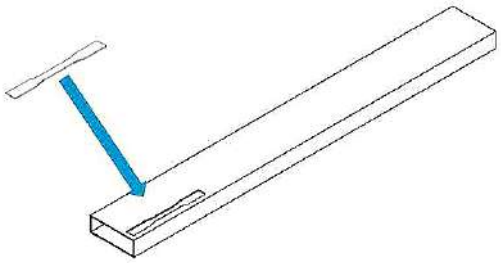

Figure 5.1: Samples cut from the extrusion tubes

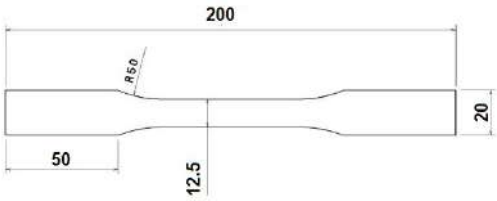

Figure 5.2: Sample measurements

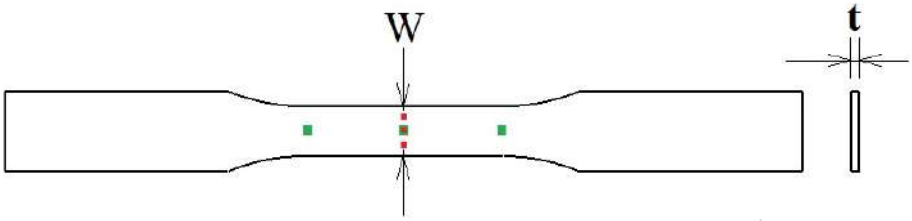

Figure 5.3: Width (green) and thickness (red) measurement points

Samples that have a difference in width or thickness larger than 1% between one of the sides and the center will not be considered in order to have a group of samples with a section as uniform as possible.

In Table 5.1 all the measured values are listed and samples 1, 4, 5, 8 and 10 were excluded. Sample 7 was also not considered due to visible damage from the cutting process and sample 15 was used as preliminary and calibration sample so will not be considered also.

Table 5.1: Sample measurements

	Width	**[mm]**			**Thickness**	**[mm]**		
Specimen	W**1**	W**2**	W**3**	**Average** W	t**1**	t**2**	t**3**	**Average** t
1	12.30	12.25	12.17	12.24	1.946	1.970	1.974	1.963
2	12.54	12.51	12.53	12.53	2.029	2.025	2.020	2.025
3	12.45	12.47	12.40	12.44	2.038	2.029	2.024	2.030
4	12.47	12.11	12.22	12.27	1.973	1.982	1.991	1.982
5	12.32	12.30	12.41	12.34	1.556	1.767	1.759	1.694
6	12.56	12.62	12.63	12.60	2.059	2.059	2.074	2.064
7	12.27	12.33	12.43	12.34	2.002	2.013	2.023	2.13
8	12.41	12.37	12.57	12.45	2.005	1.998	1.999	2.000
9	12.45	12.41	12.48	12.45	2.033	2.027	2.024	2.028
10	12.32	12.24	12.39	12.32	2.044	2.032	2.030	2.035
11	12.30	12.33	12.40	12.34	2.035	2.035	2.031	2.034
12	12.47	12.43	12.49	12.46	2.033	2.034	2.040	2.036
13	12.37	12.37	12.31	12.35	2.033	2.030	2.029	2.031
14	12.52	12.47	12.52	12.50	2.026	2.034	2.019	2.026

Tensile procedure

For this procedure, a servo-hydraulic MTS test machine with a 50 kN load cell (SN 429175) was used. The test velocity was 1 mm/min, being the initial distance between the two grips 150 mm. All tests were performed at the same temperature, of 24℃.

A biaxial extensometer, model 632.85F-05 was used to measure the extension in the axial direction and the decrease in width of the samples. The gauge length of the extensometer is 25mm in both directions. The complete setup of the procedure is shown in Figure 5.4.

Figure 5.4: Tensile test setup

The average measurements in Table 5.1 were introduced in the test machine for each of the samples being tested.

5.1.2 Experimental Results

After each of the samples is tested until fracture, a photo of the fractured sample is taken and the machine output is collected.

The output consists of the stress-strain curve of each sample as well as values for axial and transverse elongation. From the curve, the values of elasticity modulus, yield strength, ultimate strength and elongation at break are obtained. Poisson's ratio is obtained from the axial and transverse elongation.

The output data was collected and compiled in the graph shown in Figure 5.5.

From Figure 5.5, it is clear that most samples have similar behaviour in the tensile procedure, except samples 13 and 14. For this reason, these two samples were not considered.

Values for Young's modulus (E), Poisson's ratio (ν), elongation at break and plasticity yield stress or yield strength (σ_{yield}) were collected from the rest of the samples, averaged and used as an input in the computational model. These values are listed in Table 5.2.

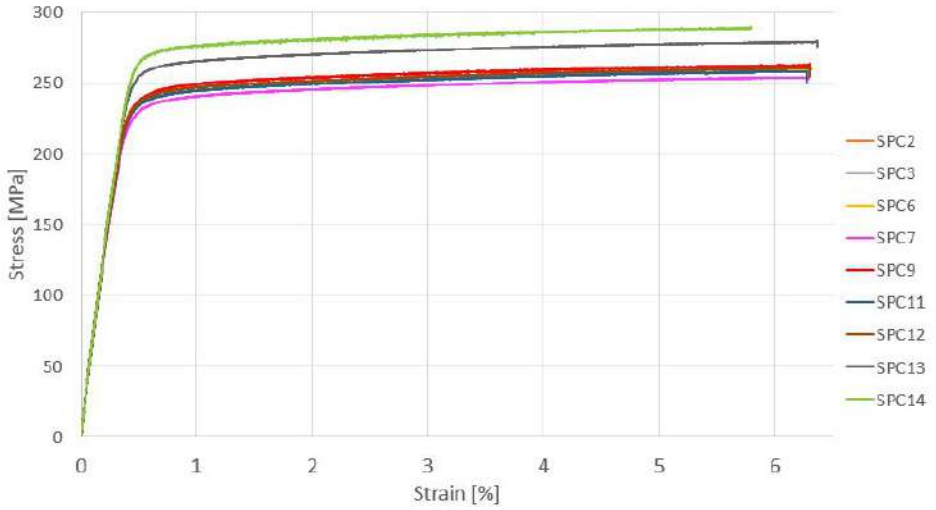

Figure 5.5: Tensile tests output curves

Table 5.2: Results average

Specimen	E [GPa]	Yield strength [MPa]	Poisson's ratio	Elongation at break [%]
2	62.28	212.55	0.38	6.31
3	62.18	219.23	0.38	6.28
6	61.67	215.80	0.38	6.29
7	60.43	212.32	0.36	6.30
9	62.15	218.72	0.37	6.30
11	61.54	218.99	0.38	5.39
12	61.61	212.16	0.36	6.30
Average	61.69	215.68	0.373	6.17

According to *Aerospace Specification Metals Inc.* [77], citing several books [78, 79], this material has the properties presented in Table 5.3.

Table 5.3: Aluminum 6063 T6 properties

	Property	Value	Units
ρ	Density	2700	kg/m^3
E	Young's modulus	68.9	GPa
ν	Poisson's ratio	0.33	
σ_{yield}	Plasticity yield stress	214	MPa
ε_{max}	Elongation at break	15	%

Comparing these values with the averaged values obtained in the tensile procedures, both the Young's modulus (E) and ν are around 12% higher than expected, while the value for the yield strength has less than 1% difference. The largest difference occurs in the value of elongation at break that is 2.5 times lower than expected. This is an indicator that the material is a lot more brittle than expected.

5.1.3 Material Model Curve Fitting

As described in Section 3.2, the material model used in this work is the Johnson Cook material model. The value A from equation (3.12) is the yield strength that was obtained from the tensile procedures.

A ”fit” of the parameters B and n was made using Microsoft Excel solver funcionalities, minimizing the distance of each point to the average of the curves obtained from the tensile procedures. The optimum values for parameters B and n were obtained and the resulting curve is shown in Figure 5.6.

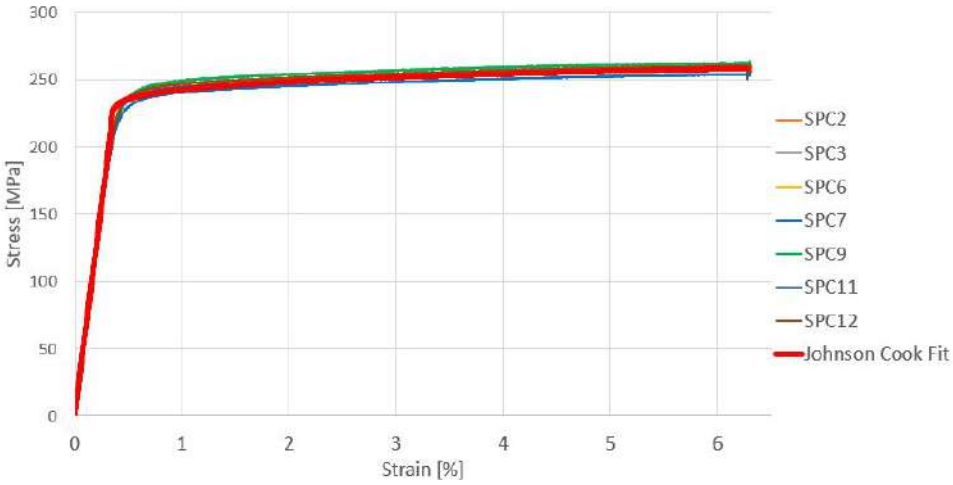

Figure 5.6: Johnson Cook material model curve compared with tensile test results

5.2 Quasi-Static Model Validation

In order to see if the results obtained in Chapter 4 have a good similarity to a real compression and validate the quasi-static model, that had a good correlation with the dynamic model as shown in Chapter 6, an example bumper compression procedure was performed using the resources available in CEiiA headquarters. A servo-hydraulic MTS test machine with a 250 kN load cell (SN 10317357) was used in this experimental procedure.

As mentioned in Section 5.1, the available alternative to perform the validation procedures were 6063-T6 aluminum alloy tubes. The section of the tubes was also not possible to be the same of the one used in the quasi-static model. The measurements of the used geometry in the compression procedure are represented in Figure 5.7. The transverse beam could not be bent, so a straight beam was used.

This experimental procedure will be repeated for three identical structures to minimize uncertainties in the measured values.

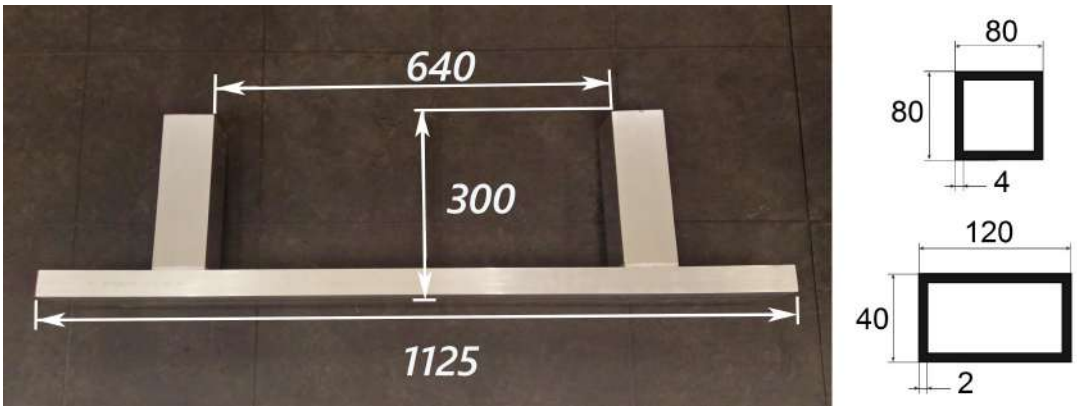

Figure 5.7: Compression procedure specimen measurements

5.2.1 Quasi-Static Numerical Model Changes

Having changed the geometry, the quasi-static model was adapted to correspond to the used specimen. The setup remained the same as the setup explained in Chapter 4 but the material properties were modified to correspond to the material model fitting described in the Section 5.1. Performing this simulation before the experimental procedure allows a rough prediction of the force-displacement distribution. The expected force should not exceed 250 kN to be within the test machine limits.

The force-displacement curve obtained is shown in Figure 5.8.

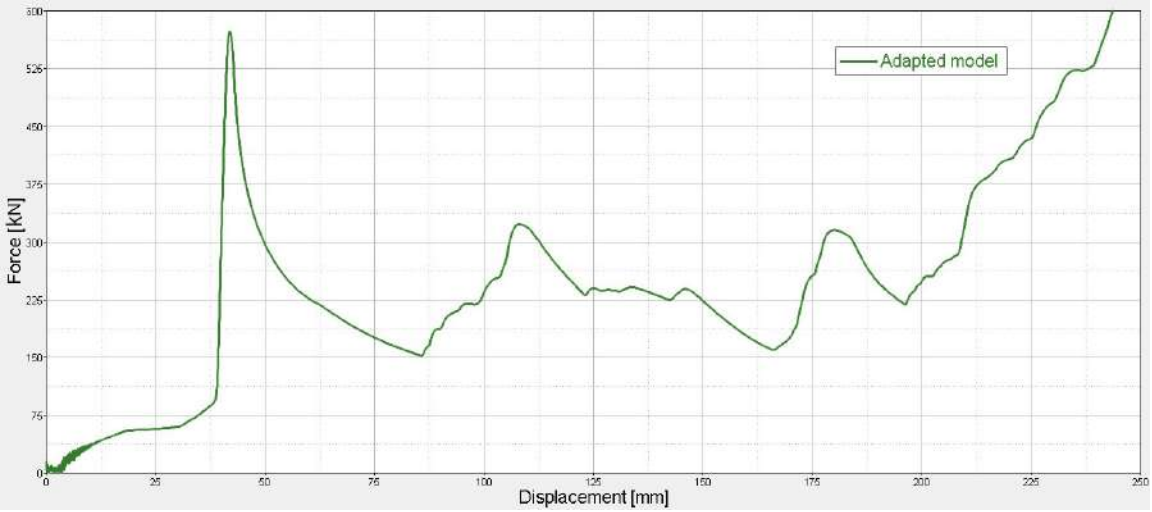

Figure 5.8: Adapted quasi-static model force vs displacement curve

From Figure 5.8, it is clear that the force will most likely exceed the maximum force of the test machine. Taking this into account, it will be tested if compressing half of the structure (one crash box) would be within the limits. The setup was modified to use only half of the structure, considering a symmetry boundary condition in the middle plane as shown in Figure 5.9.

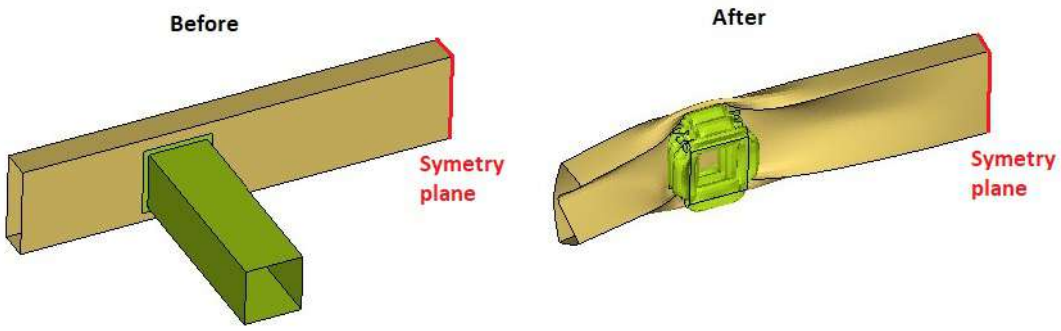

Figure 5.9: Half structure quasi-static model

The results show that the initial peak is expected to be higher than the machine maximum load value, as shown in Figure 5.10. The procedure was performed anyway since this value is only 13% above the maximum load value and it was considered that it was within the machine safety limits.

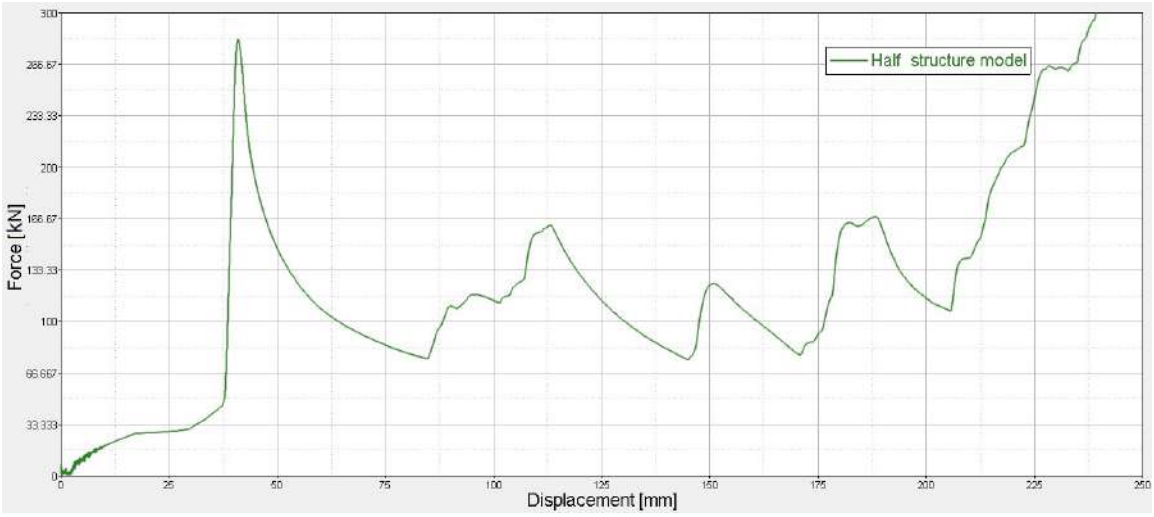

Figure 5.10: Half-structure force vs displacement curve

5.2.2 Experimental Compression Test

Setup

After programming the machine for a test speed of 10mm/min and a displacement of 150 mm, the first specimen was fixed to the platform as shown in Figure 5.11. This value of displacement was the maximum possible for the used hydraulic test machine.

One side of the structure is fixed while on the other side the structure is compressed against the table. In this case, the table was protected with a steel plate that represents the rigid wall in the model. The force will be applied from top to bottom and measured by a load cell. This corresponds to the force in the rigid body used in the model and both will be compared.

The same procedure was repeated for one of the crash boxes of specimen 2. Specimen 3 was compressed in both crash boxes at different speeds, 10 mm/min and 30 mm/min to see the influence of

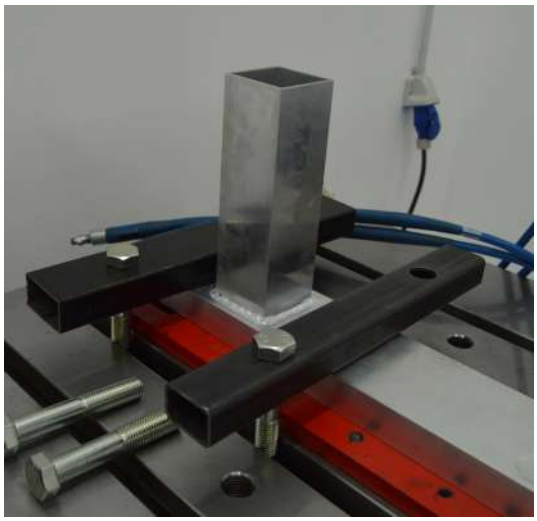

Figure 5.11: Fixing strategy for the compression procedure

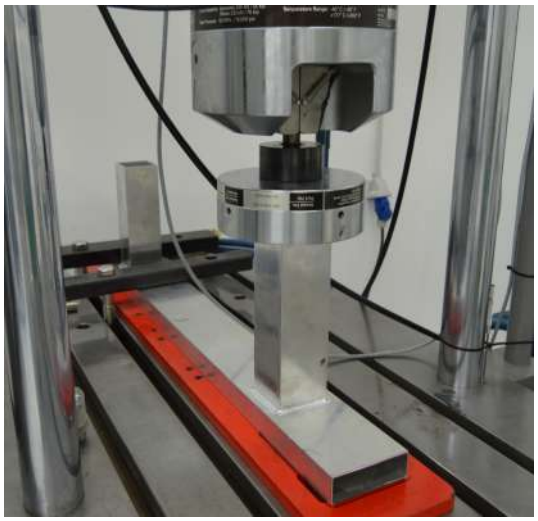

Figure 5.12: Final setup for the compression procedure

compression speed in the force-displacement curve.

Results

At the end of each compression test, the data was collected and the force-displacement curves are shown in Figure 5.13. The procedure was recorded in video and the final shape was photographed as shown in Figure 5.14.

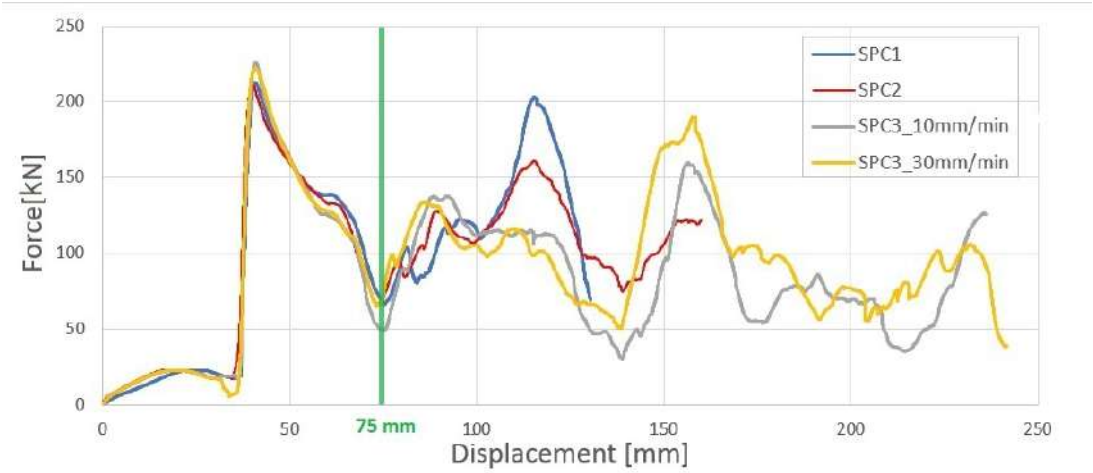

Figure 5.13: Compression procedure force-displacement curves

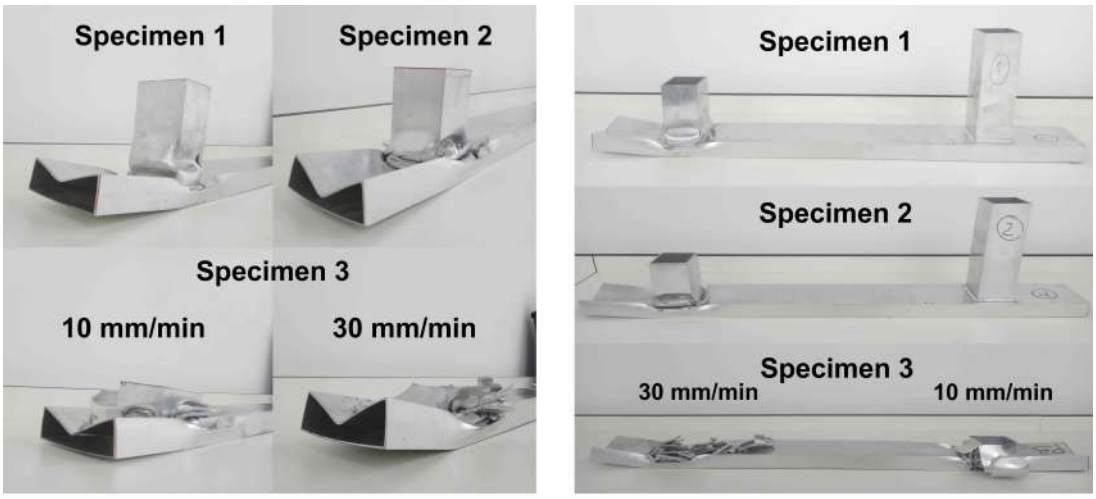

Figure 5.14: Final shape of the 4 compressed crash boxes

Extensive fracture was observed in all specimens. The fracture initiated in all the cases for a displacement value close to 75 mm. It is clear that, after that value, the curves do not have a good correlation. The expected deformation pattern was not observed in any of the specimens. This was expected since the material had lower ductility than required. In Figure 5.15 a comparison between a similar compression test made to a 6061-T6 aluminum tube is made. The best option would be to repeat this procedure with a material with the desired properties, but that was not possible for the time available for this work.

Figure 5.15: Comparison between the computational model, the expected result [81] and the obtained result

The comparison between the experimental results and the quasi-static numerical model force-displacement curve is represented in Figure 5.16. Taking into account that the first fracture occurred at around 75 mm of displacement, it is clear that, after fracture, the curves do not have a good correlation.

Despite the results, the model and the tested structures had the initial peak at 40 mm of deformation and the force before fracture is comparable. The model shows a good correlation with other axial compression tests made with a material with the desired properties [81] in terms of deformation pattern. Taking this into account, the model is considered valid before fracture and it is expected that a material with the desired ductility would not break in this procedure and would have a closer correlation to the numerical model in all the stages of compression. For that reason, in Chapters 6 and 7, the alloy chosen in Chapter 3 (6061 T6 Aluminum) will be used to build the dynamic model and perform the optimization process.

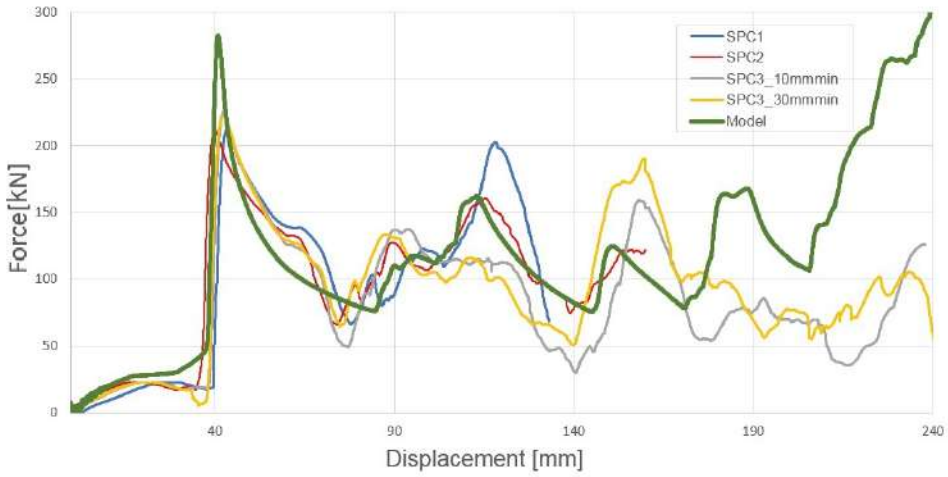

Figure 5.16: Experimental results vs quasi-static model

Chapter 6

Dynamic Approach

With the main goal of this work in sight, the structure must be improved to perform as well as possible in a crash situation. The two most important motivations are the safety of the passengers and the performance in the crash test made by NCAP at 50 km/h onto a rigid wall.

The main difference between this work and many other studies made to these kind of structures in the last years is the approach. The improvement will be made using a dynamic crash test and testing different solutions to improve the performance of the bumper. The most common approach is to test the structures in a quasi-static model and evaluate their energy absorption capability and performance. This kind of procedure allows an improvement of these quantities and a better understanding of some parameters effect in the performance. The problem is the generality of this test. The tested structures are always deformed in the same range of deformation and at the same constant imposed velocity.

To make the structure meet a specific goal for a given vehicle project, it is important to take into account the mass of the vehicle and the vehicle speed at the moment of the crash. That way, the energy that the bumper structure is supposed to absorb in a specific front crash situation can be optimized.

According to Campos et al. [56], the percentage of energy absorbed by the bumper deformable structure in a compact car is about 40%. In the present work, the goal will be an energy absorption of 50% of the crash energy by this structure for a vehicle of approximately 1400 Kg, with the best possible performance. This goal was proposed by CEiiA as project requirements.

The dynamic test will be performed considering that the rest of the vehicle structural parts (i.e. chassis) will be designed to deform after the bumper. This way, if the bumper does not absorb all the energy in the optimum range of deformation, the structure will have force spikes that will be evaluated by the CFE parameter. The SEA parameter will mostly be affected by the change in mass of the structure because the EA will be similar in each test, corresponding to the kinetic energy of the vehicle.

Apart from the crashworthiness criteria, it is important that this EA process meets the requirements imposed by the regulations. These limits are imposed for a full vehicle crash test with dummy. Due to the time line of this thesis and the early stage of the Be02 project, it is impossible to build a model for the whole vehicle and dummy, so some assumptions have to be made.

The three requirements in a front crash test imposed by NHTSA, as mentioned in Section 2.2, are:

- The acceleration in the dummy's chest must be less than 60 G's;
- The chest must not suffer a compression superior to 76.2 mm;
- The maximum allowable value for HIC is 1000.

None of these values can be measured in the used model but the deceleration in the rigid body can be obtained and will be close to the cockpit's deceleration. If the restraint system is considered rigid, the dummy's chest will have the same deceleration of the vehicle, so a upper limit of 60 G's will be taken into account when evaluating the force-displacement curves.

As mentioned before, the HIC is calculated using the head's acceleration. This acceleration is substantially different from the vehicle's deceleration [82], so this parameter will not be considered in this study.

As shown in Figure 2.10, the NCAP evaluation is done evaluating the values of chest G's and HIC. Having only an approximation for the value of chest G's, this value should be minimized during the optimization.

6.1 Dynamic Setup

To convert the quasi-static model to a dynamic model, two important modifications need to be made. The speed should be specified for the beginning of the test and mass should be added representing the vehicle. In the end, the bumper should be able to absorb the kinetic energy and stop in a controlled and effective way.

Performing a dynamic simulation introduces noise and vibration in the model results. In the crash tests performed by ECE, the data from accelerations is measured with a Channel Frequency Class (CFC) of 1000 [83]. Using filter options from *HyperView®*, the raw data from the dynamic test will be treated with a CFC of 1000 filter to reduce noise and have a better correlation with the data that would be measured in a real crash test. The two modifications added to make the setup dynamic are explained next.

6.1.1 Initial Velocity

In a crash test, the vehicle has a pre-defined velocity at which impacts the rigid wall. For the NCAP rigid wall front impact test, this speed is 50 km/h. All the structure is supposed to have that speed when the impact occurs and then stop at the end of the crash.

Using *HyperCrash™* setup options, it is possible to replace the imposed velocity added to the rear end of the bumper in the quasi-static test for an initial velocity in all nodes of the structure. The initial velocity will be specified as 50 km/h but not imposed to the rest of the crash. Figure 6.1 illustrates that.

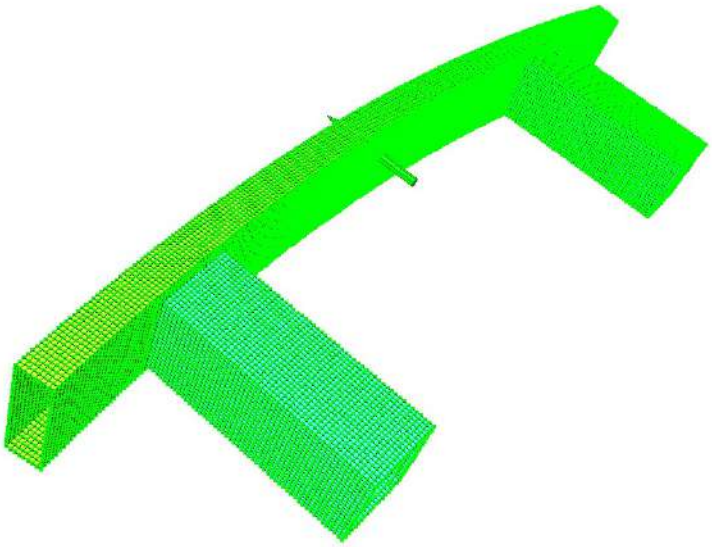

Figure 6.1: Initial velocity of 50 Km/h added to all nodes

6.1.2 Added Mass

On *HyperCrash*^{TM}, when creating a rigid body is possible to add mass to those bodies. In this model, the mass will be added to the previously created rigid bodies in the back end of the two crash boxes (Figure 6.2).

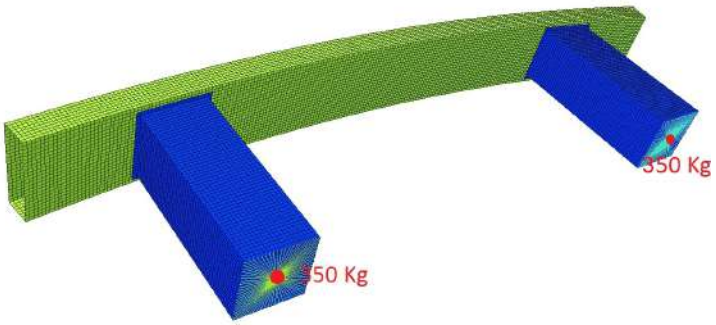

Figure 6.2: Mass added to the rigid bodies

To have the structure absorbing 50% of the kinetic energy of the vehicle, the mass added to the rigid bodies, representing the mass of the vehicle, will be half of the expected vehicle's mass. The kinetic energy is directly proportional to the mass and to the square of the velocity,

$$E_k = \frac{1}{2}mv^2. \tag{6.1}$$

Inserting 350 Kg on each of the rigid bodies and performing the crash test is a decent approximation.

It is expected that in the end of this study, the structure is optimized for a specific vehicle in a specific crash situation. It is also required that the methodology used for this evaluation and improvement can be adapted for a different set of requirements regarding a different crash setup and vehicle.

6.2 Quasi-Static vs Dynamic Model

Both Quasi-Static and Dynamic test force-displacement curves were compared in terms of force distribution and deformation pattern to evaluate the comparability of both tests .

In Figure 6.3 it is possible to see that the deformed structures are almost identical and both curves have a good correlation in all of the crash and compression stages.

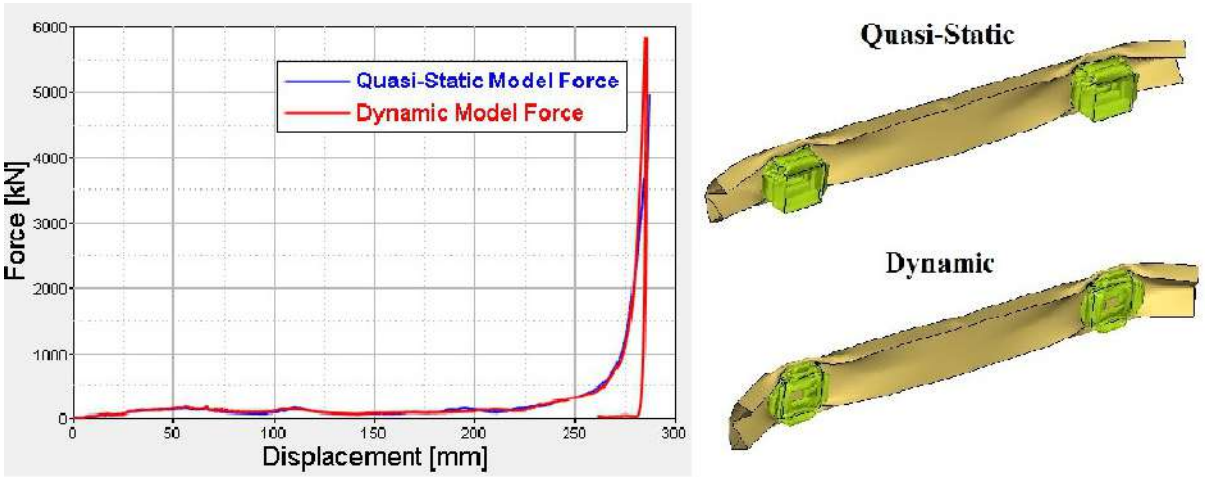

Figure 6.3: Comparison between quasi-static and dynamic tests

Both curves have a high peak of force at the end. In the quasi-static one, this peak happens because the structure was compressed over the maximum displacement. At that point of the test, all the structure cannot deform any further, and the force grows exponentially. The same happens in the dynamic test but this growth in force stops when all the kinetic energy is absorbed and the structure stops. The two curves can be compared in detail before this growth in force starts in Figure 6.4.

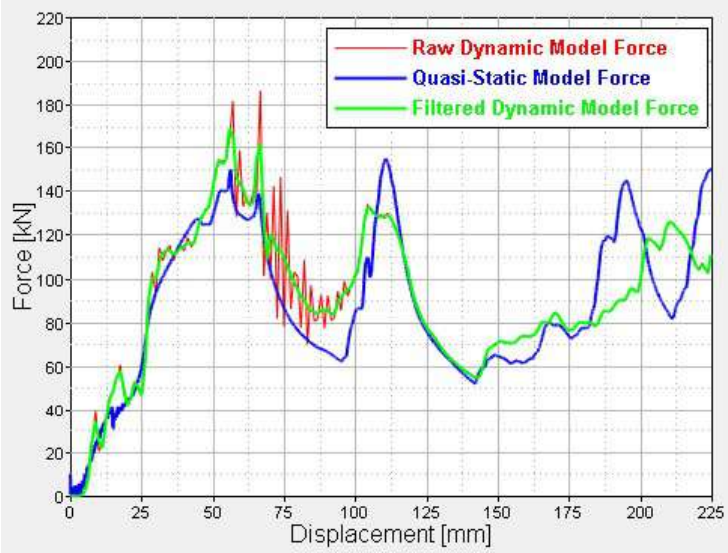

Figure 6.4: Comparison between quasi-static and CFC 1000 filtered dynamic test

It can be noted that both models are similar in terms of force displacement curves. However, when dimensioning the structure, all the curve should be considered because the structure should absorb

enough energy for a specific range of deformation to avoid the force peak in the end of the curve in Figure 6.3.

For the considered mass and speed values, the value for the kinetic energy is given by equation 6.1. As explained in the previous section the vehicle's mass is 1400 kg and the speed is 50 km/h ($\simeq 13.889 m/s$) resulting in a value for the kinetic energy of

$$E_k = \frac{1}{2} \times 1400 \times 13.889^2 = 135033 J. \tag{6.2}$$

The goal is to absorb 50% of this value with the bumper structure, so the baseline structure should absorb at least $67516.5 J$. In Table 6.1 the values for the absorbed energy of the quasi-static and the dynamic models are compared with the kinetic energy of the full vehicle.

Table 6.1: Energy absorption of quasi-static and dynamic models

	Quasi-Static	**Dynamic**	**Kinetic Energy**
EA [J]	19780	20609	135033.0
$\%E_k$	15	15	100

These values show that the baseline structure cannot absorb enough kinetic energy of the considered impact test. The maximum value of acceleration can also be calculated to evaluate if the structure is not going above the established legal limit of 60 G's, described in the beginning of this Chapter. For the maximum values of force of both quasi-static and dynamic tests, the maximum acceleration can be calculated using Newton's second law

$$a_{max} = \frac{F_{max}}{m} m/s^2. \tag{6.3}$$

The values are listed in Table 6.2

Table 6.2: Maximum forces and accelerations of quasi-static and dynamic models

	Quasi-Static	**Dynamic**
F_{max} [kN]	154.6	168.9
Acceleration [G's]	23	25

Becomes clear that the baseline structure is not able to absorb enough energy. In terms of acceleration, it is expected that the structure does not go above the stipulated limit but, due to the lack of energy absorption, in the end of the deformation a peak in force will occur as shown in Figure 6.4 that will correspond to 852 G's of acceleration. This value is not acceptable and the structure will be changed in the optimization process discussed in Chapter 7 so it is able to absorb enough energy for a value of acceleration not exceeding the limit. The dynamic model will be used to iterate the structure.

Using the dynamic model will allow to mimic the real crash test and see of the structure is absorbing enough energy before reaching the maximum deformation. When all the kinetic energy is absorbed, the

structure will strop. With this model, computation time can also be saved. The impact of a structure using this model lasts up to 100 ms. Remembering that the explicit integration uses time steps, the quasi-static model has a computational time at least five times higher because the compression lasts at least 500 ms.

Chapter 7

Structure Optimization

In order to improve the structure crashworthiness, relevant changes to the geometry should be implemented and studied using the same crash model setup. The optimization will be made using a multi-objective method based on a goal-oriented parametric study.

The ideal approach is to choose a wide set of parameters and a wide range of values for each parameter of the geometry, choosing the best combination. However, testing every possible combination in a structure with a single part is a huge and time consuming job. For a structure with two or more parts, the necessary time to perform this evaluation is exponentially larger. For example, if 4 simple characteristics are chosen and 3 values for those parameters are studied for each of the parts (beam and crash boxes), the number of geometries to model in CAD, mesh, setup and run would be $3^8 = 6561$ as represented in Figure 7.1. With an optimistic estimate of one hour spend for each geometry, working 5 days a week for, 8 hours a day, this approach would take more that 3 years with a single person working on it, having the current available equipment.

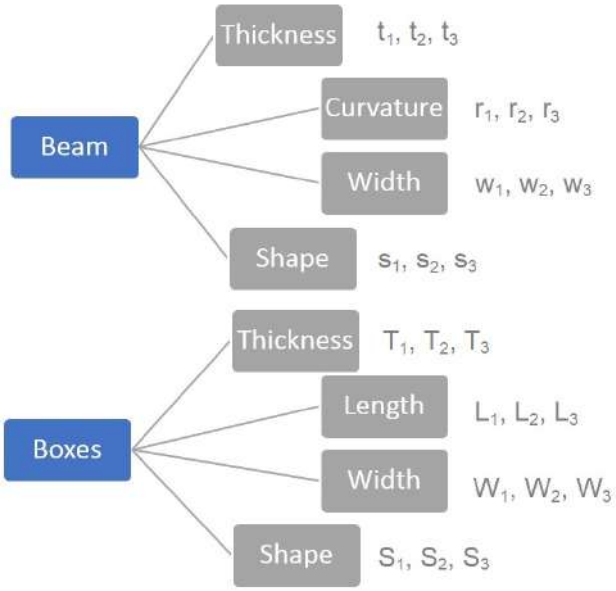

Figure 7.1: Example size of an exhaustive test procedure

In this thesis, the approach will be different, focusing on the performance deficits of the structure and testing several parameters at a time to get a better result. The changes in each step of the process will be based on the crashworthiness parameters analysis and the force vs displacement curve, aiming for a specific improvement in each iteration.

7.1 Performance Evaluation Using Pareto Analysis

A Crashworthiness Score (CS) will be used to compare the crashworthiness of each structure to the reference one, balancing the values of each of the crashworthines criteria. Weights can be defined for each of the two criteria as $w1$ and $w2$, having

$$0 < w1, w2 < 1 \tag{7.1}$$

and

$$w2 = 1 - w1. \tag{7.2}$$

The CS will be given for a specific weighting *i* as

$$CS_i = w_1 \frac{SEA_i - SEA_{ref}}{SEA_{ref}} + w_2 \frac{CFE_i - CFE_{ref}}{CFE_{ref}}. \tag{7.3}$$

In different scenarios with different requirements this weighting can be performed with a specific weighting but in the present work, a Pareto analysis will be used to evaluate the influence of each of the criterion and obtain the best design point considering a range of weightings.

A wide variety of problems arising in design optimization of engineering systems inherently involve optimizing multiple performance criteria. However, it is highly improbable that these conflicting objectives would both be ”extremized” by the same design. Hence the designer makes some trade-offs among the conflicting objectives in choosing the final design [84].

In multiobjective optimization problems, there are two primary approaches to finding the preferred, if not optimal, design. The first involves determining the relative importance of the attributes and aggregating the attributes into some kind of overall objective. Then, solving the optimization problem presumably would generate the optimal solution for a given set of attribute importances. The second approach involves populating a number of optimal solutions along the Pareto frontier and then selecting one based on the values of the attributes for a given solution [85]. This analysis will be used in several structure iterations, changing several parameters in each of the iterations.

For each value of w_1 and w_2, one of the geometries will have the highest CS and that is our optimum geometry for that weighting. All of the optimum geometries, corresponding to each of the weightings will be located in a chart and, in the end, that will be our Pareto chart that can be used to choose the best solution for the present project or any project using this process.

The points corresponding to the weightings of $w_1 = 1$ and $w_1 = 0$ will represent the limits of the set being correspondent to the geometries with higher SEA and higher CFE respectively. A utopia point

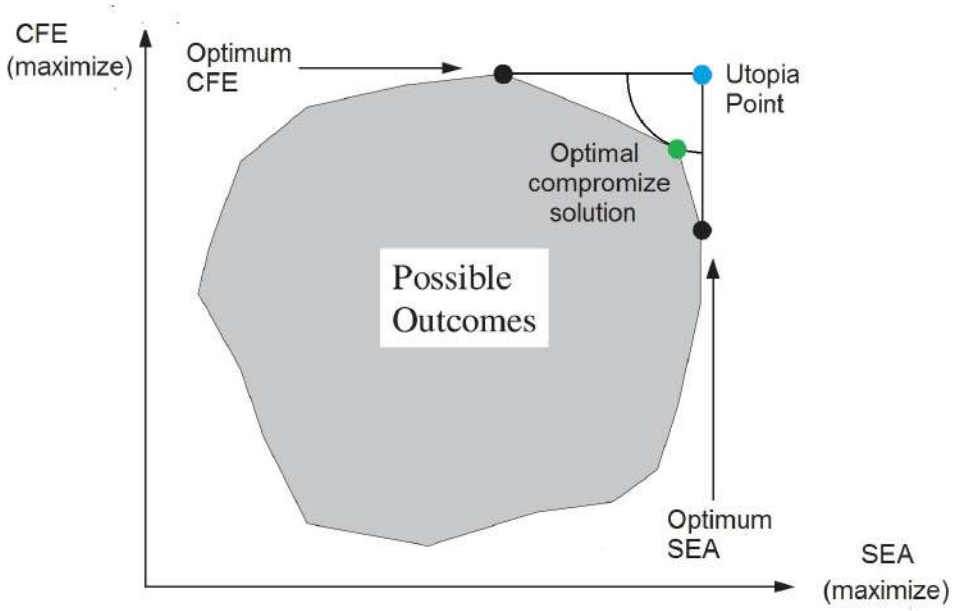

Figure 7.2: Pareto set example (adapted from [85])

having the maximum SEA and CFE can be identified and the best compromise solution will be the one that is non-dimentionally closer to this point as shown in Figure 7.2. This distance is evaluated by

$$d = \sqrt{\left(\frac{SEA_{max} - SEA_i}{SEA_{max} - SEA_{min}}\right)^2 + \left(\frac{CFE_{max} - CFE_i}{CFE_{max} - CFE_{min}}\right)^2}. \tag{7.4}$$

Regarding the regulations described in the beginning of Chapter 6, a limit of 60 G's will be imposed to the structure. At this point, if our optimal solution does not meet this requirement, the next point closer to the utopia point will be our optimal solution. In case none of the solutions meet this requirement, another set of changes should be tested until this criterion is satisfied.

After choosing one of the geometries, other parameters can be iterated and the process is repeated until an optimized structure is obtained.

7.2 First Iteration

The first iteration will be made to the crash boxes as they are the component that absorb most of the energy in a frontal crash. As concluded in Section 6.2, the current structure is not absorbing enough energy. The project goal is to get a structure that can absorb 50% of the kinetic energy without going above 60 G's of acceleration.T he baseline structure can only absorb 15% before the maximum deformation is reached and the force grows exponentially.

Two parameters were chosen to change in the crash boxes in order to improve their EA ability and minimize as much as possible any force peak in the vehicle.

7.2.1 Parameters

The chosen parameters are represented in Figure 7.3. For this first iteration, the length L of the crash boxes and the wall thickness A of this section will be changed and it is expected that an optimum solution is found.

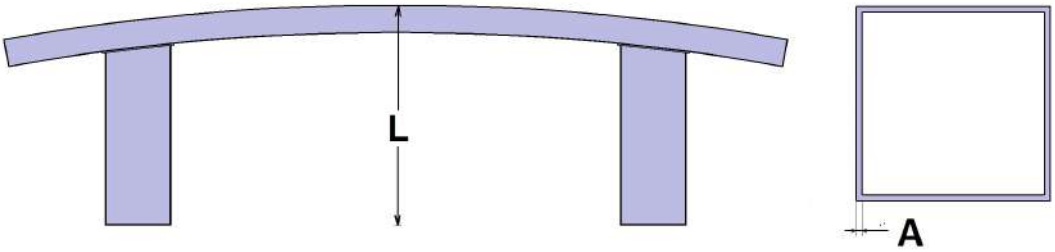

Figure 7.3: Parameters that will be changed in the first iteration

In Table 7.1 there is a list of the tested geometries for the crash boxes, maintaining the geometry of the beam. Five values for thickness and four for length were studied resulting in $5 \times 4 = 20$ geometries for this first iteration. REF 1 is the baseline structure, used in the model discussed in Chapter 6.

Table 7.1: First iteration geometries

Geometry Number	**REF 1**	**2**	**3**	**4**	**5**	**6**	**7**	**8**	**9**	**10**
A [mm]	2.0	2.0	2.0	2.0	2.5	2.5	2.5	2.5	3.0	3.0
L [mm]	300	400	500	600	300	400	500	600	300	400

Geometry Number	**11**	**12**	**13**	**14**	**15**	**16**	**17**	**18**	**19**	**20**
A [mm]	3.0	3.0	3.5	3.5	3.5	3.5	4.0	4.0	4.0	4.0
L [mm]	500	600	300	400	500	600	300	400	500	600

7.2.2 Results

After building each of the geometries in *CATIA™ V5*, mesh in *HyperMesh®* and implement the dynamic setup described in Section 6.1, all the geometries were tested and the results, obtained from *HyperView®*, are listed in Table B.1 (Appendix B). To calculate SEA, CFE and also the maximum acceleration in G's, each of the force-displacement curves were analyzed. The maximum force value can be obtained and the integral that represents the EA can be calculated by the software. The final displacement was also written down. Figure 7.4 shows an example of data gathering for one of the geometries. All the force-displacement curves can be found in Appendix A.4.

After all the necessary parameters are collected, SEA and CFE are calculated as described in Section 3.4 and the first Pareto set can be obtained and analyzed.

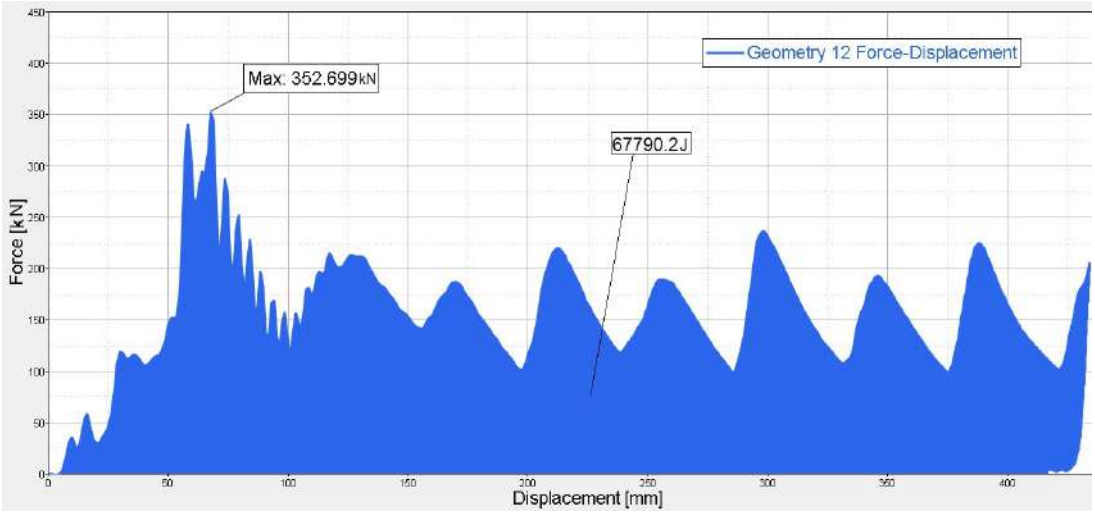

Figure 7.4: Example of data gathering (Geometry 12)

Using the process described in Section 7.1, with 101 different values for w_1 and w_2 (from 100% to 0% changing 1% in each), four optimum points were obtained as illustrated in Figure 7.5. Between values of 1 and 0.3 for w_1, the higher CS corresponded to Geometry 12. For values of w_1 between 0.29 and 0.05, the higher score was obtained using Geometry 14. For $w_1 = 0.04$ the higher CS corresponds to Geometry 17 and for values between $w_1 = 0.3$ and $w_1 = 0$, as expected, Geometry 1 had the best score because SEA is mostly influenced by mass and this was the lowest mass geometry.

Having the utopia optimum point at the right top corner of the Pareto set, the optimum geometry was chosen using equation (7.4). Also, the acceleration values must be considered in order to see of the chosen geometry satisfies the 60 G's criteria.

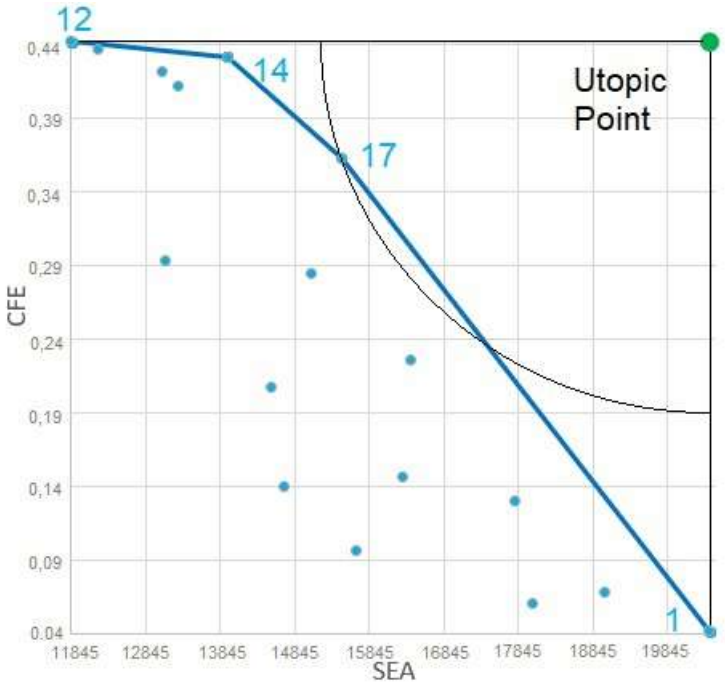

Figure 7.5: Pareto set of first iteration (each point corresponds to a different geometry)

In Table 7.2 it can be seen that the optimum corresponds to geometry 17 but this geometry, as well as geometries 14 and 1, has a value for maximum acceleration higher than 60 G's. So the choice for the first iteration was geometry 12, with 3 mm thickness and 600 mm from the front to the back of the structure.

Table 7.2: First iteration geometry choice

Geometry	SEA [J/kg]	%Δ SEA	CFE	%Δ CFE	d	Maximum acceleration [G's]
12	11845	-42.0	0.443	+959.0	1	51.4
14	13935	-31.7	0.432	+924.4	0.76	72.4
17	15467	-24.2	0.363	+769.7	0.61	114.1
REF 1	20412	–	0.042	–	1	851.9

When comparing geometry 12 with the reference geometry, a major improvement can be verified. The peak acceleration dropped from 851 G's to 51 G's, meaning that the initial criteria for the maximum acceleration is satisfied. The mass of this structure is close to 67% higher, resulting in a 42% decrease in SEA but having a 959% increase in CFE. The higher value of CFE means a more evenly distribution of force over the crash. This can be seen in Figure 7.6 where the improvement can be noted. The peak at the end of the crash was avoided because the structure was able to absorb all the energy before the maximum deformation value.

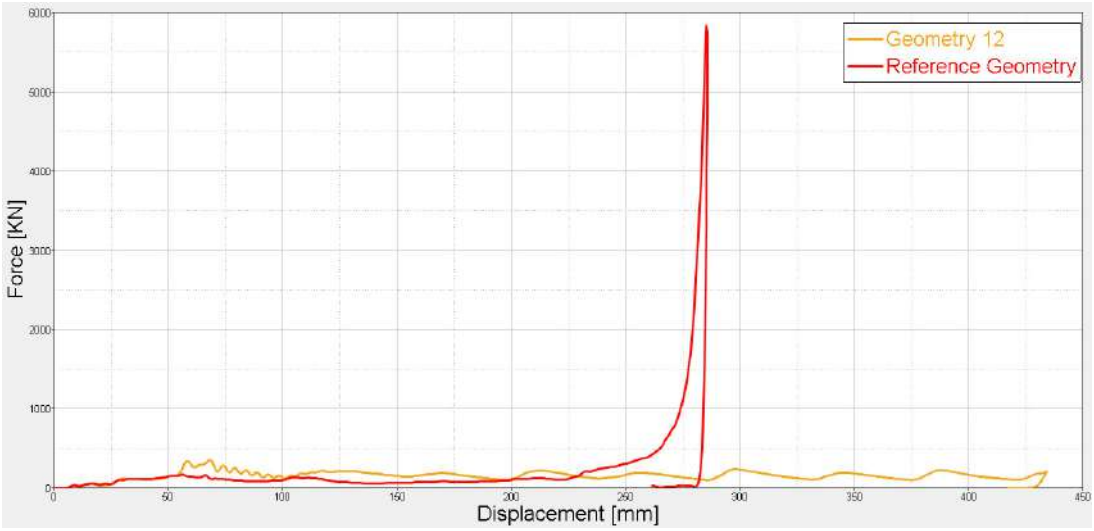

Figure 7.6: Comparison between the reference geometry and geometry 12 force-displacement curves

The geometry 12 force-displacement curve can be observed in better detail in previously shown Figure 7.4. In Figure 7.7 the final deformation of both structures, 1 and 12 is represented.

After analyzing the force-displacement curve of Geometry 12, it is necessary to spot any problem or lack of EA efficiency through the deformation process. Looking at Figure 7.4, while analyzing the deformation of the structure through the crash, it is possible to conclude that in the first 50 mm of the crash, knowing that the area of the curve represents the absorbed energy, the structure is absorbing less

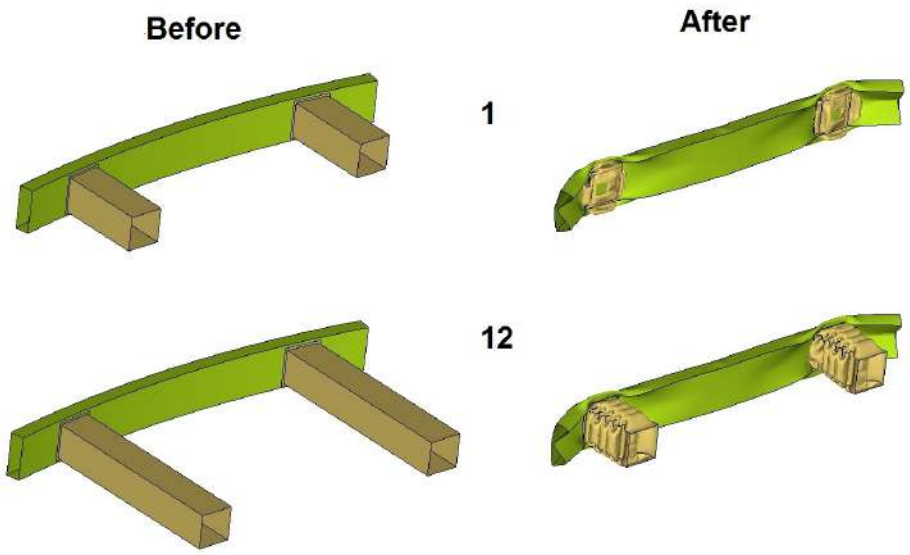

Figure 7.7: Comparison between reference geometry and geometry 12, before and after the impact

energy than after the first peak of force, that occurs at the start of the deformation of the crash boxes. After this peak, the first bend in the crash boxes occurs simultaneously in two faces of each crash box. After this bend, more bends are formed on each of the faces, each of them traducing in a peak in the force-displacement curve. Is also possible to see that the first 50 mm of the crash corresponds only to the deformation of the transverse beam, so the focus of the second iteration will be in the transverse beam structure to improve the performance of the structure in the first 50 mm of the crash.

7.3 Second Iteration

In the second iteration, the focus will be the beam and the same process will be used to determine the best solution of the chosen set of geometries.

Changing the transverse beam geometry, aiming for higher force values and a better EA performance in the beginning of the crash will be the goal of this iteration. The thickness and length of the crash boxes are kept constant using the optimal values of L = 600 mm and A = 3 mm found in the first iteration.

7.3.1 Parameters

In order to obtain a better distribution of force in the beginning of the crash, the beam must be reinforced. Two reinforcement options will be studied: the increase in thickness of the beam and the use of an internal rib that divides the interior of the beam, creating two closed cells. Also, in the first 20 mm of deformation, the force is specially low because this corresponds to the period when the curve transverse beam fits to the wall before starting to crush. Taking this into account, two more values of curvature will also be tested to have a better understanding of the influence of this parameter in the energy absorption performance.

The three parameters of this iteration are represented in Figure 7.8 and the values of each parameter for the corresponding geometry are listed in Table 7.3, being REF 5 the optimal solution found in the first iteration.

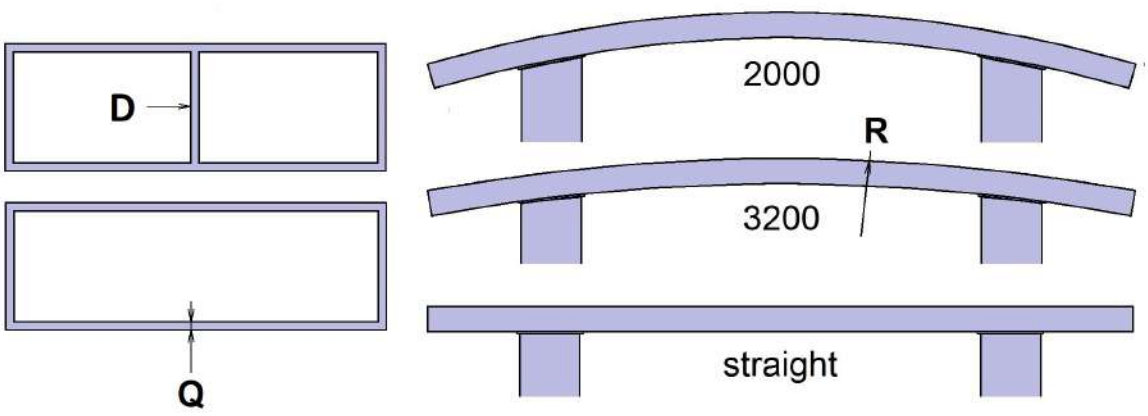

Figure 7.8: Parameters that will be changed in the second iteration

Table 7.3: Second iteration geometries

Geometry Number	**1**	**2**	**3**	**4**	**REF 5**	**6**	**7**	**8**
D [yes/no]	no	no	no	no	no	no	no	no
R [mm]	straight	straight	straight	straight	3200	3200	3200	3200
Q [mm]	2.5	3.0	3.5	4.0	2.5	3.0	3.5	4.0

Geometry Number	**9**	**10**	**11**	**12**	**13**	**14**	**15**	**16**
D [yes/no]	no	no	no	no	yes	yes	yes	yes
R [mm]	2000	2000	2000	2000	straight	straight	straight	straight
Q [mm]	2.5	3.0	3.5	4.0	2.5	3.0	3.5	4.0

Geometry Number	**17**	**18**	**19**	**20**	**21**	**22**	**23**	**24**
D [yes/no]	yes	yes	yes	yes	yes	yes	yes	yes
R [mm]	3200	3200	3200	3200	2000	2000	2000	2000
Q [mm]	2.5	3.0	3.5	4.0	2.5	3.0	3.5	4.0

7.3.2 Results

The same process used in the first iteration was followed and the data for each of the tested geometries was collected in Table B.2 (Appendix B).

For this iteration, the Pareto set, represented in Figure 7.9, has four points: Geometry 9 for $0 \leq w1 \leq 0.12$, Geometry 21 for $0.13 \leq w1 \leq 0.63$, Geometry 18 for $0.64 \leq w1 \leq 0.94$ and Geometry 12 for $0.94 \leq w1 \leq 1$.

Table 7.4 contains the data corresponding to the SEA, CFE, maximum acceleration and non-dimensional distance to the utopic point of each of the four geometries in the Pareto set, compared with the reference.

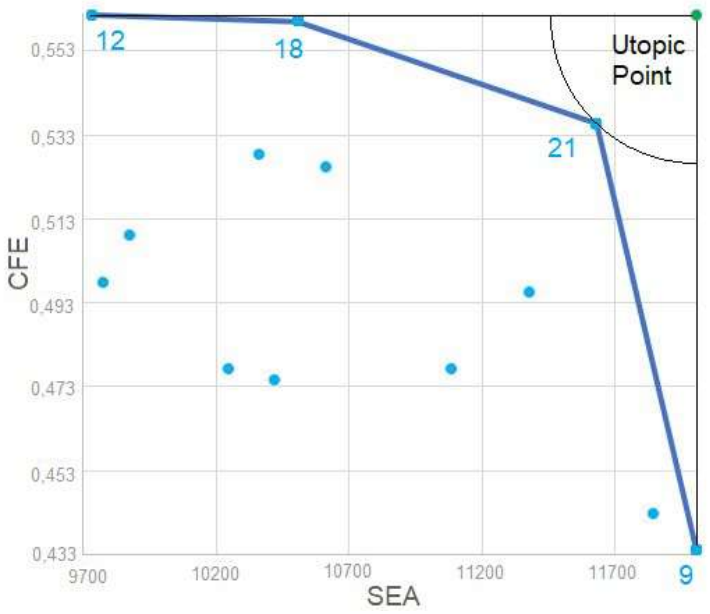

Figure 7.9: Pareto set of second iteration

Table 7.4: Second iteration geometry choice

Geometry	SEA [J/kg]	%Δ SEA	CFE	%Δ CFE	d	Maximum acceleration [G's]
12	9735	-17.8	0.562	+26.9	1	43.7
18	10508	-11.3	0.560	+26.5	0.66	43.0
21	11633	-1.8	0.536	+21.0	0.26	44.2
9	12007	+1.4	0.440	-1.9	1	51.3
REF 5	11845	–	0.443	–	–	51.4

Geometry 21, with internal rib, R = 2000 mm and Q = 2.5 mm has the closest point to the utopic point. Comparing the crashworthiness criteria of the geometry obtained in the first iteration (Geometry 5 in this iteration) with the new optimized solution, a 21% increase of CFE was verified with less than 2% decrease in SEA. The curvature was increased from a radius value of 3200 mm to 2000 mm. Both structures have the same wall thickness and the new structure weights 200 g more due to to the used rib. Observing the force-displacement curves comparison in Figure 7.10, it is clear that the established goal for this iteration was not achieved. Comparing the energy absorption of both structures in the first 50 mm of deformation, Geometry 5 absorbed 3350 J while Geometry 21 managed to absorb 4332 J. Although, the values of absorbed energy in this section are low when compared to the energy absorption in the rest of the crash. The first 50 mm of deformation still have a low force distribution but the overall efficiency was improved. The force peaks have been decreased and the average force increased. The new structure have a maximum peak that corresponds to 44 G's.

In general, the geometries with a transverse beam without curvature had a higher force at the beginning of the crash. Although this was an improvement in the amount of energy absorption in this phase of

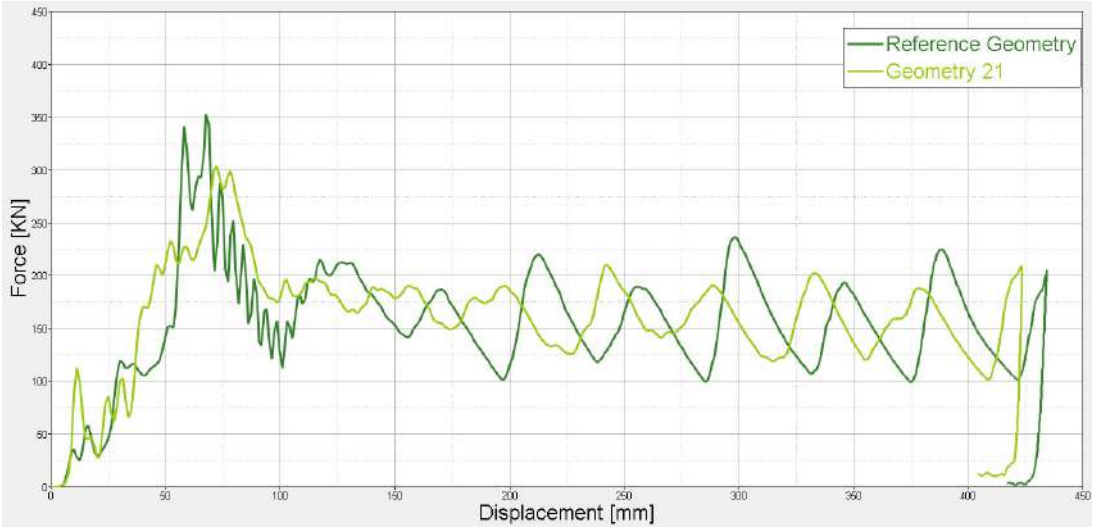

Figure 7.10: Comparison between the reference geometry and geometry 21 force-displacement curves

the deformation, the general crash performance of these geometries is substantially lower than the others, mainly because the first force peak is larger. Apart from lowering the correspondent CFE value, this peak also represents, in some cases, a maximum force that corresponds to an acceleration higher than 60 G's. The final deformation of the reference and the obtained structure, corresponding to Geometries 5 and 21 is represented in Figure 7.11and can be noted that the final shape is similar.

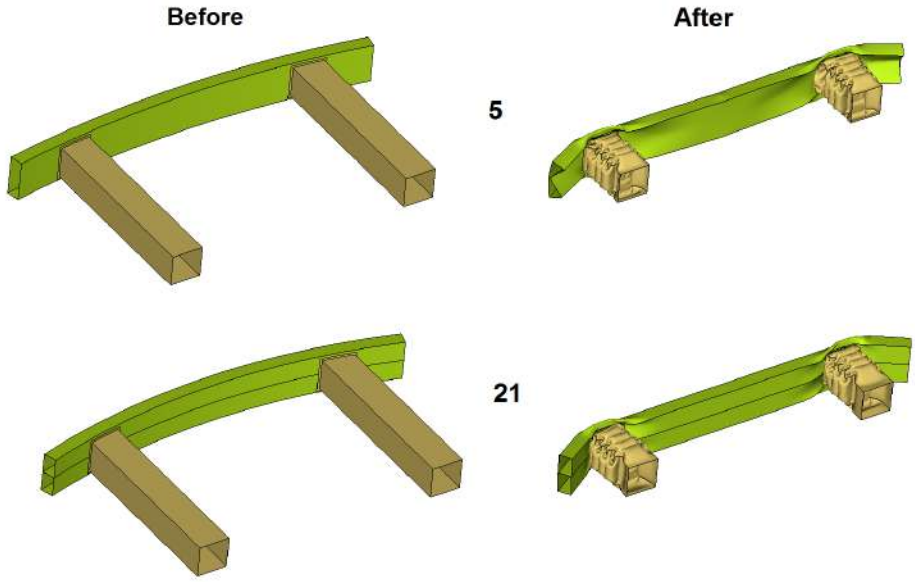

Figure 7.11: Comparison between the reference geometry and geometry 21 before and after the impact

7.4 Third Iteration

After two iterations to the geometry, the performance has been improved substantially. The improvement is mostly due to the improvement of CFE by lowering the peak force and growing the average force. At the start of the crash boxes deformation, still exists a higher force peak. In the third iteration, different sections will be tested for the crash boxes. The goal is to lower the initial peak or increase the overall force distribution to make it more uniform and, if possible, save weight without compromising the performance.

7.4.1 Parameters

Two more parameters will be studied to see their influence in the initial buckling of the structure as well as in the folding pattern, shape and width of the crash boxes.

In Figure 7.12, the shapes that will be used in this iteration are represented. In Table 7.5, the used values for weight and the shape of each geometry are listed. REF 3 is the optimal geometry from the second iteration.

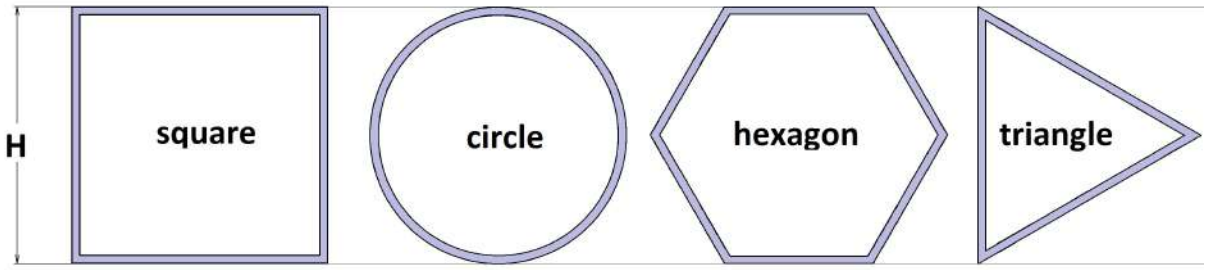

Figure 7.12: Parameters that will be changed in the third iteration

Table 7.5: Third iteration geometries

Geometry Number	**1**	**2**	**REF 3**	**4**	**5**	**6**	**7**
Shape	square	square	square	square	square	circle	circle
H [mm]	85	90	95	100	105	85	90

Geometry Number	**8**	**9**	**10**	**11**	**12**	**13**	**14**
Shape	circle	circle	circle	hexagon	hexagon	hexagon	hexagon
H [mm]	95	100	105	85	90	95	100

Geometry Number	**15**	**16**	**17**	**18**	**19**	**20**
Shape	hexagon	triangle	triangle	triangle	triangle	triangle
H [mm]	105	85	90	95	100	105

7.4.2 Results

The same process used in the first and second iterations was followed and the data for each of the tested geometries was collected in Table B.3 (Appendix B).

The three points in the Pareto boundary for this iteration are Geometry 16 for $0 \leq w1 \leq 0.06$, Geometry 6 for $0.07 \leq w1 \leq 0.57$ and Geometry 8 for $0.58 \leq w1 \leq 1$.

Following the same criteria, Geometry 6 was the choice after this iteration, having the lowest non-dimensional distance to the utopic point, as shown in Figure 7.13. Table 7.6 contains the data corresponding to the SEA, CFE, maximum acceleration and non-dimensional distance to the utopic point of each of the three geometries in the Pareto set, compared with the reference.

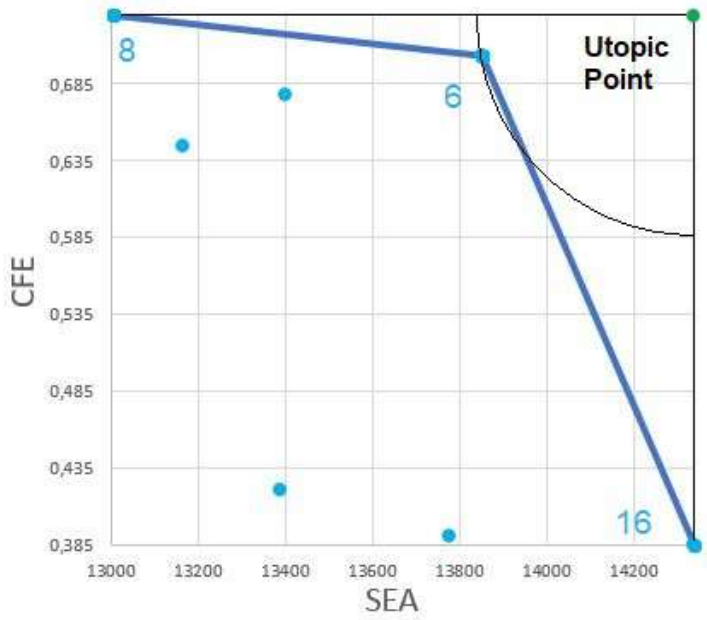

Figure 7.13: Pareto set of third iteration

Table 7.6: Third iteration geometry choice

Geometry	SEA [J/kg]	%Δ SEA	CFE	%Δ CFE	d	Maximum acceleration [G's]
8	13008	+11.8	0.729	+36.1	1	40.6
6	13852	+19.1	0.703	+31.3	0.37	39.8
16	14339	+23.3	0.385	-28.1	1	54.8
REF 3	11633	–	0.536	–	–	44.2

Comparing the crashworthiness criteria of the geometry obtained in the second iteration (Geometry 3 in this iteration) with the new optimized solution, a 31% increase of CFE and a 19% increase in SEA was verified. The increase in CFE was caused by the decrease in the peak force, and the increase of the average force, meaning that the main goal of this iteration was achieved. The maximum acceleration was reduced from 44 G's to 40 G's and the force in the rest of the crash was increased.

The circular section had a major influence in the performance, allowing the decrease in width, from 95 mm to 85 mm, of the crash boxes thus reducing weight and increasing SEA.

Analyzing the force displacement curve as well as the final deformation comparison in Figures 7.14 and 7.15, it can be noted that the new structure did not deform completely, being able to absorb all the impact energy with lower deformation of the structure.

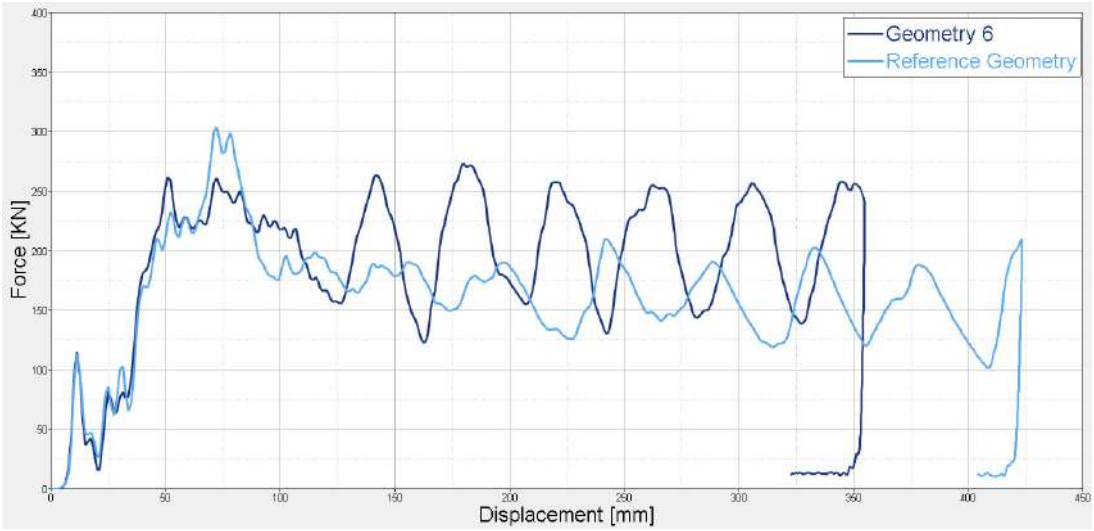

Figure 7.14: Comparison between the reference geometry and geometry 6 force-displacement curves

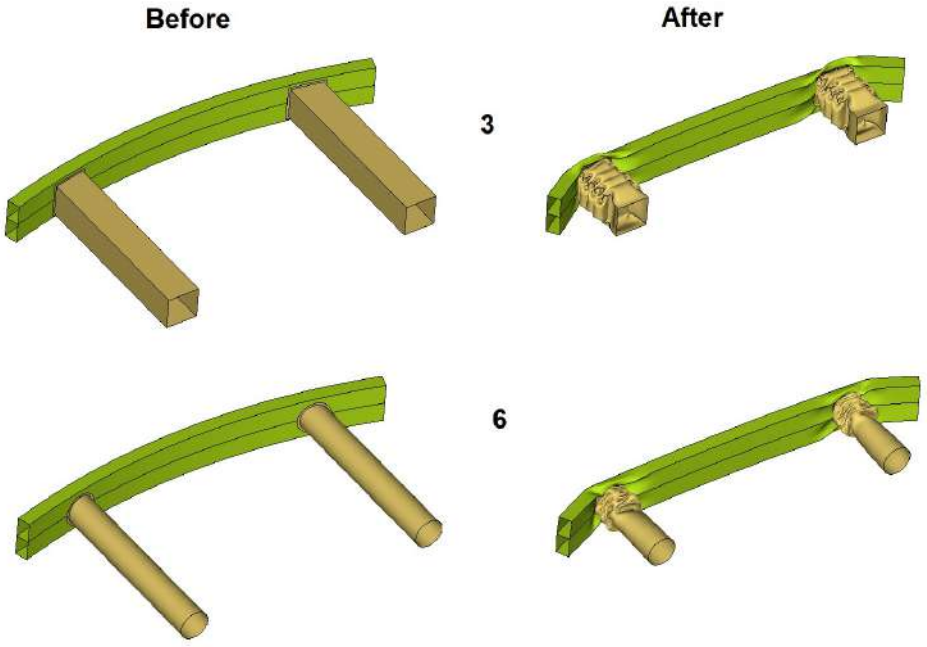

Figure 7.15: Comparison between the reference geometry and geometry 6 before and after the impact

The circular crash boxes had, by far, the best uniformity in force through the crash, as seen in Appendix A.4 (Figures A.5 to A.8). It can also be concluded that this uniformity is related with the number of faces. The geometries with more faces had a better force distribution and that makes sense since, by increasing the number of faces it gets closer to a circle.

7.5 Fourth Iteration

At this point, the value of CFE reached 0.7 that is a satisfactory value for this parameter. The next approach will have a main goal of weight decrease, trying to make the structure as light as possible, without affecting the value of CFE significantly. If the weight is decreased, it is expected that the performance will be higher having an increase in SEA.

As mentioned before, the transverse beam absorbs a negligible amount of energy on a front crash when compared to the crash boxes. In particular, for the present structure (Geometry 6 of iteration 3) the energy absorbed by the transverse beam was 12% of the total energy.

7.5.1 Parameters

Having that in mind, the section of the beam will be changed to reduce weight. The tested structures will have reduced widths as well as a smaller size for the front and rear surfaces. In order to maintain the joining technique of the two parts, a minimum of 100 mm for the rear surface was established so the crash boxes can be welded in the same way.

In Figure 7.16 the reference section for this iteration is at the left and the changed measurements at the right. Table 7.7 has the list of all the geometries and corresponding measurements. REF 10 corresponds to the geometry obtained from the third iteration.

Table 7.7: Fourth iteration geometries

Geometry Number	**1**	**2**	**3**	**4**	**5**	**6**	**7**	**8**	**9**
Z [mm]	20	20	20	20	20	20	20	20	20
B [mm]	120	120	120	110	110	110	100	100	100
l [mm]	120	90	60	120	90	60	120	90	60

Geometry Number	**REF 10**	**11**	**12**	**13**	**14**	**15**	**16**	**17**	**18**
Z [mm]	40	40	40	40	40	40	40	40	40
B [mm]	120	120	120	110	110	110	100	100	100
l [mm]	120	90	60	120	90	60	120	90	60

Geometry Number	**19**	**20**	**21**	**22**	**23**	**24**	**25**	**26**	**27**
Z [mm]	60	60	60	60	60	60	60	60	60
B [mm]	120	120	120	110	110	110	100	100	100
l [mm]	120	90	60	120	90	60	120	90	60

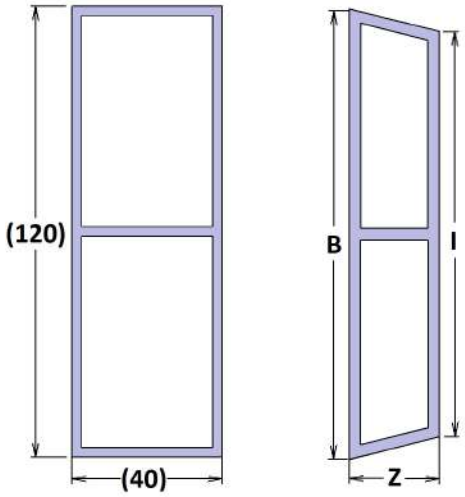

Figure 7.16: Parameters that will be changed in the fourth iteration

7.5.2 Results

The same process used in the the previous iterations was followed and the data for each of the tested geometries was collected in Table B.4 (Appendix B).

The three points in the Pareto boundary for this iteration are Geometry 9 for $0 \leq w1 \leq 0.40$, Geometry 8 for $0.41 \leq w1 \leq 0.72$ and Geometry 10 for $0.73 \leq w1 \leq 1$.

Following the same criteria of the previous iterations, Geometry 8 was the choice after this iteration, having the lowest non-dimensional distance to the utopic point, as shown in Figure 7.17.

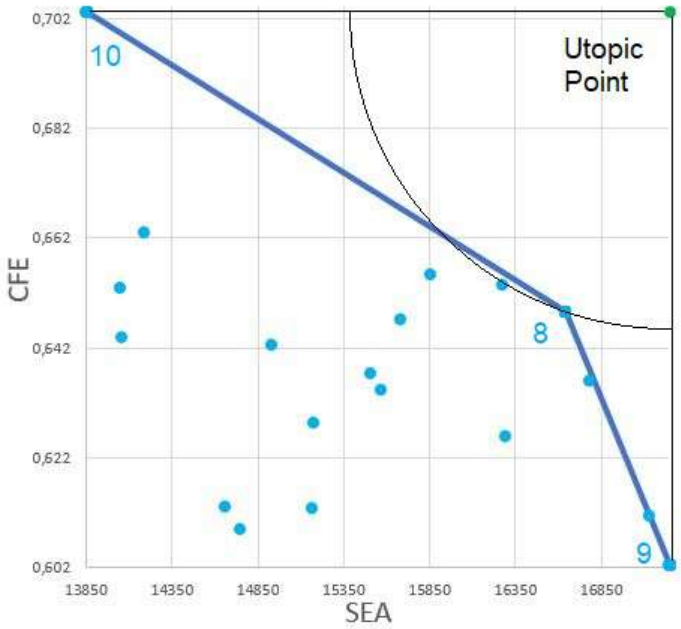

Figure 7.17: Pareto set of fourth iteration

Table 7.8 contains the data corresponding to the SEA, CFE, maximum acceleration and non-dimensional distance to the utopic point of each of the three geometries in the Pareto set.

Table 7.8: Fourth iteration geometry choice

Geometry	SEA [J/kg]	%Δ SEA	CFE	%Δ CFE	d	Maximum acceleration [G's]
REF 10	13852	–	0.703	–	1	39.8
8	16642	+20.1	0.649	-7.8	0.57	41.7
9	17249	+24.5	0.602	-14.3	1	44.8

In Figure 7.18 it is clear that the force distribution was not substantially affected but the weight of the structure was reduced in 1 kg that represents 20%. This translated into a 20% increase in SEA with less than 8% decrease in CFE, meaning that the goal of this iteration was achieved. The range of the deformation was also similar as shown in Figures 7.18 and 7.19.

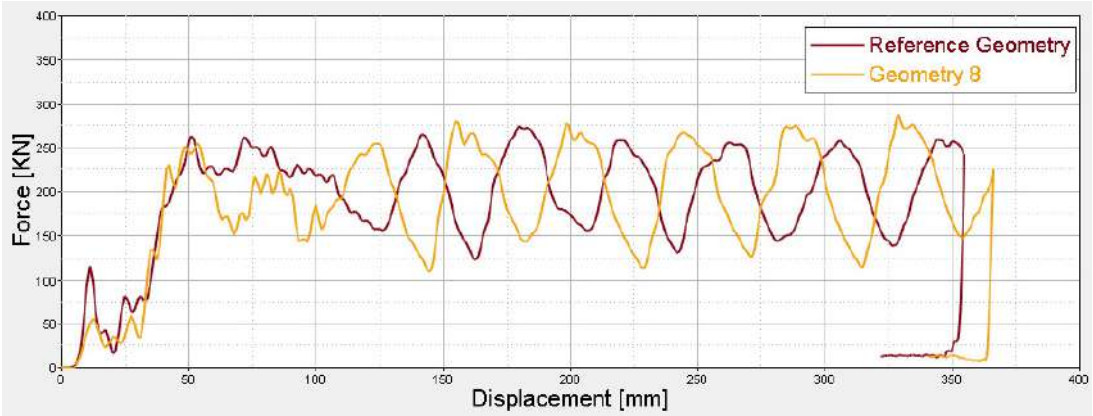

Figure 7.18: Comparison between the reference geometry and geometry 8 force-displacement curves

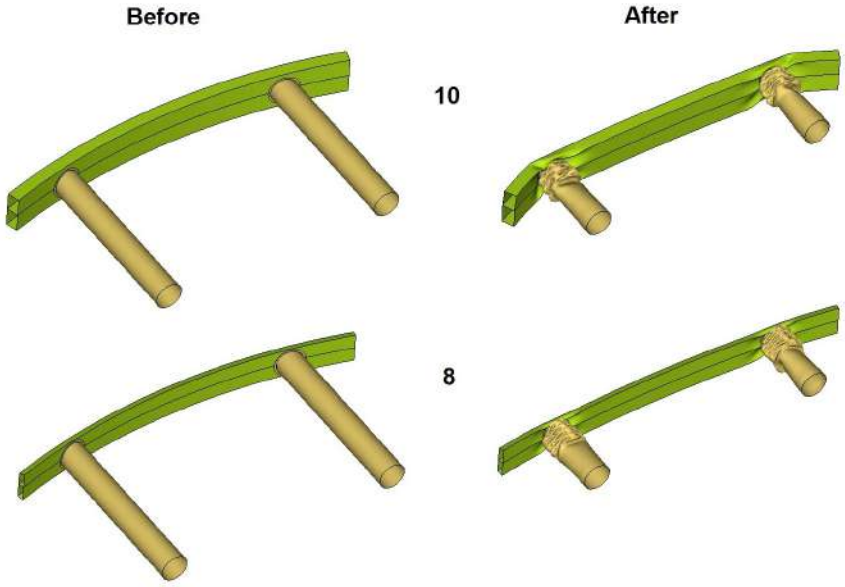

Figure 7.19: Comparison between the reference geometry and geometry 8 before and after the impact

7.6 Final Results

The iterative process described in the previous sections can be repeated for new parameters or done again, iterating the obtained structure with the same parameters. Doing this, it is expected that the optimum structure with all the parameters used in the four iterations converges to a final optimized structure.

At the end of the fourth iteration, as expected, the final structure has a better performance in general, when compared with the initial reference. The comparison between the two, in terms of shape and deformation pattern is shown in Table 7.9 and Figure 7.20.

Table 7.9: Initial vs final geometries measurements

Geometry	A [mm]	L [mm]	D [yes/no]	R [mm]	Q [mm]	Shape	H [mm]	Z [mm]	B [mm]	I [mm]
Initial	2	300	no	3200	2.5	square	95	40	120	120
Final	3	600	yes	2000	2.5	circle	85	20	100	90

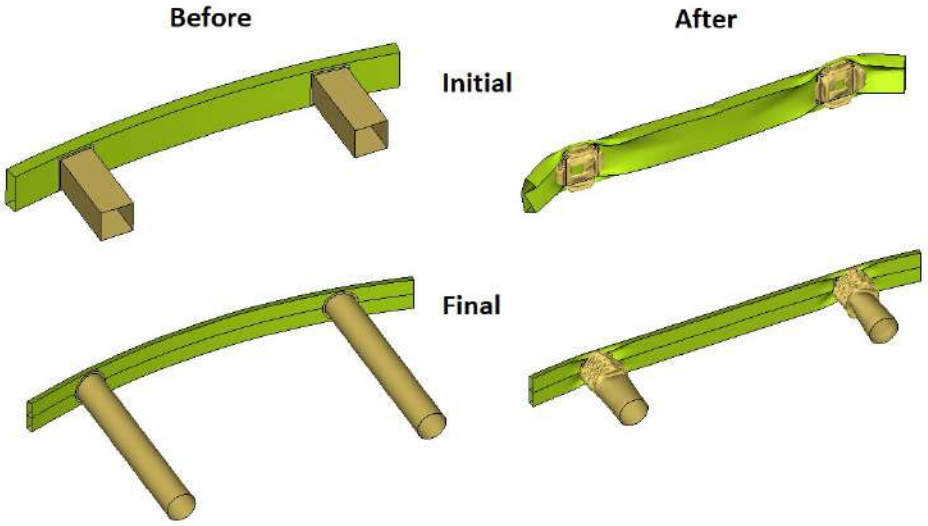

Figure 7.20: Comparison between the initial geometry and the resultant of the optimization process

Table 7.10 sums the improvement made to the structure after the four iterations.

Table 7.10: Initial vs final geometries comparison

Geometry	SEA [J/kg]	%Δ SEA	CFE	%Δ CFE	Max. acc. [G's]	%Δ Max. acc.	Mass [kg]	%Δ Mass
Initial	20412	–	0.042	–	851.9	–	3.421	–
Final	16642	-18.5	0.649	+1451.8	41.7	-95.1	4.088	+19.5

The final structure has close to 20% more mass than the initial one, translating into a 19% decrease in SEA. The final structure is able to absorb energy with a force curve always below the maximum

established value of 60 G's and the CFE parameter increased more than 14 times, meaning that the force displacement curve is much more uniform than the initial one.

Compiling all the tested geometries in the four iterations in Figure 7.21, the progress of each iteration in terms of crashworthiness criteria is clear.

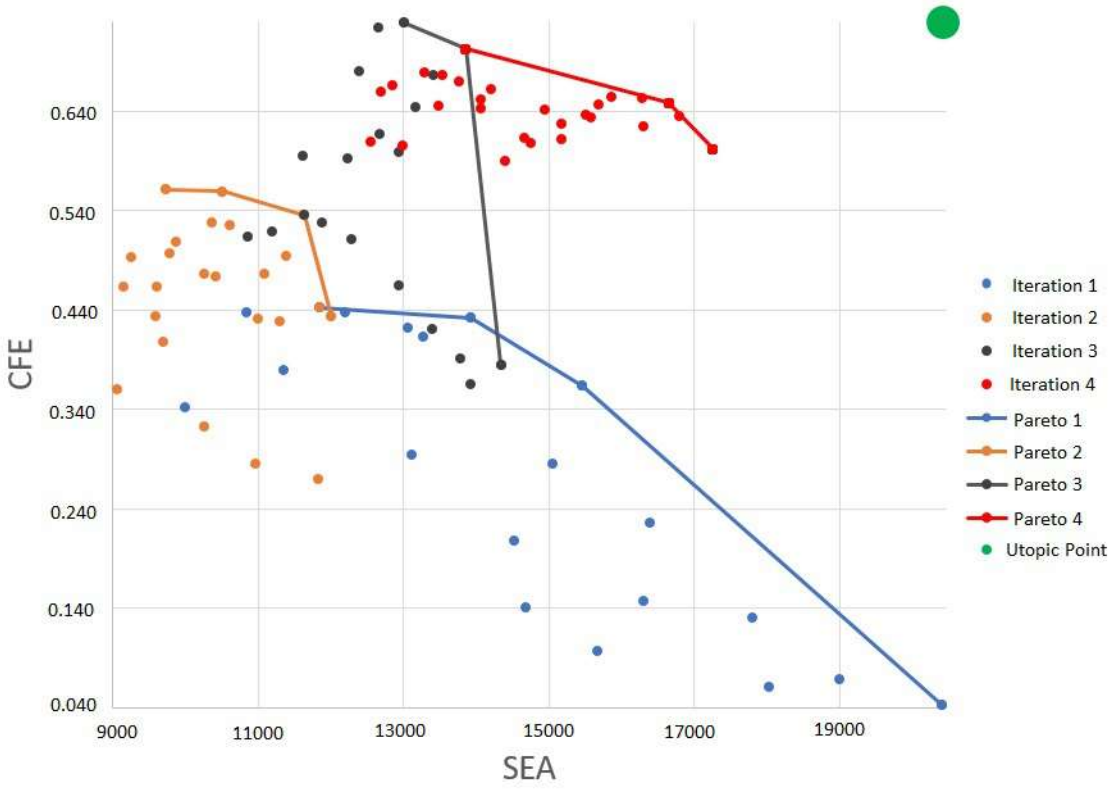

Figure 7.21: Final Pareto distribution

First Iteration

The first iteration had a major improvement in CFE while increasing mass. After this iteration, the maximum acceleration goal was already achieved. Analyzing all force-displacement curves of this iteration in Figures A.1 to A.4 (Appendix A), it can be noted that both length and thickness of the crash boxes raise the force needed for the deformation to occur. It becomes clear that, for a maximum length of 600 mm, both 2.5 and 3.0 mm thickness options cannot absorb all the impact energy before reaching the maximum deformation. This leads to a force peak at the end, similar to the initial geometry. The best result corresponds to the geometry that absorbs all energy before the end of the deformation and has less thickness (and weight).

Second Iteration

In the second iteration, the peak at the beginning of the crash boxes deformation was decreased. This happened because of the higher curvature of the transverse beam that caused a different initiation in the deformation of the crash boxes, with a lower value of force. The goal was to increase the force in

the first 50 mm of deformation but it was not archived even though the overall crash performance was improved.

Figures A.5 to A.10 show that, increasing the curvature of the beam, the crash-boxes start to deform for a lower initial peak, decreasing the maximum force and improving CFE. The thickness of the beam does not influence much the force displacement distribution so, as expected, the best performance corresponds to the lowest thickness, 2.5mm. The influence of the rib can be observed only at the first 50 mm of displacement, slightly increasing the force, leading to a more even distribution.

Third Iteration

After the third iteration, CFE was substantially improved as well as SEA, with a mass decrease of around 1 kg. This was the first time in this process that both crashworthiness criteria were improved, the new optimized point moved up and right in the Pareto set, overcoming the last optimized point in both criteria.

The decrease in weight was due to the decrease in width of the crash-boxes. This was only possible, without compromising the energy absorption, due to the improvement that circular crash boxes bring to the structure. Increasing the number of sides makes the force more even during the crash, as shown in Figures A.11 to A.14. For an infinite number of sides, the section becomes a circle, so the obtained result makes sense. It can also be concluded that, for the same number of sides, width does not influence the curves substantially.

Fourth Iteration

For the fourth iteration, the goal was to maintain or improve the performance of the structure while decreasing weight on the beam. The force-displacement distribution did not suffer a major change but the weight decreased around 1 kg , so the goal was achieved. SEA was improved with a low cost in CFE and this can be noted by the displacement of the optimum point to the right of the Pareto set.

In Figures A.15 to A.17, the similarity between all the curves can be noted, as well as the influence of the beam width in the beginning of the deformation. The decrease in this value leads to a decrease in the interval of displacement with lower forces in the beginning of the distribution, making the curve more even.

Initial vs Final

The baseline structure was not able to absorb all the impact energy as concluded in Chapter 6. After one iteration the resulting structure was able to absorb all the energy without going above the established acceleration limit. All subsequent iterations made improvements in the crashworthiness of the structure for a frontal impact setup. The final structure shows a major improvement in the performance, achieving and surpassing the established goals of this optimization process.

Chapter 8

Conclusions

During this work, corresponding to the early stage of the Be2 project where many specifications are yet to be set, the work was conducted in order to create knowledge and valuable tools that can be used in latter stages of the vehicle's development.

After all iterations and testing of a significant number of alternatives and parameters that influence the crash performance of the front Crash Management System (CMS), a robust numerical model was built. The material numerical formulation used has a good correlation with previous works regarding thin-walled beams axial compression, although it could not completely validated in this work due to lack of quality of the provided material by the suppliers at hand.

A versatile and adaptable multi-objective evaluation methodology was developed and proven to have good results by improving the structure, regarding the used crashworthiness criteria. This tool also provided a way to gather knowledge and build a "map" for future iterations. If new iterations were made to the structure, they would be based in this knowledge and the changed parameters would have a specific goal. This process can also be used for projects with different goals. The choice criteria can be changed and, for example, CFE can be prioritized if the weight of the structure is not an important factor. Either SEA is not calculated or this parameter can be ignored while choosing the optimum geometry, choosing the point that has higher CFE. These parameters could also be replaced with new ones to fit the requirements of another project.

The validation procedures provided insight about the influence of the material properties in the behaviour of the structure during axial compression.

8.1 Achievements

The major achievements of the present work can now be listed:

- A robust explicit non-linear numerical model was built, suitable for dynamic or quasi-static setups, using simple structures, composed by one ore more thin-walled beams with changeable shape and material;

- A solid multi-objective optimization procedure was achieved, that can be adapted to fit future goals of the project or any multi-objective project;
- The collected data and the evaluation system allows the gathering of information about the influence of each of the tested parameters in the crash performance;
- The final optimized structure meets the initial goals in terms of deceleration of the vehicle in the occurrence of a frontal impact similar to NCAP 50 km/h solid barrier front crash procedure;
- For a traditional bumper composed of a transverse beam and two crash boxes, the beam was proven to have low influence in terms of energy absorption during front collision;
- The curvature of the transverse beam was proven to be beneficial, initiating the crash box deformation for a lower value of force;
- The use of crash boxes of circular section was the best improvement in the optimization, providing a way to save weight, while improving the force-displacement curve.

8.2 Future Work

Taking into account that the model had a good correlation in terms of deformation pattern with some previous works in the field, it would be interesting to repeat the validation procedures with the desired material and geometry, in order to also validate the force-displacement curve.

Regarding the optimization procedure, it would be interesting to repeat the four iterations with the final geometry as reference until it converges to a single geometry. This would, most likely, have an inferior computational time when compared to the approach of testing every possible combination of the used parameters in the four iterations. Adding the four iterations, 91 geometries were tested. If all the parameter combinations were tested it would translate in $(5 \times 4) \times (2 \times 3 \times 4) \times (4 \times 5) \times (3 \times 3 \times 3) = 20 \times 24 \times 20 \times 27 = 259,200$ geometries. This represents a computational time almost 3000 times larger than the process used. It would also be interesting to check if the final converged geometry would correspond to the same result of the exhaustive approach. Programming all the process from the geometry creation to the analysis of the results and choice of an optimum geometry would also make this process more viable.

During a later stage of Be2 development, this work can advance to a more complex and detailed model. Having all the details of the vehicle, the model can grow into a full vehicle crash representation. Implementing a dummy on the full model would make possible to calculate the Head Injury Criterion (HIC) and check if the accelerations in the dummy's chest have a good correlation with the ones obtained with the bumper model.

Bibliography

[1] E. R. H. Fuchs, R. Roth, F. R. Field, and R. E. Kirchain. Strategic materials selection in the automobile body: economic opportunities for polymer composite design. *Composites Science and Technology Journal*, 68:1989–2002, Feb. 2008.

[2] World Health Organization. Global status report on road safety 2015.

[3] World Health Organization. Global status report on road safety 2013: Supporting a decade of action, 2013.

[4] European Road Safety Observatory. Annual accident report 2016. `ec.europa.eu/transport/road_safety/sites/roadsafety/files/pdf/statistics/dacota/asr2016.pdf`. Accessed February 2017.

[5] A. Sheshadri. Design and analysis of a composite beam for side-impact protection of occupants in a sedan. Master's thesis, Graduate School of Wichita State University, 2006.

[6] W. Johnson and A. G. Mamalis. Crashworthiness of vehicles. *London: Mechanical Engineering Publications Limited*, 1978.

[7] J. E. Morton. Structural impact and crashworthiness. *Elsevier Applied Science Publishers*, 2, 1984.

[8] N. Jones and T. Wierzbicki. Structural crashworthiness and failure. *New York: Elsevier Science Publishers*, 1993.

[9] G. Lu and T. Yu. Energy absorption of structures and materials. *Cambridge: Woodhead Publishing Limited*, 2003.

[10] A. Ghandianlou and S. B. Abdullah. Crashworthiness design of vehicle side door beams under low-speed pole side impacts. *Thin-Walled Structures*, 67:25–33, Mar 2013.

[11] L. Peroni, M. Avalle, and G. Belingardi. Comparisson of the energy absorption capability of crash boxes assembled by spot-weld and continuous joining techniques. *International Journal of Impact Engineering*, 36:498–511, Jul 2009.

[12] T. Tang, W. Zhang, H. Yin, and H. Wang. Crushing analysis of thin-walled beams with various section geometries under lateral impact. *Thin-Walled Structures*, Jan 2016.

[13] P. Khalili, F. Tarlochan, A. Hamouda, and K. Al-Khalifa. Energy absorption capability of thin-walled aluminum tubes under crash loading. *Journal of Mechanical Engineering and Sciences*, 9:1734–1743, Dec 2015.

[14] A. A. A. Alghamdi. Collapsible impact energy absorbers: an overview. *Thin-Walled Structures*, 39: 189–213, 2001.

[15] ECO. `eco.pt/2017/01/28/a-fiscalidade-dos-combustiveis-e-um-mana/`. Accessed August 2017.

[16] CEIIA. CEiiA - Mobility. `www.ceiia.com/mobility`. Accessed August 2017.

[17] PCT da Mobilidade. Mobicar. www.pctdamobilidade.com/en/projects/detail/6. Accessed June 2017.

[18] Diário de Notícias. `static.globalnoticias.pt/storage/DN/2015/dn2015_detalhe_topo/ng5512574.JPG`. Accessed June 2017.

[19] Vehicle certification agency. Definition of vehicle categories. URL `http://www.dft.gov.uk/vca/vehicletype/definition-of-vehicle-categories.asp`.

[20] Flaticon. `www.flaticon.com/packs/seo-7`. Accessed June 2017.

[21] X. Zhang, H. Zhang, and Z. Wang. Bending collapse of square tubes with variable thickness. *International Journal of Mechanical Sciences*, 106:107–116, 2016.

[22] J. M. Lahman. `www.jmlahman.com/`. Accessed March 2017.

[23] A. W. Orlowicz, M. Mróz, M. Tupaj, and A. Trytek. Materials used in the automotive industry. *Archives of Foundry Engineering*, 15(2):75–78, 2015.

[24] V. Tarigopula, M. Langseth, O. S. Hopperstad, and A. H. Clausen. Axial crushing of thin-walled high-strength steel sections. *International Journal of Impact Engineering*, 32:847–882, 2006.

[25] A. Segade, J. A. L. Campos, J. R. Fernández, E. Casarejos, and J. A. Vilán. Finite element simulation for analyzing the design and testing of an energy absorption system. *materials*, 2016.

[26] E. R. H. Fuchs, F. R. Field, R. Roth, and R. E. K. Kirchain. Strategic materials selection in the automobile body: Economic opportunities for polymer composite design. *Composites Science and Technology*, 68:1989–2002, 2008.

[27] S. Houa, Q. Lib, S. Longc, X. Yanga, and W. Li. Design optimization of regular hexagonal thin-walled columns with crashworthiness criteria. *Finite Elements in Analysis and Design*, 43:555–565, 2007.

[28] Metalmen. `www.metalmensales.com/aluminum.html`. Accessed February 2017.

[29] M. Pervaiz, S. Panthapulakkal, K. Birat, M. Sain, and J. Tjong. Emerging trends in automotive lightweighting through novel composite materials. *Materials Sciences and Applications*, 7:26–38, 2016.

[30] S. Das. Life cycle assessment of carbon fiber-reinforced polymer composites. *The International Journal of Life Cycle Assessment*, 16:268–282, 2011.

[31] B. D. Agarwal, L. J. Broutman, and K. Chandrashekhara. *Analysis and performance of fiber composites*. Wiley, 3 edition, 2006.

[32] Molded Fiber Glass Companies. Technical design guide for FRP composite products and parts - techniques & technologies for cost effectiveness, 2006.

[33] A. G. Mamalis, D. E. Manolakos, M. B. Ioannidis, and D. P. Papapostolou. The static and dynamic axial collapse of CFRP square tubes: finite element modelling. *Composite Structures*, 74:213–225, 2006.

[34] H. Zarei, M. Kroger, and H. Albertsen. An experimental and numerical crashworthiness investigation of thermoplastic composite crash boxes. *Composite Structures*, 85:245–257, 2008.

[35] Y. Tay, C. Lim, and H. Lankarani. A finite element analysis of high-energy absorption cellular materials in enhancing passive safety of road vehicles in side-impact accidents. *International Journal of Crashworthiness*, 19:288–300, 2014.

[36] ACP Composites. `http://www.acpsales.com/home.html`. Accessed February 2017.

[37] 3printr. Additive manufacturing of smart fibers composites. `www.3printr.com/additive-manufacturing-smart-fibers-composites-5840203/`. Accessed March 2017.

[38] W. Abramowicz and N. Jones. Dynamic axial crushing of circular tubes. *International Journal of Impact Engineering*, 3:263–281, 1984.

[39] W. Abramowicz and N. Jones. Dynamic axial crushing of square tubes. *International Journal of Impact Engineering*, 2:179–208, 1984.

[40] W. Abramowicz and N. Jones. Dynamic progressive buckling of circular and square tubes. *International Journal of Impact Engineering*, 4:243–270, 1986.

[41] N. Qiu, Y. Gao, J. Fang, Z. Feng, G. Sun, and Q. Li. Crashworthiness analysis and design of multi-cell hexagonal columns under multiple loading cases. *Finite Elements in Analysis and Design*, 104: 89–101, 2015.

[42] C. Baykasoglu and M. T. Cetin. Energy absorption of circular aluminum tubes with functionally graded thickness under axial impact loading. *International Journal of Crashworthiness*, 20:95–106, 2015.

[43] X. Zhang, Z. Wen, and H. Zhang. Axial crushing and optimal design of square tubes with graded thickness. *Thin-Walled Structures*, 84:263–274, 2014.

[44] G. Sun, F. Xu, G. Li, and Q. Li. Crashing analysis and multi objective optimization for thin-walled structures with functionally graded thickness. *International Journal of Impact Engineering*, 64:62–74, 2014.

[45] X. Zhang, H. Zhang, and Z. Wen. Axial crushing of tapered circular tubes with graded thickness. *International Journal of Mechanical Sciences*, 92:12–23, 2015.

[46] F. Xu, X. Tian, and G. Li. Experimental study on crashworthiness of functionally graded thickness thin-walled tubular structures. *Experimental Mechanics*, 55:1339–1352, 2015.

[47] X. Zhang and H. Zhang. Relative merits of conical tubes with graded thickness subjected to oblique impact loads. *International Journal of Mechanical Sciences*, 98:111–125, 2015.

[48] P. D. Bois, C. C. Chou, B. B. Fileta, T. B. Khali, A. I. King, H. F. Mahmood, H. J. Mertz, and J. Wismans. *Vehicle Crashworthiness and Occupant Protection*. American Iron and Steel Institute, 2004.

[49] Thailand automotive institute. How does eco car phase II promote thailand automotive industry, environment and safety drive? `http://thaiauto.or.th/2012/news/news-detail.asp?news_id=3172`. Accessed September 2017.

[50] Steel Market Development Institute. *Steel Bumper Systems for Passenger Cars and Light Trucks*. 5th edition, 2013.

[51] National Highway Traffic Safety Administration. FMVSS - NHTSA. `www.nhtsa.gov/laws-regulations/fmvss`. Accessed March 2017.

[52] W. T. Hollowell, H. C. Gabler, S. L. Stucki, S. Summers, and J. R. Hachney. Updated review of potential test procedures for FMVSS no.208, 1999.

[53] European New Car Assessment Programme. `www.euroncap.com/en`. Accessed March 2017.

[54] L. L. Hershman. The U.S. New Car Assessment Program (NCAP): past, present and future. 2001.

[55] Research Council for Automobile Repairs. *RCAR Bumper Test*. 2010.

[56] J. A. L. Campos, A. S. Robleda, J. A. V. Vilán, P. J. G. Nieto, and J. B. Cordero. Study of a steel's energy absorption system for heavy quadricycles and nonlinear explicit dynamic analysis of its behavior under impact by fem. *materials*, Oct 2015.

[57] G. M. S. Oliveira. Simulação numérica do comportamento ao impacto de componentes metálicos para aplicações de crashworthiness utilizando iniciadores de deformação configuráveis. Master's thesis, Escola de Engenharia da Universidade do Minho, 2015.

[58] G. Belingardi, A. Beyene, E. Koricho, and B. Martorana. Alternative lightweight materials and component manufacturing technologies for vehicle frontal bumper beam. *Composite Structures*, 120:483–495, 2015.

[59] European Aluminum Association. Design - case study: Crash Management Systems (CMS). *The Aluminum Automotive Manual*, 2011.

[60] European Aluminum Association. Materials - Designation Systems. *The Aluminum Automotive Manual*, 2002.

[61] SAPA. Liga 6061. `www.sapagroup.com/pt-PT/porque-o-aluminio/o-material/a-liga-certa/liga-6061/`. Accessed April 2017.

[62] European Aluminum Association. Applications - car body - crash management systems. *The Aluminum Automotive Manual*, 2013.

[63] A. V. Sobolev and M. V. Radchenko. Use of Johnson-Cook plasticity model for numerical simulations of the SNF shipping cask drop tests. *Nuclear Energy and Technology*, 2:272–276, 2016.

[64] X. Wang and J. Shi. Validation of Johnson-Cook plasticity and damage model using impact experiment. *International Journal of Impact Engineering*, 60:67–75, 2013.

[65] G. R. Johnson and W. H. Cook. Fracture characteristics of three metals subjected to various strains, strain rates, temperatures and pressures. *Engineering Fracture Mechanics*, 21(1):31–48, 1985.

[66] G. R. Johnson and W. H. Cook. A constitutive model and data for metals subjected to large strains, high strain rates and high temperatures. *In Proceedings of the 7th International Symposium on Ballistic*, 1983.

[67] Office of Aviation Research. Failure Modeling of Titanium 6Al-4V and Aluminum 2024-T3 With the Johnson-Cook Material Model. *U.S. Department of Transportation - Federal Aviation Administration*, Sep 2003.

[68] L. Schwer. Optional strain-rate forms for the Johnson Cook constitutive model and the role of the parameter epsilon_01. *6th European LS-DYNA Users Conference*, 2007.

[69] F. P. Beer, E. R. Johnston, and J. T. Dewolf. *Mechanics of Materials*. McGrawHill, 2006.

[70] A. Manes, L. Peroni, M. Scapin, and M. Giglio. Analysis of strain rate behavior of an al 6061 t6 alloy. *Procedia Engineering*, 10:208–2183477–3482, 2011.

[71] G. C. Eto. Federal regulation of defective vehicles. `www.garyeto.com`. Accessed March 2017.

[72] Altair University. *Crash Analysis With RADIOSS - A Study Guide*. 1st edition, 2015.

[73] LS-DYNA. What are the differences between implicit and explicit? `www.dynasupport.com/`. Accessed March 2017.

[74] P. Rebelo. Design study of a side intrusion beam for automotive safety. Master's thesis, Instituto Superior Técnico, Lisboa, Nov 2016.

[75] F. Djamaluddin, S. Abdullah, A. K. Ariffin, and Z. M. Nopiah. Multi objective optimization of foam-filled circular tubes for quasi-static and dynamic responses. *Latin American Journal of Solids and Structures*, 12(6), June 2015.

[76] Extrusal. Perfis standard. www.extrusal.pt/index.php?id=77&prt=64. Accessed April 2017.

[77] Aerospace Specification Metals Inc. Aluminum 6063-T6. asm.matweb.com/search/SpecificMaterial.asp?bassnum=MA6063T6. Accessed July 2017.

[78] H. Boyer and T. Gall. *Metals handbook; desk edition*. American Society for Metals,Metals Park, OH, Jan 1985.

[79] J.M. Holt, C. Gibson, C.Y Ho and Purdue University. Center for Information and Numerical Data Analysis and Synthesis. *Structural Alloys Handbook*. CINDAS/Purdue University, 1996.

[80] ASTM B557M-15. Standard test methods for tension testing wrought and cast aluminum- and magnesium-alloy products (metric). *ASTM International*, 2015.

[81] P. C. Albert, A. R. A. Ghani, M. Z. Othman, and A. M. A. Zaidi. Axial crushing behavior of aluminum square tube with origami pattern. 2015.

[82] K. Jelen, O. Fanta, R. Billich, D. Hadraba, and P. Kubový. Whiplash injury and head injury criterion during deceleration. *Transactions on Transport Sciences*, 4(4), 2011.

[83] United Nations. Concerning the adoption of uniform technical prescriptions for wheeled vehicles, equipment and parts which can be fitted and/or be used on wheeled vehicles and the conditions for reciprocal recognition of approvals granted on the basis of these prescriptions - addendum 93: Regulation no. 94. August 2013.

[84] I. Das and J. E. Dennis. Normal-boundary intersection: A new method for generating the pareto surface in nonlinear multicriteria optimization problems. *SIAM Journal on Optimization*, 8(3):631–657, August 1998.

[85] E. Kasprzak and K. E. Lewis. Pareto analysis in multiobjective optimization using the collinearity theorem and scaling method. *Structural and Multidisciplinary Optimization*, 22:208–218, 2001.

Appendix A

Optimization Process Force vs Displacement Curves

A.1 First Iteration

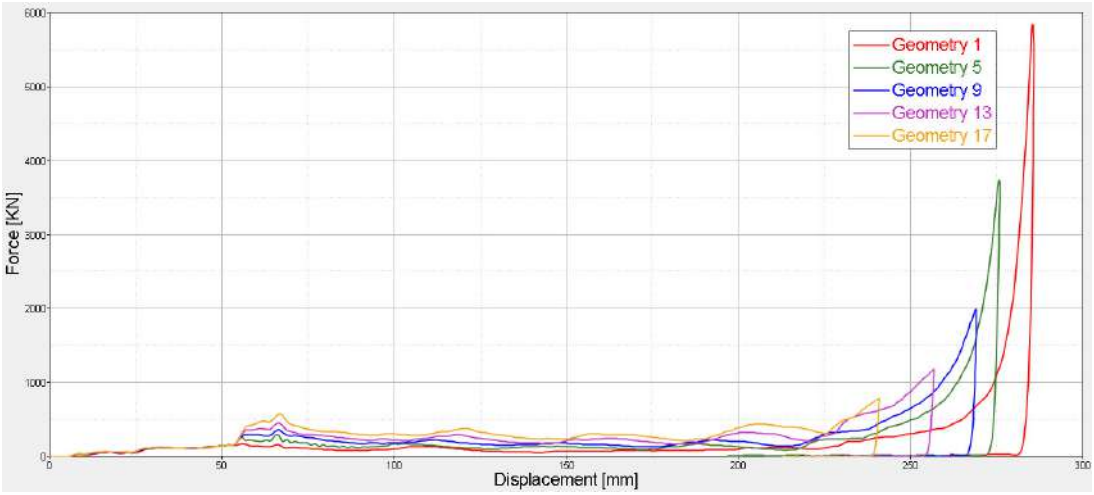

Figure A.1: Force-displacement curves of the first iteration (geometries with L = 300 mm)

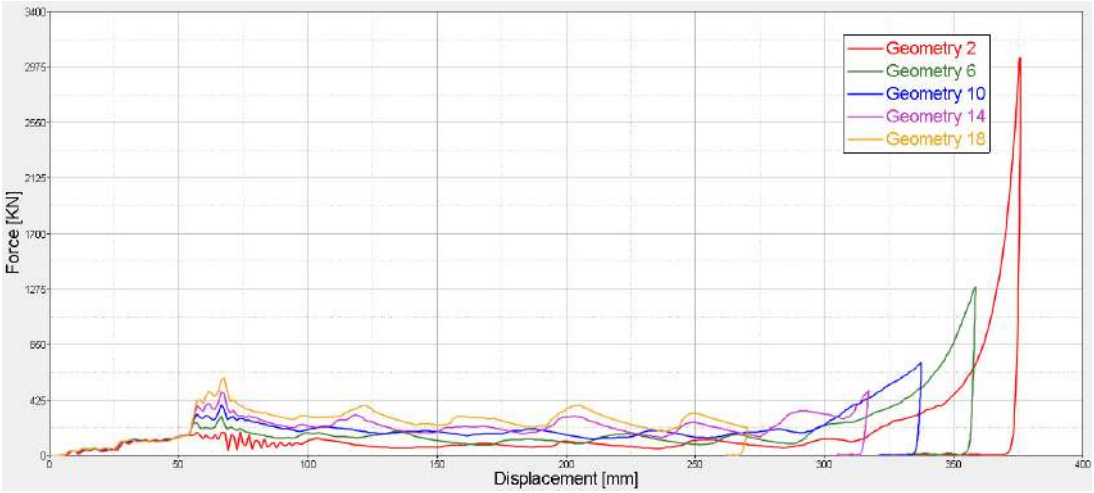

Figure A.2: Force-displacement curves of the first iteration (geometries with L = 400 mm)

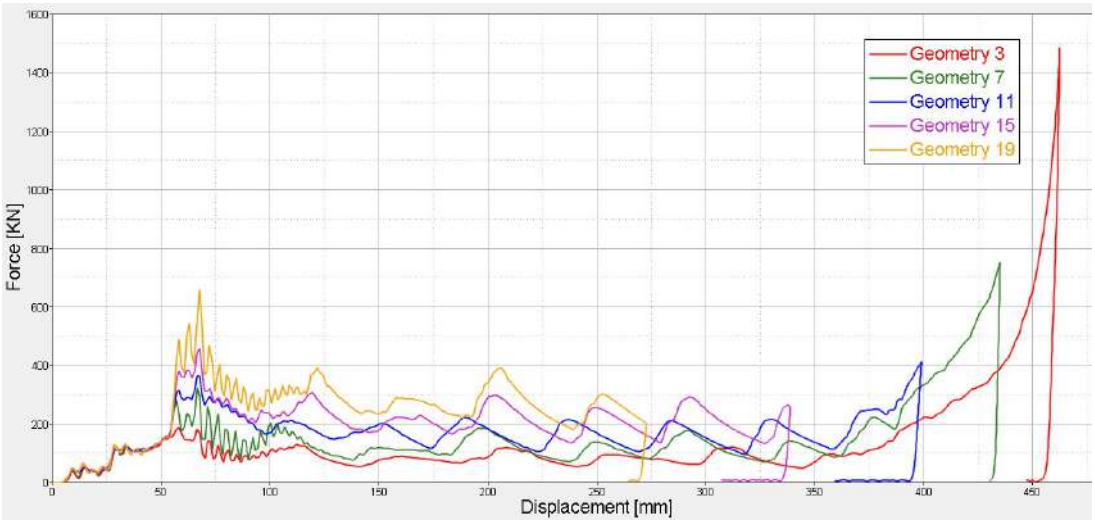

Figure A.3: Force-displacement curves of the first iteration (geometries with L = 500 mm)

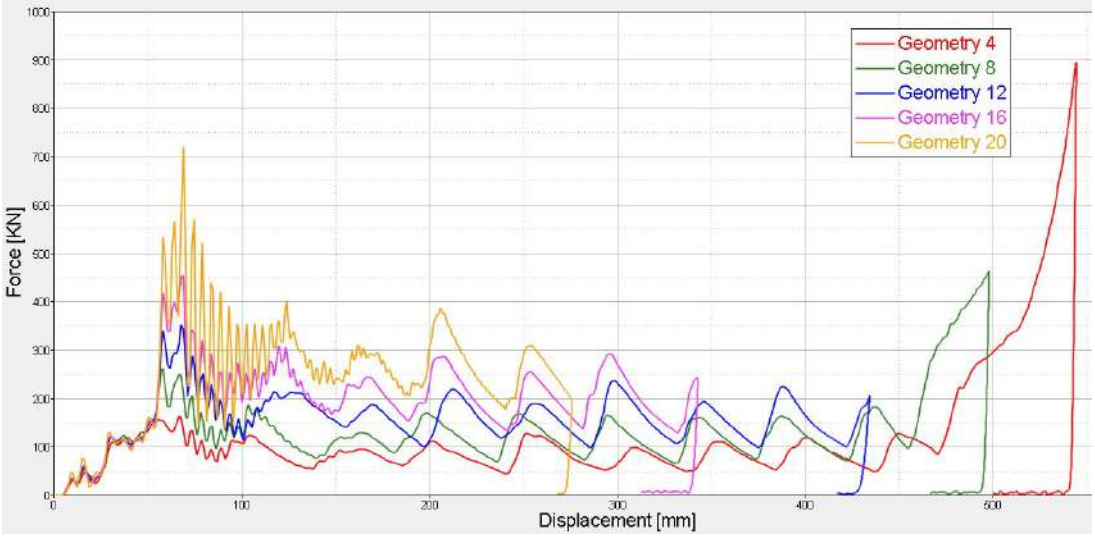

Figure A.4: Force-displacement curves of the first iteration (geometries with L = 600 mm)

A.2 Second Iteration

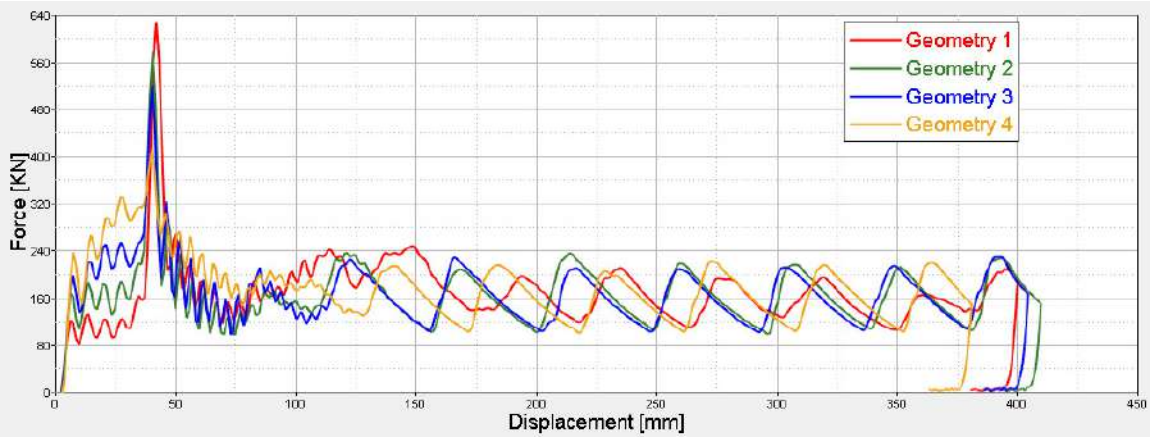

Figure A.5: Force-displacement curves of the second iteration (geometries with D = no and R = straight)

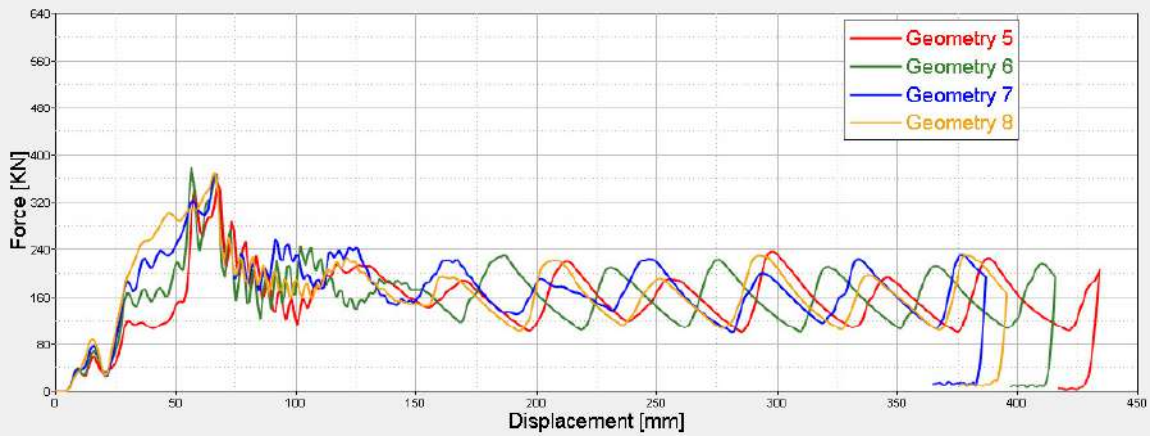

Figure A.6: Force-displacement curves of the second iteration (geometries with D = no and R = 3200 mm)

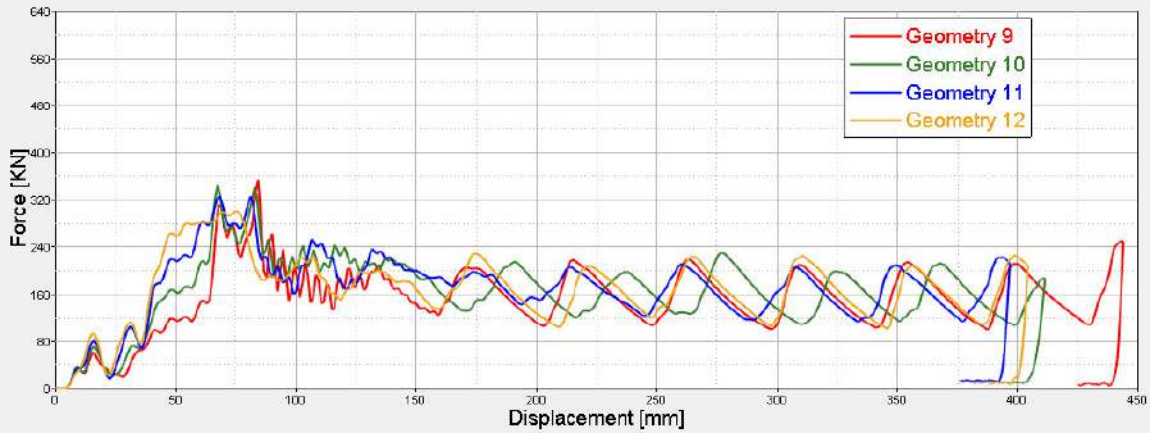

Figure A.7: Force-displacement curves of the second iteration (geometries with D = no and R = 2000 mm)

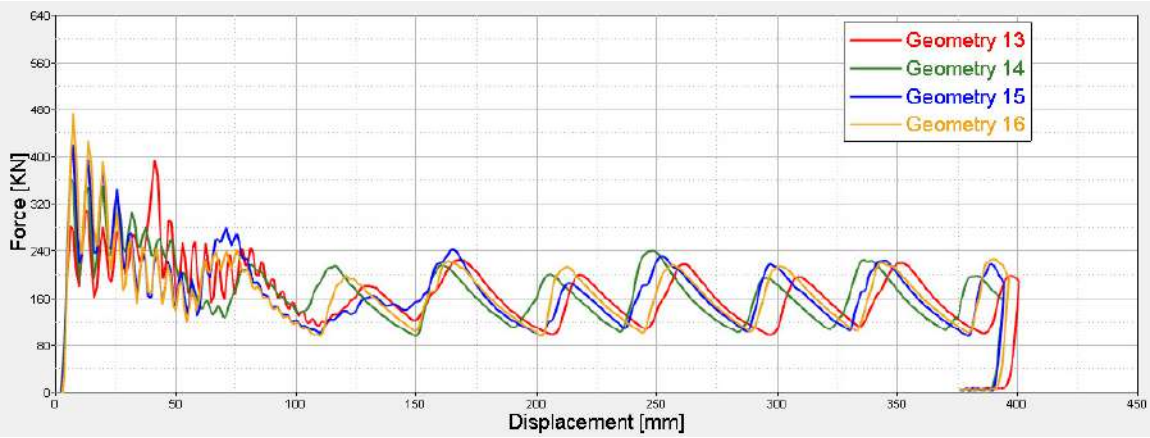

Figure A.8: Force-displacement curves of the second iteration (geometries with D = yes and R = straight)

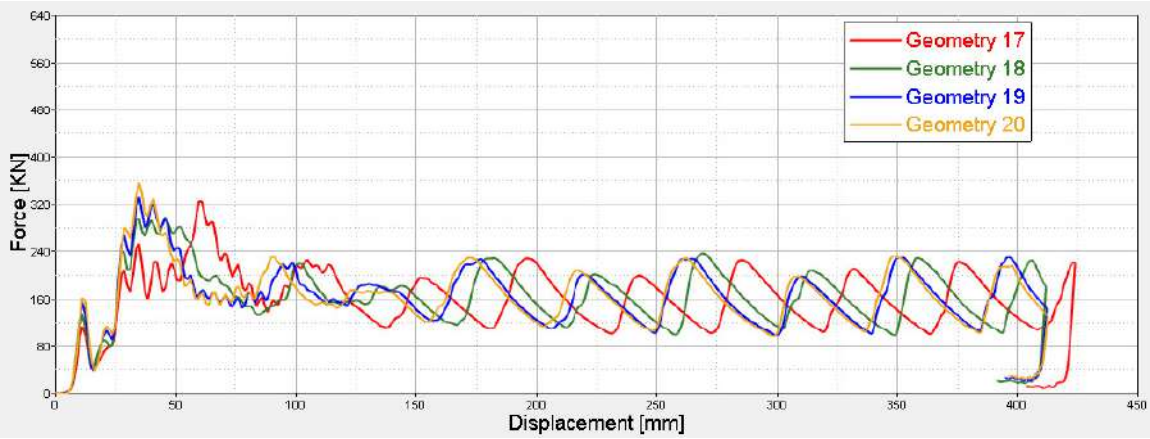

Figure A.9: Force-displacement curves of the second iteration (geometries with D = yes and R = 3200 mm)

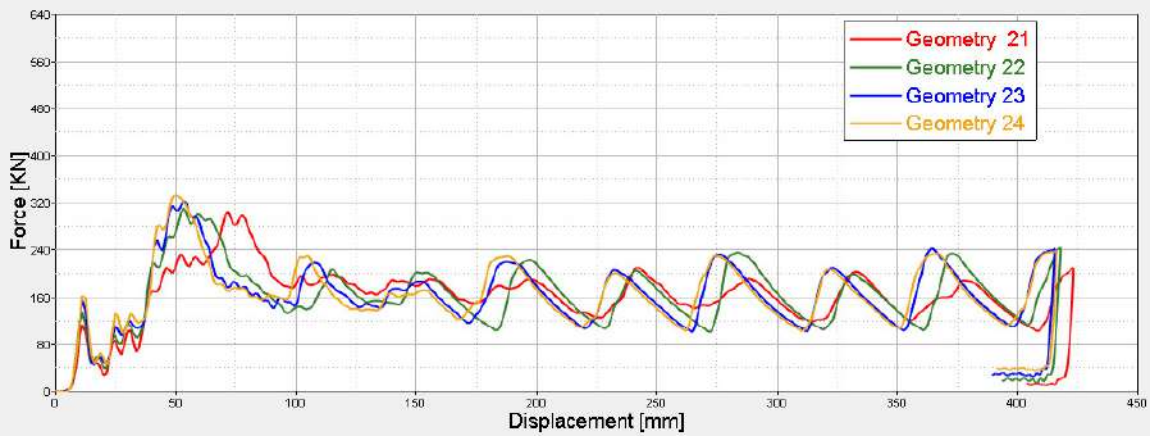

Figure A.10: Force-displacement curves of the second iteration (geometries with D = yes and R = 2000 mm)

A.3 Third Iteration

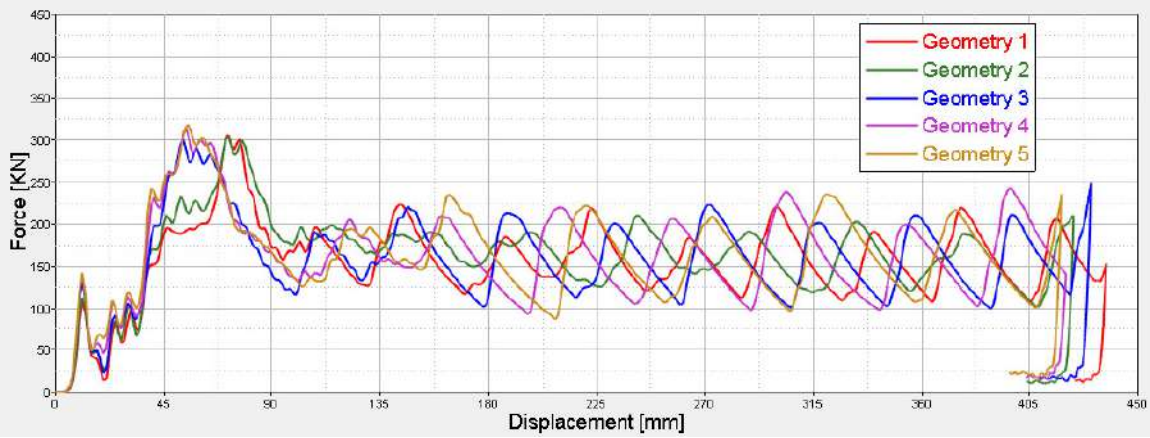

Figure A.11: Force-displacement curves of the third iteration (squared section)

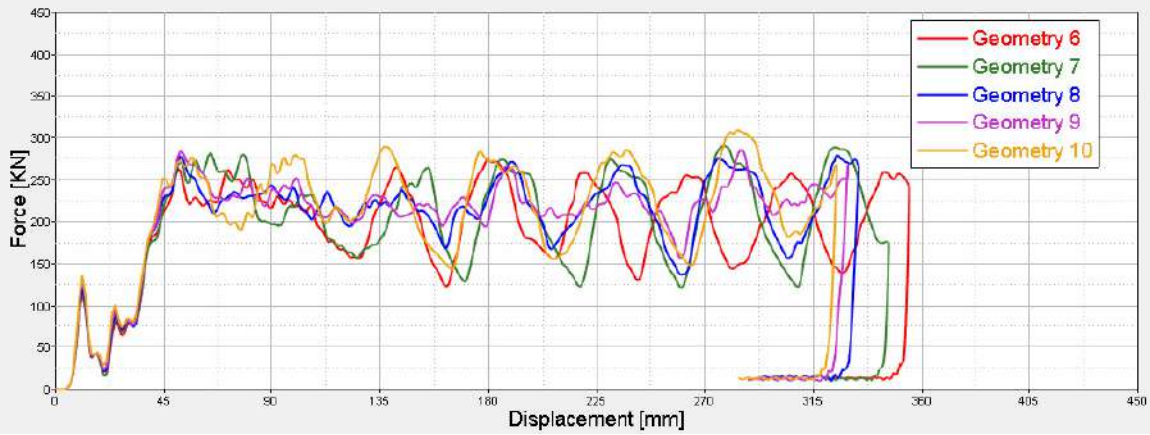

Figure A.12: Force-displacement curves of the third iteration (circular section)

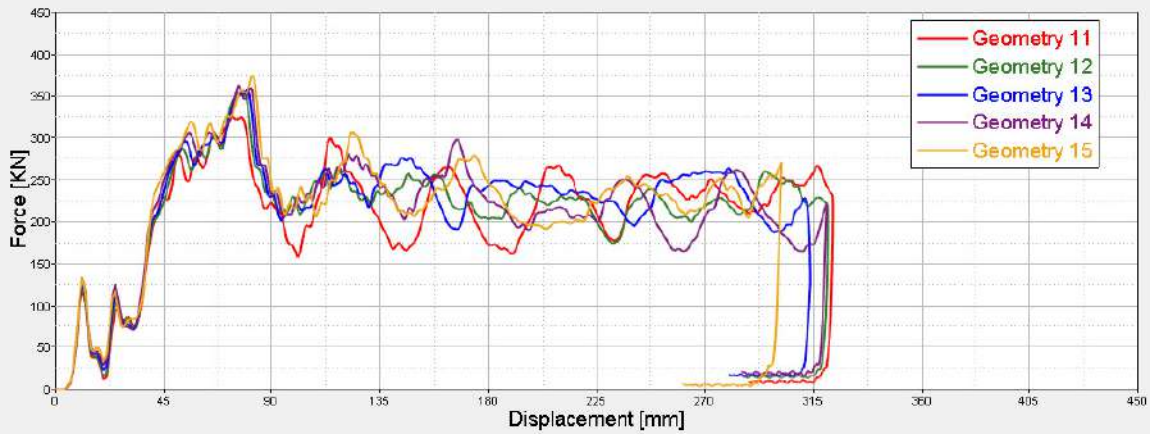

Figure A.13: Force-displacement curves of the third iteration (hexagonal section)

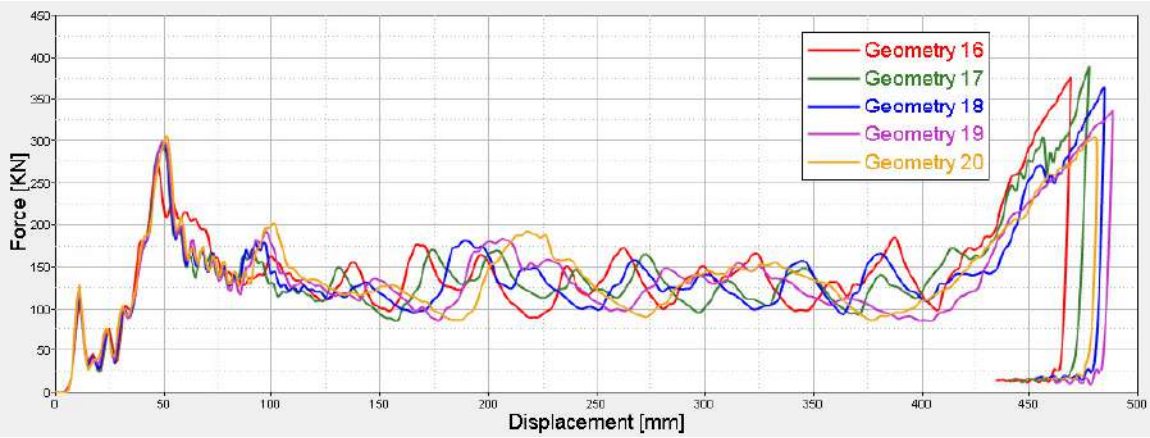

Figure A.14: Force-displacement curves of the third iteration (triangular section)

A.4 Fourth Iteration

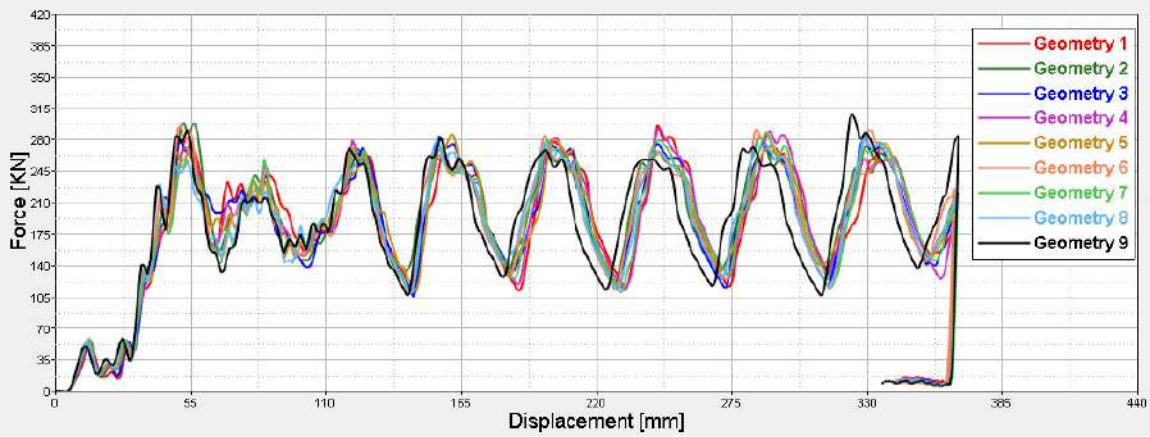

Figure A.15: Force-displacement curves of the fourth iteration (geometries with Z = 20 mm)

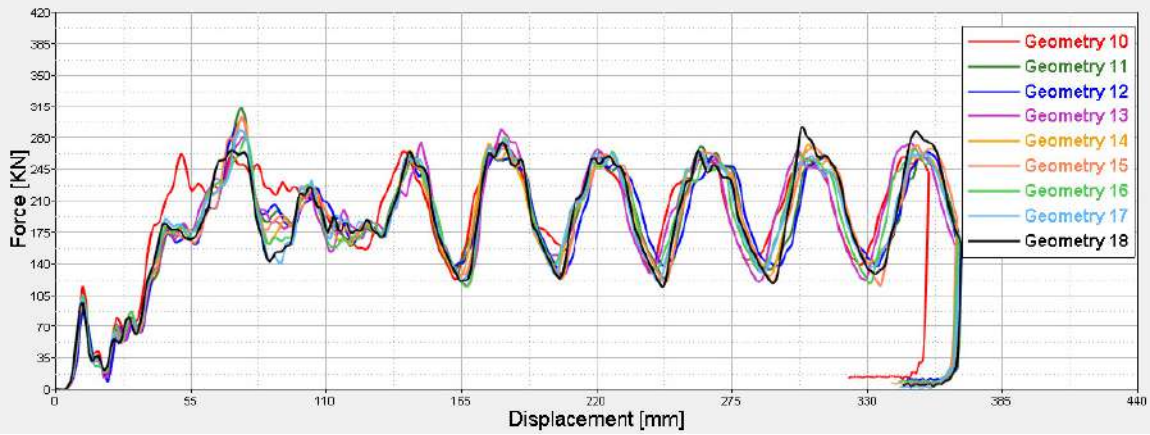

Figure A.16: Force-displacement curves of the fourth iteration (geometries with Z = 40 mm)

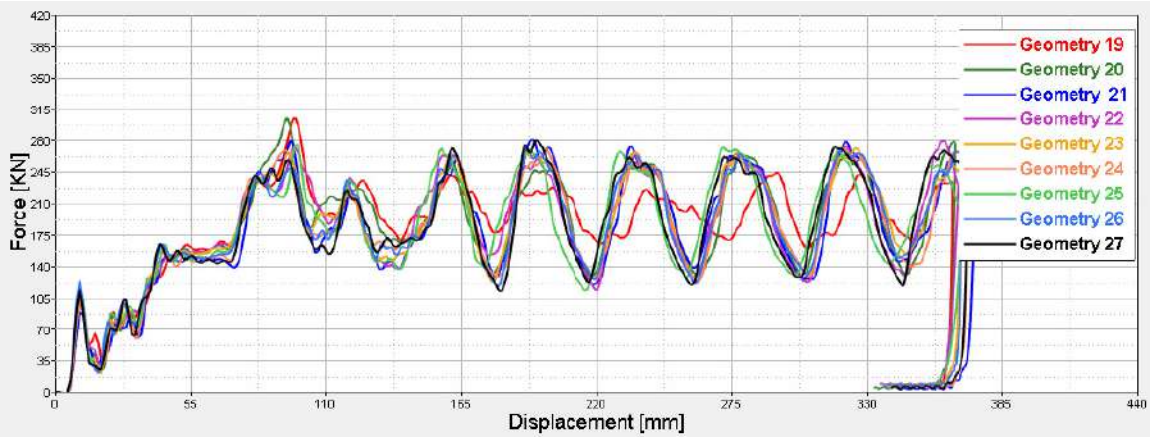

Figure A.17: Force-displacement curves of the fourth iteration (geometries with Z = 60 mm)

Appendix B

Optimization Process Results

B.1 First Iteration

Table B.1: First iteration results

Geometry	Mass [kg]	EA [J]	Displacement [mm]	F_{max} [kN]	F_{avg} [kN]	**SEA [J/kg]**	**CFE**
REF 1	3.421	69830	286	5850	244	20412	0.042
2	3.823	68917	376	3050	183	18027	0.060
3	4.224	66207	462	1485	143	15674	0.096
4	4.626	67968	544	894	125	14693	0.140
5	3.679	69901	276	3742	253	19000	0.068
6	4.179	68111	358	1293	190	16298	0.147
7	4.678	67976	435	751	156	14531	0.208
8	5.178	67910	498	465	136	13115	0.294
9	3.934	69993	269	1998	260	17792	0.130
10	4.530	68211	337	710	202	15058	0.285
11	5.127	68057	399	414	171	13274	0.412
12	5.723	67790	434	353	156	11845	0.443
13	4.186	68608	257	1183	267	163890	0.226
14	4.887	68101	317	497	215	13935	0.432
15	5.569	67991	339	459	201	12209	0.437
16	6.261	67887	343	453	198	10843	0.4370
17	4.434	68581	241	783	285	15467	0.363
18	5.220	68209	2709	597	252	13067	0.422
19	6.006	68163	273	659	250	11349	0.379
20	6.792	67898	276	721	246	9997	0.341

B.2 Second Iteration

Table B.2: Second iteration results

Geometry	Mass [kg]	EA [J]	Displacement [mm]	F_{max} [kN]	F_{avg} [kN]	**SEA [J/kg]**	**CFE**
1	5.725	67646	400	627	169	11816	0.270
2	6.178	67709	410	578	165	10960	0.286
3	6.624	67991	405	520	168	10264	0.323
4	7.065	67735	381	410	178	9587	0.434
REF 5	5.723	67790	434	351	156	11845	0.443
6	6.175	67859	416	378	163	10989	0.431
7	6.621	67854	387	367	175	10248	0.477
8	7.061	67873	396	369	171	9612	0.464
9	5.655	67902	444	352	153	12007	0.434
10	6.110	67735	412	345	165	11086	0.477
11	6.558	67948	397	324	171	10361	0.528
12	7.000	68142	405	300	168	9735	0.562
13	5.991	67677	401	394	169	11296	0.429
14	6.487	67587	394	361	171	10419	0.474
15	6.975	67625	395	419	171	9695	0.409
16	7.453	67557	397	472	170	9064	0.361
17	5.988	68147	424	324	161	113801	0.495
18	6.484	68133	412	295	165	10508	0.560
19	6.971	68163	412	332	165	9778	0.498
20	7.449	68148	413	356	165	9149	0.463
21	5.922	68888	423	304	163	11633	0.536
22	6.421	68169	418	310	163	10616	0.525
23	6.910	68240	416	323	164	9876	0.509
24	7.390	68377	416	333	164	9253	0.494

B.3 Third Iteration

Table B.3: Third iteration results

Geometry	Mass [kg]	EA [J]	Displacement [mm]	F_{max} [kN]	F_{avg} [kN]	**SEA [J/kg]**	**CFE**
1	5.556	68187	437	305	156	12272	0.512
2	5.739	68132	431	300	158	11872	0.528
REF 3	5.922	68888	423	304	163	11633	0.536
4	6.105	68259	420	313	162	11181	0.519
5	6.289	68287	4191	317	163	10858	0.515
6	4.928	68264	355	274	192	13852	0.703
7	5.072	67979	3466	290	196	13403	0.678
8	5.216	67849	334	279	203	13008	0.729
9	5.360	67847	330	284	206	12658	0.724
10	5.504	68136	325	308	210	12379	0.681
11	5.158	67914	323	326	210	13167	0.644
12	5.316	68786	321	357	214	12939	0.600
13	5.474	69382	314	358	221	12675	0.618
14	5.632	68886	321	363	215	12231	0.592
15	5.790	67242	302	374	223	11613	0.596
16	4.743	68011	469	376	145	14339	0.385
17	4.878	67922	478	389	142	13924	0.366
18	5.012	69052	485	364	142	13777	0.391
19	5.147	68918	489	35	141	13390	0.421
20	5.282	68305	481	305	142	12932	0.466

B.4 Fourth Iteration

Table B.4: Fourth iteration results

Geometry	Mass [kg]	EA [J]	Displacement [mm]	F_{max} [kN]	F_{avg} [kN]	**SEA [J/kg]**	**CFE**
1	4.461	67692	365	295	186	15174	0.628
2	4.289	68026	367	283	186	15861	0.655
3	4.186	68216	365	299	187	16296	0.626
4	4.392	68103	366	292	186	15506	0.637
5	4.183	68076	365	285	186	16274	0.653
6	4.065	68215	365	294	187	16781	0.636
7	4.336	67995	367	287	186	15681	0.647
8	4.088	68033	366	286	186	16642	0.649
9	3.947	68083	367	308	185	17249	0.602
REF 10	4.928	68264	355	274	192	13852	0.703
11	4.735	68120	369	312	185	14386	0.591
12	4.601	67866	369	302	184	14750	0.609
13	4.858	68310	368	289	186	14061	0.644
14	4.639	68016	368	301	185	14662	0.613
15	4.488	68066	366	303	186	15166	0.613
16	4.794	68046	3678	280	186	14194	0.663
17	4.551	67953	368	288	185	14931	0.643
18	4.379	68180	368	292	185	15570	0.634
19	5.402	67761	364	305	186	12544	0.610
20	5.195	67497	366	305	185	12993	0.605
21	5.035	67904	374	281	181	13486	0.646
22	5.329	67605	367	279	184	12686	0.660
23	5.105	67838	368	271	184	13289	0.679
24	4.931	67859	372	272	182	13762	0.671
25	5.262	67562	368	275	183	12840	0.667
26	5.021	67924	369	272	184	13528	0.677
27	4.830	67882	371	280	183	14054	0.653